Dipole-strength distribution below the particle emission threshold in ^{124}Sn and ^{112}Sn

Melissa Boswell

A dissertation submitted to the faculty of the University of North Carolina at Chapel Hill in partial fulfillment of the requirements for the degree of Doctor of Philosophy in the Department of Physics and Astronomy.

Chapel Hill
2008

Approved by:

H. J. Karwowski, Advisor

A.P. Tonchev, Reader

A. Champagne, Reader

J. Engel, Reader

J. Ng, Reader

© 2008
Melissa Boswell
ALL RIGHTS RESERVED

Abstract

MELISSA BOSWELL: Dipole-strength distribution below the particle emission threshold in ^{124}Sn and ^{112}Sn.
(Under the direction of H. J. Karwowski.)

Dipole-strength distributions around the neutron emission threshold have been measured in ^{124}Sn and ^{112}Sn at the free electron laser facility at Duke University. In total, 103 ground state transitions were observed in ^{124}Sn, and 13 ground state transitions were observed in ^{112}Sn. The use of the 100% linearly polarized γ-ray beam at the free electron laser allows for very accurate parity measurements. The spin and parity of 22 levels were confirmed, and 57 new parities were assigned in ^{124}Sn. In ^{124}Sn, 22 new levels were observed in ^{124}Sn, and 13 new levels were observed in ^{112}Sn. A method was developed in this thesis to determine the flux of the incident Compton-scattered γ-ray beam. The procedure was tested using both a well known transition in ^{11}B, and previous ^{124}Sn measurements. The integrated cross section, decay widths, and reduced transitions strengths were calculated for each of the 103 ground state transitions. The summed transitions strength exhausted 0.54% of the energy-weighted-sum rule in ^{124}Sn, 0.12% of the energy-weighted-sum rule in ^{112}Sn. Energy averaged absorption cross sections were compared with previous measurements above the neutron separation energy in ^{124}Sn. An examination of the entire energy spectra in ^{124}Sn shows that the strength below 10 MeV has an average energy of 8.25 ± 0.32 MeV which corresponds to 5.27% of the total strength below 25 MeV. The average properties of this energy region were extracted and compared with predictions from various theoretical models.

Table of Contents

List of Tables

List of Figures

1 Introduction

Describing physical systems that comprise many bodies that interact with each other as well as their environment often becomes quite complicated. In some cases, if the number of objects is large enough, as is the case with a drop of liquid or a volume of gas, statistical methods can be very successful. In other cases, such as planetary systems, the interaction involves some center of force that is much stronger than any other interactions, which can be treated as small perturbations. The interactions involved in a nucleus lie somewhere between these two relatively simple scenarios. Most nuclei contain too few particles to be modeled using statistical methods, but no definite center of force minimizes the effects of forces among nucleons. The basic approach, therefore, requires relating experimental data to some better understood phenomena with simple models, in this case the shell model and the collective model.

The most prominent instance of collective motion is the Giant Dipole Resonance (GDR). This massive concentration of dipole strength, whereby radiation penetrates deep into the nucleus causing the periodic spatial separation of the protons and neutrons, dominates the nuclear landscape. This study, however, concerns not the GDR but rather a small bump that appears on the low-energy side of the GDR just below the particle-emission threshold. In the early 1960s, multiple researchers investigated the energy dependence of photon scattering on various targets. Several experiments revealed a small concentration of dipole strength at the neutron emission threshold [Ful56, Rei60]. In comparison to the GDR, this second resonance was much smaller, exhausting between 3% to 6% of the E1 sum rule. Such a diminutive resonance, dwarfed by the GDR, earned its current moniker of

Pygmy Dipole Resonance (PDR).

To the untrained observer, this meager dipole strength seems inconsequential, but, the PDR could have far reaching effects; it could even change the elemental composition of the Universe, at least theoretically. In the realm of nuclear astrophysics, the rapid-neutron process (or r-process) is believed to account for nearly half the nuclides heavier than iron [Mat83]. As its name suggests, the rapid-neutron process is believed to occur in very neutron-rich environments where nuclei capture neutrons much faster than they can decay [Mat83]. In the theoretical models, the neutron capture rates are typically calculated in the framework of the Hauser-Feshbach model, and they strongly depend on the decay channels of the modeled nucleus [Gor98]. The photon transmission coefficient, dominated by E1 transitions, is generally modeled by a Lorentzian fit to the GDR. Any low-energy strength enhancements, which are not well described by this Lorentzian fit, could change the estimated neutron capture cross section. A second lower energy Lorentzian was included in a such a calculation on ^{208}Pb. This lower energy Lorentzian at 4.2 MeV resulted in a five fold increase in the neutron capture cross section despite accounting for only 1% of the total E1 strength [Gor98].

What could cause the strength attributed to the PDR? At the time of the PDR's discovery, physicists proposed a variety of explanations for this bantam bump. Some argued that this bump was due to threshold states from surface phenomena in nuclei [Baz59].[1] Others argued that the bump was simply an extrapolation of the GDR [Axe62]. The major problem with resolving this issue was the conflicting results from the two main experimental investigations. In 1956, Fuller and Hayward measured the elastic scattering cross section of 14 nuclei as a function of photon energy from 4-40 MeV [Ful56, Ara73]. While the GDR peak and maximum cross section were consistent with the statistical theory of the GDR, the corresponding lower-energy parameters differed from this same theory. In 1960, Reibel and Mann measured the elastic scattering cross sections of 32 elements in the 7-MeV γ-ray energy range [Rei60]. Their elastic cross sections were a factor of two or more below the results of Fuller and Hayward [Ara73]. Not until 1962, when Axel re-examined the scattering cross sections

[1] Baz reformulated the Wigner-Eisenbud theory to account for a surface potential. When this potential was included, quasi-bound states appeared with a high probability close to the various thresholds.

and inferred decay widths at 7 MeV for the two measurements, were the reasons for the discrepancies understood [Axe62]. Axel realized that the large resolution of the photon sources in the two measurements might not be able to discern individual levels, so he suggested that decays that had been interpreted as single ground-state transitions were actually averaged gross properties of many levels. Using the Porter-Thomas distribution to describe the distribution of levels, Axel brought the two measurements into agreement not only with each other but also with results from neutron capture data. In addition, Axel found that a low-energy extrapolation of the Lorentzian fit the GDR agreed with the corrected absorption cross sections [Axe62].

If, as Axel's work suggests, this strength enhancement is in fact collective, what could be the cause? The nature of the nucleus is such that, below the particle-emission threshold very few nucleons are available to participate in collective motion. A mixture of the Pauli Principle and the "weakness" of the strong interaction[2] prevents core nucleons from interacting unless they can be scattered into the outer unoccupied orbits. The GDR is an example of one such excitation, in which a nucleon is excited above the Fermi surface, setting the remaining core nucleons into motion to preserve the center of mass [Cas00]. For the PDR, however, the interacting photon does not have nearly the energy required to disturb this nuclear core, and thus, the incident radiation transfers its energy to the valence nucleons, setting them into motion against a seemingly inert core [Suz90].

While an oscillating neutron skin certainly sounds collective, it is not necessarily so. The classification of collectivity is generally reserved for situations in which multiple single-particle transitions contribute to the total strength [Ish00]. In the case of the GDR, no single transition contributes more than 20-30% to the observed strength. Numerous microscopic theories have been developed to understand the PDR on this fundamental single nucleon basis. Of particular interest are the Quasi-Phonon Model and the Relativistic Random Phase Approximation. While both models use the standard relativistic mean field theory to describe the ground state, they approach excited nuclear states very differently. In the Random Phase Approximation (RPA), excited states are produced by creating a

[2]Weakness here refers to the weakness of the strong interaction relative to the kinetic energy of the nucleons in the nuclear volume.

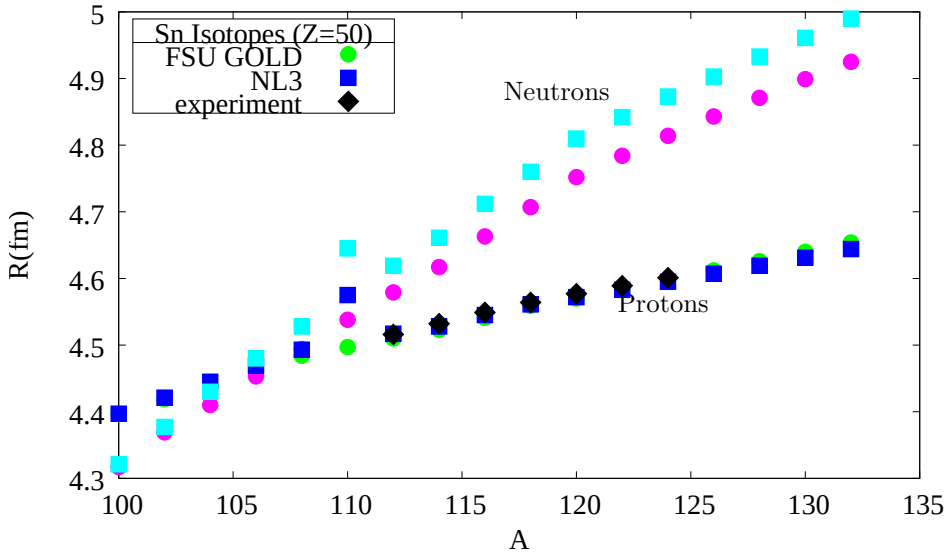

Figure 1.1: The theoretical predictions for proton and neutron root-mean-square radii for various Sn isotopes are plotted along with the available experimental data [Pie06]. The experimental data is taken from reference [De 87]. The circles (squares) indicate the predicted root-mean-square radii of the FSU Gold model (NL3). FSU Gold and NL3 are accurately calibrated parameter sets used in RPA calculations. Such a large range in the radii of the neutron skins, gives Sn isotopes an advantage over other isotopic chains in studying the PDR.

particle-hole pair in the nucleus. Collective motion in the (Q)RPA is achieved by considering a superposition of particle-hole (or two-quasi-particle) states [Paa07]. The Quasi-Phonon Model (QPM) considers more complex excited states. In this model, the excited states are constructed out of phonons that comprise two-quasi-particle pairs, which can form simple (one-phonon) configurations, complex (two-three phonon) configurations or a combination of the two [Paa07].

In the past decade these theoretical models have been used to study the PDR in various isotopes with widely varying results. Models based on the RPA have shown that excitations below the GDR in light nuclei are due entirely to non-resonant, single-neutron excitations [Lit07]. In the case of medium-heavy and heavy nuclei, the RPA results depend on the various assumptions of each microscopic model. The various predictions range from collective excitations that can be correlated with the neutron skin to single-particle excitations such as those observed in lighter nuclei [Lit07].

If the oscillation of the neutron skin is an accurate description of the PDR, then one would expect to find a clear correlation between the summed dipole strength and the neutron skin thickness. The

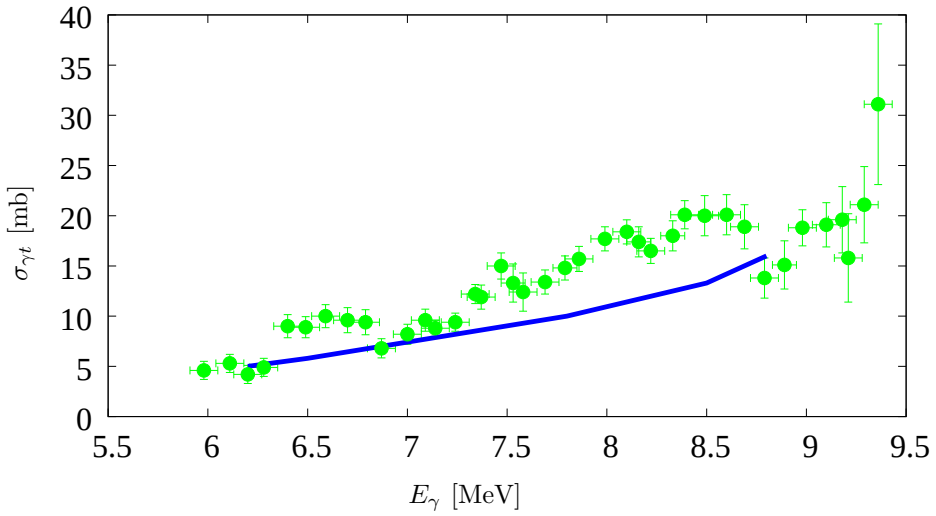

Figure 1.2: Total photon interaction cross section of Sn from the Axel *et al.* experiment [Axe70]. The green circles represent the observed total photo-absorption cross section. The solid line represents the extrapolation from the GDR into the measurement energy region. As shown, there is significant photo-absorption strength above what is expected from the GDR extrapolation, indicating the possible existence of a separate collective excitation in this energy region.

effects of such an oscillation should be particularly prominent for neutron skins due to the absence of the Coulomb interaction. Figure 1.1 shows the theoretical predictions of the neutron and proton radii, R_n and R_p respectively, for different Sn isotopes [Pie06]. All isotopes from ^{106}Sn to ^{132}Sn have a neutron skin ($R_n - R_p$), which increases with mass. Such a large range of valence neutrons, and consequently the radii of the neutron skins, makes Sn isotopes especially useful for studying the PDR.

In 1970 Axel *et al.* used the University of Illinois's bremsstrahlung facility to study these sub-threshold states in natural Sn (the results are displayed in Figure 1.2) [Axe70]. Axel *et al.* showed that the strength of the ground-state transitions far exceeded the predictions of the extrapolated GDR in this lower energy region and that these extrapolations accounted for as a little as 50% of the observed dipole strength at some energies. Unfortunately, because Sn has so many stable isotopes determining the contribution of each isotope was impossible. In addition, the range of particle-emission thresholds of these stable isotopes (see Table 1.1) complicated the process of estimating the strength of PDR. For example, the cross section dropped by as much as 30% between 8.6 and 8.8 MeV, an energy range that also corresponds to the neutron emission threshold of ^{122}Sn and ^{124}Sn, the stable nuclei with the

Mass	Abundance (%)	Thresholds (MeV) (γ, n)	(γ, p)	$< E >_{GDR}$ (MeV)
112	0.97	10.786(6)	7.559(6)	
114	0.65	10.299(3)	8.4807(13)	
115	0.35	7.5464(17)	8.7528(18)	
116	14.30	9.563 (7)	9.270(9)	15.56
117	7.68	6.9446(11)	9.437(4)	15.65
118	24.03	9.3263(14)	9.999(5)	15.44
119	8.58	6.4854(14)	10.126(8)	15.53
120	32.85	9.1074(22)	10.689(7)	15.38
122	4.72	8.8132(25)	11.394(27)	
124	5.94	8.488(3)	12.100(25)	15.19

Table 1.1: Natural abundances of Sn. Sn has 10 stable isotopes, and a magic core composed of 50 protons. The thresholds and abundances are taken from the reference [Aud93], while the experimental GDR energies are taken from the RIPL website [Bel06].

largest neutron skin.

In 1994, at the Gent Linac, the E1 strength below the neutron separation energy was investigated in ^{116,124}Sn isotopes [Gov98]. Using a partially linearly polarized bremsstrahlung beam, the Gent group identified more than 150 dipole ground-state transitions above 4.1 MeV in both ^{116,124}Sn. The Gent experiment showed that the E1 strength in ^{124}Sn was significantly larger than what was observed for ^{116}Sn.[3] This finding seemed to contradict the QPM predictions, notably that the E1 strength should peak about ^{120}Sn [Gov98].

The Gent group experienced considerable difficulty in establishing the parity of many measured levels, assigning only 69 parities of the 150 measured levels. Many of the higher energy levels in ^{116,124}Sn decayed indirectly to the ground state by way of intermediate levels. This low-lying feeding is especially troublesome in parity measurement, which rely on an azimuthal asymmetry in the angular distributions.[4] Furthermore, the large energy range of the bremsstrahlung beam is such that the decay pattern of the higher lying states is obscured by states directly populated by the beam [Gov98].

The difficulties encountered in the Gent experiments can be partially alleviated by using a 100%

[3]The Gent group assumed all transitions were electric dipole. Under this assumption, the summed strength in ^{124}Sn was greater than ^{116}Sn.

[4]The angular distribution of the emitted radiation is determined by the polarization plane of the γ-ray that initially populated the state. If an excited state is populated by multiple sources, say a γ-ray beam and a higher lying transitions, depending on the spin and parity of the higher-lying state, the decay pattern will depend not only on the polarization plane of the γ-ray beam, but also the polarization plane of the higher-lying states.

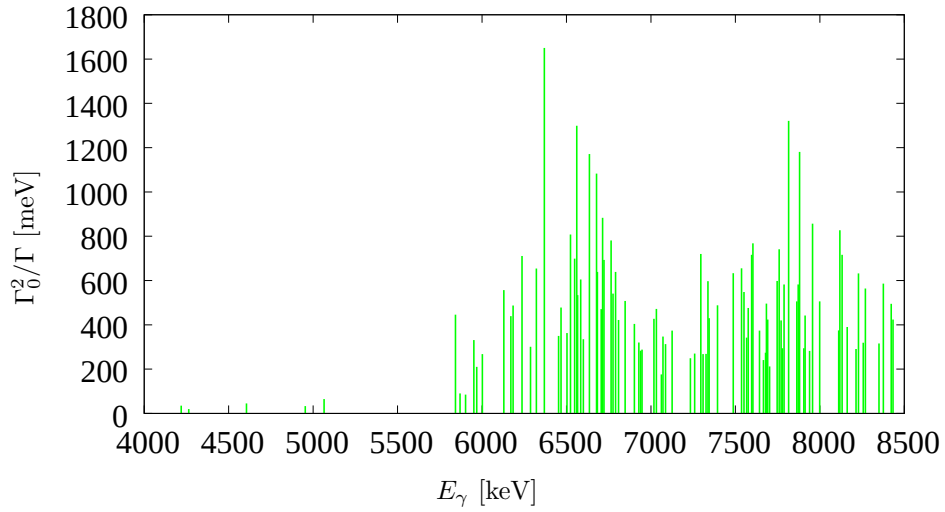

Figure 1.3: Dipole strength distributions for ground-state transitions in ^{124}Sn from Gent experiment [Gov98]. In total, 95 ground-state transitions were measured in ^{124}Sn, but only 35 transitions were identified as electric dipole and two transitions were identified as magnetic dipole.

linearly polarized Compton backscattered γ-ray beam, such as the High Intensity γ-ray Source (HIγS) at the Duke Free Electron Laser Lab (DFELL). Because the HIγS beam is nearly mono-energetic, it allows the selective probing of excited states, enabling a careful examination of the feeding of low lying levels. In addition, since the angular distribution of an nuclear transition depends on the polarization plane of the populating γ-ray, an incident beam of linearly polarized γ-rays produces γ-rays with an azimuthal asymmetry. When undergoing a *magnetic* dipole transition, the nucleus radiates *parallel* to the polarization plane; it radiates *perpendicular* to the polarization plane as a result of an *electric* dipole transition. Therefore, by comparing transition strengths in detectors at azimuthal scattering angles of $\phi = 0°$ and $90°$, we can easily distinguish E1 from M1 excitations.

The main *experimental* goals of the present investigation are to measure the transitions strengths below the particle-emission threshold in both ^{124}Sn as well as ^{112}Sn. Using the nuclear resonance fluorescence method (discussed in Chapter 2), the current research will essentially remeasure the states in ^{124}Sn observed in the Gent experiment. The achievable goals are twofold, first, I hope to improve on parity measurements of the Gent group. Second, by comparing my cross-section measurements with those of the Gent group, I can establish the parameters under which absolute cross-section

measurements can be made at HIγS (see Section 4.5). Assuming that ^{124}Sn cross sections can be reproduced, the new cross sections for ^{112}Sn will also be reported for the first time.

The main *theoretical* goals of the present experimental investigation include determining the nature of these low-energy dipole states and their relationship with the eminent strength of the GDR. In addition, the strength distributions will be compared with various theoretical models in the hope of understanding the possible sources of these excitations (see Section 5.3). Finally, in comparing the strength distributions with other (γ, n) experiments at higher energies, we can determine the PDR's contribution to the energetic landscape of electric-dipole strength. The results of this analysis will be presented in Chapter 5. Final conclusions and remarks will be presented in Chapter 6.

2 Nuclear Resonance Fluorescence

Nuclear Resonance Fluorescence (NRF) refers to the process of exciting a nucleus via an electromagnetic interaction. The relative simplicity of the interaction in the NRF experiment can yield the following spectroscopic information:

- level excitation energy E_x
- total cross section I_s
- spin J
- parity π
- transition width ratio Γ_0^2/Γ
- reduced excitation probabilities $B(\pi\ell) \uparrow$

In this chapter, I shall derive the reduced transition strengths and relate them to integrated cross sections. The latter part of the chapter explains the theoretical basis behind spin and parity measurements.

2.1 Quantization of Radiation

Consider a pure radiation field (light waves) that satisfies the wave equation in free space such that the scalar potential $\psi = 0$ and $\mathbf{A}$ are defined for all points of space and time.[1] The vector potential

[1] A formal derivation of the ideas presented here can be found in reference [Hei54]

for such a radiation field is

$$\mathbf{A} = \sum_{\lambda} (q_\lambda \mathbf{A}_\lambda + q_\lambda^* \mathbf{A}_\lambda^*). \tag{2.1}$$

Assuming that $\mathbf{A}_\lambda$ satisfies the Helmholtz equation and that q_λ satisfies the harmonic-oscillator equation for a single quantum in an enclosed volume V, the vector potential can be expressed as a series of standing spherical waves:

$$\mathbf{A}_\lambda(\mathbf{r}) = \sum_{\ell=0}^{\infty} \sum_{m=-\ell}^{\ell} \frac{8\pi\omega^2}{\ell(\ell+1)R_0} j_\ell(kr) \sqrt{\ell(\ell+1)} \mathcal{Y}^m_{J,\ell,1},$$

where J is defined such that $J_z = \ell_z + s_z$, $\mathcal{Y}^m_{J,\ell,1}$ is the vector spherical harmonic and $j_\ell(kr)$ is the spherical Bessel function. For photons, or any spin-one particle, there are three kinds of spherical harmonics, corresponding to ℓ=J+1 ,ℓ=J, and ℓ=J-1, forming a complete set of basis vectors in three dimensions. The parity of these spherical harmonics are $(-1)^J$ and $(-1)^{J+1}$. Thus the vector potential can be separated according to the parity of the radiation wave, one corresponding to an electric field having a parity of $(-1)^{\ell+1}$ while the other representing a magnetic field characterized by a parity of $(-1)^\ell$.

$$\mathbf{A}^E_{LM} = \frac{1}{k_\lambda} \left[\frac{8\pi\omega_\lambda^2}{\ell(\ell+1)R_0} \right]^{\frac{1}{2}} \nabla \times \mathbf{L} u_{\ell m}, \text{ and} \tag{2.2}$$

$$\mathbf{A}^M_{LM} = i \left[\frac{8\pi\omega_\lambda^2}{\ell(\ell+1)R_0} \right]^{\frac{1}{2}} \mathbf{L} u_{\ell m}. \tag{2.3}$$

Now we examine the case of this radiation field in the presence of a nucleus. In this case, the Hamiltonian of the radiation field (H_{rad}) must also include a term for the interaction between the field (H_{int})

and the nucleus (H_{nuc}).[2]

$$\mathcal{H} = \overbrace{\frac{(\mathbf{p} - \frac{e}{c}A)^2}{2M} + V(r)}^{H_{rad}} + \overbrace{\sum_{\lambda} n_\lambda \hbar\omega_\lambda}^{H_{nuc}} + \overbrace{\mu_N \frac{e\hbar}{2Mc}\sigma \cdot \mathbf{B}}^{H_{int}}.$$

For a single quantum emission, the initial state consists of a nucleon in state i and no other quanta. Once the interaction has occurred, all that is left will be a single nucleon in state f and a single quantum state λ. Substituting in the two components of the vector potential (Equations 2.3 and 2.2).[3] The interaction Hamiltonian for both the electric and magnetic vector fields are given by

$$\mathcal{H}_{\mathcal{E}}(\mathbf{A}^*_\lambda) = -\frac{C_\ell e}{Mc}\left(\mathbf{p} \cdot (\nabla \times \mathbf{L}u_{\ell m})^* - \frac{\hbar}{2}\sigma \cdot (\nabla \times (\nabla \times (\mathbf{L}u_{\ell m})^*))\right), \text{ and} \tag{2.4}$$

$$\mathcal{H}_{\mathcal{M}}(\mathbf{A}^*_\lambda) = -\frac{C_\ell e}{Mc}\left(\mathbf{p} \cdot (\mathbf{L}u_{\ell m})^* - \frac{\hbar}{2}\sigma \cdot (\nabla \times (\mathbf{L}u_{\ell m})^*)\right). \tag{2.5}$$

The probability amplitude for a transition characterized by either magnetic or electric fields is given by

$$< f|\mathcal{H}(\mathbf{A}^*_\lambda)|i >= C_{\ell m}(\mathbf{k})\frac{\ell + 1}{(2\ell + 1)!!}\left(\frac{\omega}{c}\right)^l < f|\mathcal{M}^\pi_\lambda|i >, \tag{2.6}$$

where π distinguishes between the electric and magnetic Hamiltonian. More specifically, the probability amplitude for an electric or magnetic transition is given by

$$\mathcal{M}^E = e(r^\ell Y_{\ell m}(\theta, \phi))^* - \frac{i\mu_N e\hbar k}{2Mc(\ell + 1)}(\mathbf{L}u_{\ell m})^*, \text{ and} \tag{2.7}$$

$$\mathcal{M}^M = \frac{e\hbar}{Mc}\left(\left(\frac{1}{\ell + 1}\mathbf{L} \cdot \nabla(r^\ell Y_{\ell m}(\theta, \phi))^*\right) + \frac{\mu_N}{2}\sigma \cdot \nabla(r^\ell Y_{\ell m}(\theta, \phi))^*\right). \tag{2.8}$$

[2] In this formula the effects of the electrons have been intentionally left out.
[3] The effects of the nucleus alone are small and thus will be excluded from the rest of the calculations.

2.2 Reduced Transition Probabilities

The probability of observing a transition from some initial state i to some final state f is given by

$$T_{i\to f} = \frac{2\pi}{\hbar}| < f|\mathcal{H}|i > |^2 \frac{dN}{dE}. \tag{2.9}$$

This relation is known as *Fermi's Golden Rule*, and describes the relationship among the experimentally-determined reaction rate, the transition-matrix elements, and the final density of states [Pov02, Dir95, Fer50]. Substituting in the appropriate matrix elements (see Equation 2.6), as well as our density of states gives into Equation 2.9:

$$T^{\pi\ell}_{i\to f} = \frac{8\pi(\ell+1)}{\ell[(2\ell+1)!!]^2}\frac{1}{\hbar}\left(\frac{\omega}{c}\right)^{2\ell+1} B(\pi\ell, J_0 \to J), \tag{2.10}$$

where $\mathrm{B}(\pi\ell, J_0 \to J)$ is known as the reduced transition probability from some initial state J_0 to some final state J. Recall that $T^{\pi\ell}_{i\to f}$ is the probability for a nucleus in some initial state i to decay to some final state f through some decay channel, this is often described as a decay width Γ. Rewriting Equation 2.10 in terms of Γ, and accounting for the spins of the initial and excited states gives

$$\Gamma(\pi\ell, J_0 \to J) = \frac{8\pi(\ell+1)}{\ell[(2\ell+1)!!]^2}\frac{1}{\hbar}\left(\frac{\omega}{c}\right)^{2\ell+1} \frac{2J_0+1}{2J+1} B(\pi\ell, J_0 \to J). \tag{2.11}$$

In more common notation, the reduced transition probabilities can describe both the entrance and the exit channel of a reactions:

$$B(\pi\ell, J_0 \to J) = B(\pi\ell)\uparrow, \text{ and} \tag{2.12}$$

$$B(\pi\ell, J \to J_0) = B(\pi\ell)\downarrow. \tag{2.13}$$

These two are related by what is known as the spin factor (g) such that

$$\begin{aligned} B(\pi\ell)\uparrow &= \frac{2J+1}{2J_0+1}B(\pi\ell)\downarrow \\ &= gB(\pi\ell)\downarrow, \end{aligned} \tag{2.14}$$

where the $\uparrow$ ($\downarrow$) denotes the reduced excitation (de-excitation) probability. The reduced transition probability for an elastic transition ($J_0 \rightarrow J \rightarrow J_0$) from the ground state to some excited state at E_x is given by

$$B(\pi\ell)\uparrow = \frac{2J+1}{2J_0+1}\frac{\ell[(2\ell+1)!!]^2}{8\pi(\ell+1)}\left(\frac{\hbar c}{E_x}\right)^{2\ell+1}\Gamma_0. \tag{2.15}$$

where the Γ_0 denotes the ground-state decay width. In the case of an even-even nucleus, the reduced transition probabilities are given by

$$B(E1)\uparrow = 2.866\frac{\Gamma_0}{E_x^3} \quad [10^{-3}e^2fm^2]; \tag{2.16}$$

$$B(M1)\uparrow = 0.2598\frac{\Gamma_0}{E_x^3} \quad [\mu_N^2]; \tag{2.17}$$

$$B(E2)\uparrow = 6201\frac{\Gamma_0}{E_x^5} \quad [e^2fm^4], \tag{2.18}$$

where Γ_0 is in meV and E_x is in MeV.

2.3 Total Scattering Cross Section

In nuclear resonance fluorescence a γ-ray excites a nucleus to an excited state at an excitation energy E_x with spin J for a short time before decaying directly or indirectly to the ground state of spin J_0 (see Figure 2.1). The probability of such an interaction is given by the cross section in the Breit-Wigner

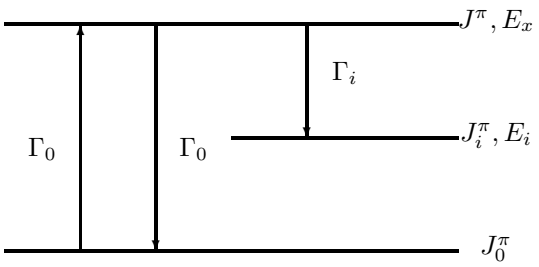

Figure 2.1: The parameters Γ_0 and Γ_i denote the transition widths to the ground state and intermediate levels, respectively. J_0^π denotes the spin and parity of the ground state, while the spins and parities of the excited states are given by J^π and J_i^π.

form [Bet36]:

$$\sigma_{\gamma\gamma}(E,\theta) = \pi\lambda\!\!\!^{-2}\frac{2J+1}{2(2J_0+1)}\frac{\Gamma_0\Gamma_i}{(E-E_x)^2+\frac{1}{4}\Gamma^2}\frac{W(\theta)}{4\pi} \tag{2.19}$$

By setting $\Gamma_0 = \Gamma_i$, Equation 2.19 can also be used to describe elastic scattering. Summing over all the possible decay channels and integrating over all angles gives the the total absorption cross section,

$$\sigma_\gamma(E) = \pi\lambda\!\!\!^{-2}\frac{2J+1}{2(2J_0+1)}\frac{\Gamma_0\Gamma}{(E-E_x)^2+\frac{1}{4}\Gamma^2}. \tag{2.20}$$

When $E \approx E_x$, the cross section is maximized:

$$\sigma_{max} = \pi\lambda\!\!\!^{-2}\frac{2J+1}{2(2J_0+1)}\frac{4\Gamma_0}{\Gamma}. \tag{2.21}$$

The elastic scattering cross section is related to this total absorption cross section according to

$$\sigma_{\gamma\gamma} = \frac{\Gamma_0}{\Gamma}\sigma_\gamma(E). \tag{2.22}$$

Integrating the elastic scattering cross section over energy gives us

$$I_s = \int \sigma_{\gamma\gamma}dE = \frac{2J+1}{2J_0+1}\left(\frac{\pi\hbar c}{E_x}\right)^2\frac{\Gamma_0^2}{\Gamma}. \tag{2.23}$$

Equation 2.23 is called the *integrated scattering cross section*. If the branching ratio Γ_0/Γ is known, the reduced excitation probability (see Equation 2.11) can be rewritten in terms of the integrated scattering cross section. Specifically, in the case of elastic scattering in an even-even nucleus, the reduced transition probabilities are given by:

$$B(E1)\uparrow = \frac{9}{16\pi^3}\left(\frac{\hbar c}{E_x}\right) I_s; \tag{2.24}$$

$$B(E1)\uparrow = 0.2486\frac{I_s}{E_x} \quad [\times 10^{-3} e^2 fm^2];$$

$$B(M1) = 22.533 \times 10^{-3}\frac{I_s}{E_x} \quad [\mu_N^2], \tag{2.25}$$

where I_s is in units of meV b, and E_x is in units of MeV.

2.4 Angular Distribution of Emitted Radiation

The angular distribution function W(θ) for resonantly scattered photons is given by

$$W(\theta) = \sum_{\nu even}^{min(2J,2\ell_1,2\ell_2)} A_\nu(1) \cdot A_\nu(2) \cdot P_\nu(\cos\theta), \tag{2.26}$$

where θ is the scattering angle between the incident and scattered photon, and $P_\nu(\cos\theta)$ are the Legendre functions [Fag59]. The coefficients $A_\nu(1)$ represent the photons in the entrance channel having multipolarity ℓ_1 or $\ell_1' = \ell_1 + 1$ and a mixing ratio δ_1. Likewise, $A_\nu(2)$ describes the scattered photons having multipolarity ℓ_2 or $\ell_2' = \ell_2 + 1$ and a mixing ratio δ_2. The mixing ratios are defined as

$$\delta_{1(2)} = \frac{< \Psi_f | \ell'_{1(2)} | \Psi_i >}{< \Psi_f | \ell_{1(2)} | \Psi_i >}. \tag{2.27}$$

The coefficients $A_\nu(1)$ and $A_\nu(2)$ can be expressed in terms of F-coefficients

$$A_\nu(1) = \left(\frac{1}{1+\delta_1^2}\right)\left(F_\nu(\ell_1\ell_1 J_0 J) + 2\delta_1 F_\nu(\ell_1\ell_1' J_0 J) + \delta_1^2 F_\nu(\ell_1'\ell_1' J_0 J)\right), \text{ and} \tag{2.28}$$

$$A_\nu(2) = \left(\frac{1}{1+\delta_2^2}\right)\left(F_\nu(\ell_2\ell_2 J_f J) + 2\delta_2 F_\nu(\ell_2\ell_2' J_f J) + \delta_2^2 F_\nu(\ell_2'\ell_2' J_f J)\right). \tag{2.29}$$

In the case of pure dipole transitions ($0 \to 1 \to 0$) in an even-even nuclei we get,

$$W_D(\theta) = \frac{3}{4}\left(1 + \cos^2\theta\right), \tag{2.30}$$

while for pure quadrupole transitions ($0 \to 2 \to 0$) the angular distribution is given by

$$W_Q(\theta) = \frac{5}{4}\left(1 - 3\cos^2\theta + 4\cos^4\theta\right). \tag{2.31}$$

The angular distributions are plotted in Figure 2.2. To make spin assignments, radiation is typically measured at two different angles. In this case, however all the detectors are placed at $\theta = 90°$.

The angular correlation measurements described above give information on the spin of the excited state, but they do not provide any information regarding the parity of that state. The problem lies in Equation 2.26, which depends on the angle relative to an axis (defined by the propagation direction of the γ-ray beam) rather than on the angle between the quanta [Fal48, Mye38]. Specifically, the polarization plane of the outgoing wave is determined by the parity selection rule. Recall from Section 2.1 that parity determines whether the outgoing wave is electric or magnetic in character. Since electric and magnetic fields are dual waves, by specifying the polarization of one of the γ-rays, in this case the polarization plane of the incident γ-ray beam, the parity change between the initial and final state can be measured. Modifying Equation 2.26 to include the initial polarization plane of the incident γ-ray beam we get

$$W(\theta,\phi) = W(\theta) + (\pm)_{\ell\prime} \sum_{\nu even}^{min(2J,2\ell_1,2\ell_2)} A_\nu(1) A_\nu'(2) P_\nu^{(2)}(\cos\theta)\cos(2\phi), \tag{2.32}$$

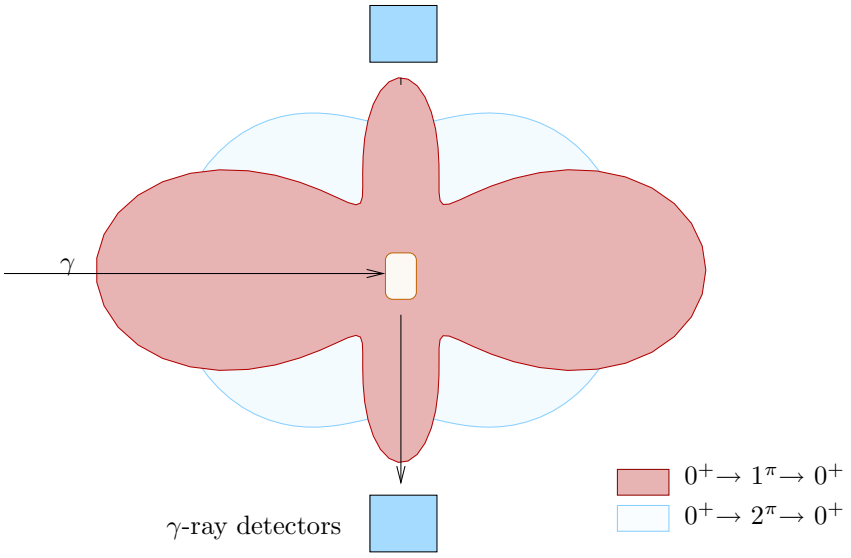

Figure 2.2: Radial plot of the angular distribution functions for pure dipole ($W_D(\theta)$) and quadrupole ($W_Q(\theta)$) ground-state transitions in even-even nuclei. The blue boxes indicate the locations of two of the four γ-ray detectors, which are all placed at $\theta = 90°$.

where θ is the angle between the incident and scattered photons, and ϕ is the angle between the electric vector $\mathbf{E}$ of the scattered photon and the reaction plane (see Figure 2.3) [Fag59]. The coefficient $A_\nu(1)$ is the same as in Equation 2.26, and it still describes the incident radiation. The coefficient $A'_\nu(2)$ is given by

$$A'_\nu(2) = \left(\frac{1}{1+\delta_2^2}\right) - \kappa_\nu(\ell_2\ell_2)F_\nu(L_2\ell_2 J_f J) + 2\delta_2\kappa_\nu(\ell_2\ell'_2)F_\nu(\ell_2\ell'_2 J_f J) + \delta_2^2\kappa_\nu(\ell'_2\ell'_2)F_\nu(\ell'_2\ell'_2 J_f J), \tag{2.33}$$

where κ_ν is the polarization coefficient and depends only on the multipolarity of the radiation [Fag59]. Equation 2.32 differentiates electric and magnetic transitions according to

$$(\pm)_{\ell'_2} = \begin{cases} + & \ell'_2 \quad \text{electric transition,} \\ - & \ell'_2 \quad \text{magnetic transition.} \end{cases} \tag{2.34}$$

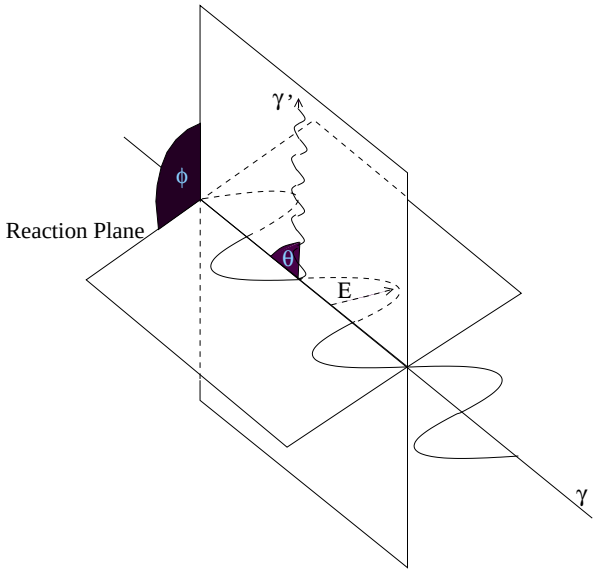

Figure 2.3: Kinematics of scattering process

For the case of a pure dipole excitation and de-excitation, the angular correlation is given by

$$W(\theta, \phi) = \frac{1}{2} + \frac{3}{2}\left(\cos^2\theta - \pi \sin^2\theta \cos(2\phi)\right). \tag{2.35}$$

In the current experimental setup, the γ-ray detectors are placed at an angle of $\theta = 90°$; therefore, Equation 2.35 reduces to

$$W(\theta, \phi) = \frac{1}{2} - \frac{3}{2}\pi \cos(2\phi). \tag{2.36}$$

Figure 2.4 shows the angular distribution function as a function of azimuthal angle for a pure dipole excitation and de-excitation. In the case of the electric-dipole de-excitation, γ-rays are emitted only perpendicular to the reaction plane, while they are emitted parallel to the reaction plane for magnetic transitions. If the reaction plane can be specified for each individual reaction, then the parity of the excited state can be determined by measuring the ratio of γ-rays emitted perpendicular and parallel

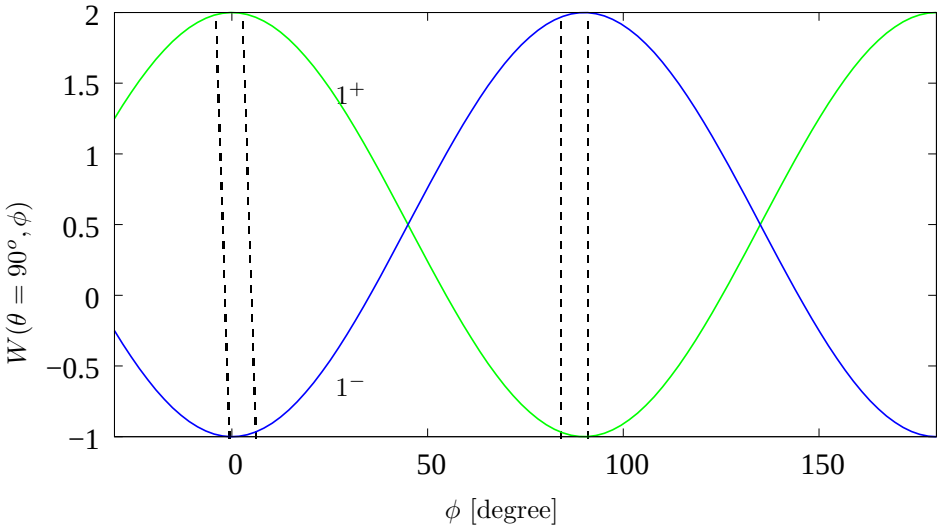

Figure 2.4: Plot of angular distribution as a function of azimuthal angle for a pure dipole excitation and de-excitation. The blue (green) line shows the distribution of a magnetic (electric) dipole de-excitation as a function of angle. The dashed vertical lines indicate the angular acceptance for two of the Ge detectors, this will be discussed in more detail in Section 4.1. At these angles, the two transitions are exactly out of phase with each other.

to the scattering plane as shown

$$\varepsilon = \frac{W(\frac{\pi}{2}, \phi_{\parallel}) - W(\frac{\pi}{2}, \phi_{\perp})}{W(\frac{\pi}{2}, \phi_{\parallel}) + W(\frac{\pi}{2}, \phi_{\perp})}. \tag{2.37}$$

Substituting in Equation 2.36 into Equation 2.37, we get $\varepsilon = +1$ for positive parity transitions ($\pi = +1$) and $\varepsilon = -1$ for negative parity transitions ($\pi = -1$) . Similar results can be obtained for transitions of higher multipolarity. Figure 2.5 shows the three dimensional angular distribution for various spin sequences. These figures all assume that the reaction plane is constant.

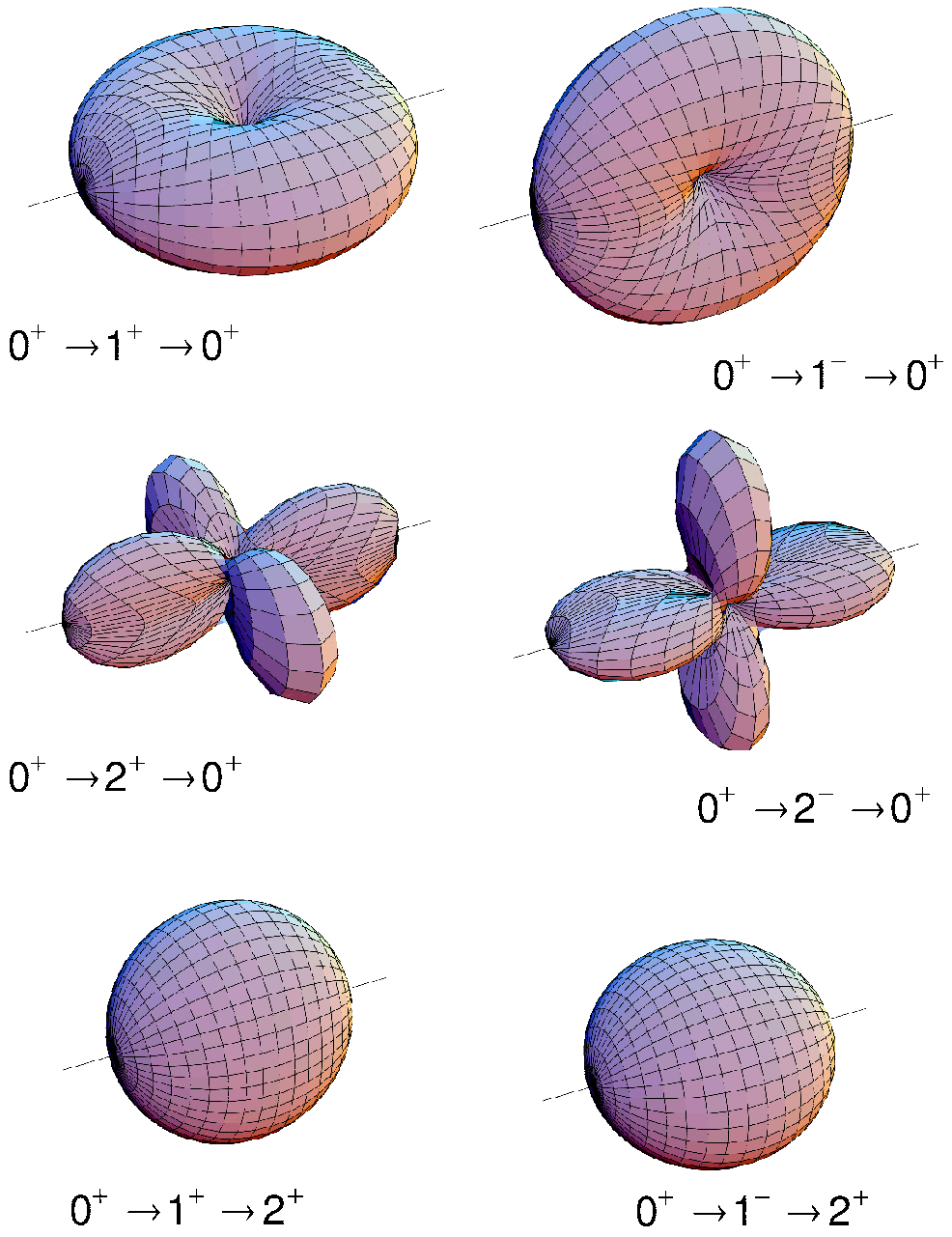

Figure 2.5: Angular distribution correlation $W(\theta, \phi)$, representing the angular distribution of the second γ-ray in the given spin sequence. The distributions for polarized incident γ-radiation are shown

3 Experimental Setup

The inspiration for the Free Electron Laser (FEL)originated in the cosmos, or, more specifically, in the large number of protons and electrons that make up the cosmic radiation [Fee48]. In 1948, Feenberg and Primakoff investigated the absence of these high-energy electrons striking the Earth's atmosphere. Their calculations showed that electrons lose considerable energy to low-energy photons (E $\approx$ 1 eV) from starlight and sunlight. In the frame of the electron, however, these photons are not low energy, and move towards the electrons at much higher energies (E >> 1 eV). They estimated that the electrons could lose upwards of 80% of their initial energy due to Compton scattering off these "red-shifted" photons [Fee48].[1] This same principle lies at the heart of the FEL concept today.

Much of the current groundwork for a terrestrial FEL was done by J.M.J. Madey in 1971 while working at Stanford University [Mad71]. In its very basic form, the FEL consists of three components: an accelerator, an undulator, and an optical cavity [Mar85]. The accelerator is the source of the electrons which are accelerated in bunches before undergoing magneto-bremsstrahlung in the undulator. An optical cavity encompasses the undulator and contains the photons that backscatter off the electrons producing γ-rays.

The photon scattering experiments were performed at the High Intensity Gamma-Ray Source (HIγS) at the Duke FEL in Durham, North Carolina. This chapter is devoted to describing the facility and the setup for the NRF experiments at HIγS.

[1] The term "red-shifted" here refers to the fact these photons are generated from starlight, which is moving away from us, and is therefore red-shifted.

3.1 Characterization of the FEL Beam

After the γ-ray beam passes through the optical cavity, it continues through an Al window and into the open air of the collimator hut. About 60-m downstream from the γ-ray creation point, a collimator (with a diameter of 25.4 mm) further reduces the energy spread of the γ-rays [Ton06], creating a γ-ray beam with a 2% energy resolution.[2] The energy of the γ-rays is measured by a 109-mm long p-type HPGe detector located at the back of the target room. This monitor has a crystal diameter of 96 mm and, relative to a NaI detector, an efficiency of 123%. The efficiency of the detector in the current experimental setup was determined using a combination of measurements from calibrated sources and a Monte Carlo simulation (Geant4) of the detector setup, this will be discussed more in Section 3.2.

The energy distribution of the γ-ray beam is determined by placing the monitor detector directly in-line (θ =0°) with a low-flux γ-ray beam. Figure 3.1 shows a typical spectrum from a beam energy measurement. A Monte Carlo simulation (Geant4) was used to reproduce the beam energy measurement spectrum. An asymmetric Voigt distribution [Saa95] was used as the initial beam profile,

$$GL(x,\sigma,\mu,m) = \frac{e^{\left(-4\ln 2(1-m)\frac{(x-\mu)^2}{\sigma^2}\right)}}{1+4m\frac{(x-\mu)^2}{\sigma^2}}, \tag{3.1}$$

where σ is the full-width-at-half-maximum, and μ is the location of the centroid. The Voigt distribution is simply a Gaussian/Lorentzian distribution; an adjustable parameter m controls whether the peak is a Gaussian (m=0) or Lorentzian (m=1). This line shape is used because of the nature of the FEL beam. The maximum energy γ-ray generated during the Compton scattering process occurs at an angle of $\theta = 0°$. The lower energy γ-rays are scattered at an angle, and are limited by the finite opening of the collimator. The resulting γ-ray energy distribution exhibits a sharp drop at the higher energies and an exponential tailing at the lower energies. In order to take into account this effect,

[2]The energy resoultion depends on the size of the collimator used in the experiment. In this case it was a 25.4-mm collimator, which produced an 2% energy resolution.

Equation 3.1 has to be modified to account for this low-energy tailing [Hed82]:

$$A(x,a,\sigma_{1,2},\mu) = \begin{cases} GL(x,\sigma_2,\mu,m) + b(a)\left(e^{-\left(\frac{2\sqrt{\ln 2}(x-\mu)}{\sigma_2 - a2\sqrt{\ln 2}(x-\mu)}\right)^2} - e^{-\left(\frac{(x-\mu)}{\sigma_2}\right)^2}\right) & x \leq \mu, \\ GL(x,\sigma_1,\mu,m) & x > \mu. \end{cases} \tag{3.2}$$

A(x,a,$\sigma_{1,2},\mu$) is the modified Voigt distribution with an adjustable tail determined by the parameters a and b, where b(a) =$\left(0.7 + \frac{0.3}{a+0.01}\right)$.

Geant4 generates a beam of unpolarized γ-rays randomly distributed within a 1-cm circular plane. The parameters of the incident energy distribution (a,σ_1,σ_2,μ) are adjusted until the simulated spectra match those of the actual spectra. Following its creation at the source, the individual γ-ray is tracked, and the energy deposited at each interaction point is recorded until some critical energy remains or the γ-ray escapes the defined "world" volume, at which point it is "killed" [gnt03]. The simulated particles are able to interact with everything defined within the "world" volume (*i.e.* air, aluminum, *etc.*) through a variety of electromagnetic processes: Compton scattering, photo-electric effect, Rayleigh effect, pair production, multiple scattering, fluorescence and Auger effect, bremsstrahlung and ionization [gnt03]. The parameters for the beam energy measurements are reported in Appendix A.

During production runs, the high flux of γ-rays produced at the FEL would overwhelm the monitor detector at 0°. In order to reduce the incident flux, the detector is moved off-center at an angle ($\theta = 5°$) so that the γ-rays can then be measured indirectly via Compton scattering off a 0.635-cm thick Cu plate (see Figure 3.2). The Cu plate is located 430 cm downstream from the target, the Ge detector is located 158 cm from the Cu plate.

The γ-ray beam profile from the 0° simulation is also used to simulate the off-axis scattering (see Figure 3.3). The flux is determined by taking the ratio of the detected Compton scattered events to the simulated Compton scattered events. Scaling the number of simulated incident γ-rays by this ratio gives us the number of actual incident γ-rays. This procedure has been tested using a well-known cross section in ^{11}B and will be further discussed in Section 4.5.

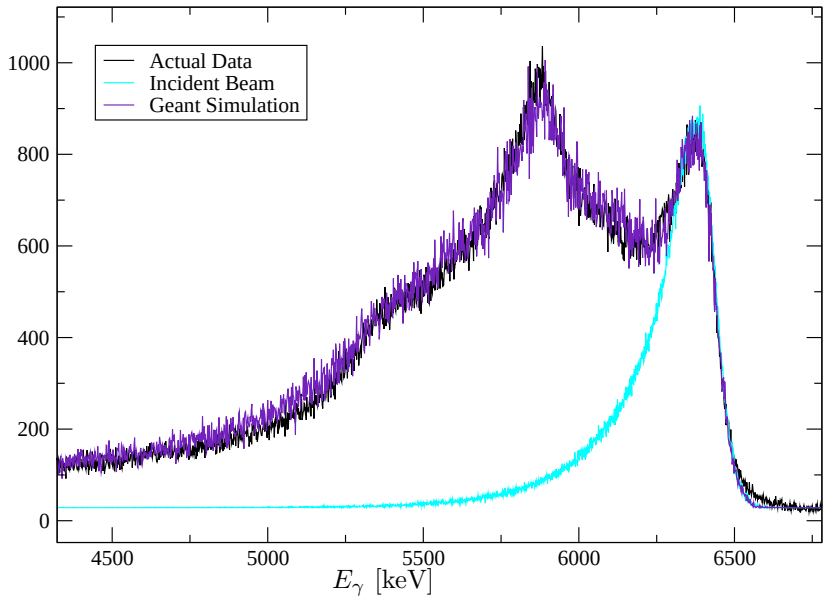

Figure 3.1: Comparison of a beam energy measurement with a Geant4 simulation. The black line shows response of Ge detector at 0° to 6.40 MeV γ-rays. The blue line shows the shape of the simulated incident γ-ray beam. The parameters used for this line shape are: $E_\gamma = 6.387$ MeV, $\sigma_{1,2} = 65$ keV, a=0.34 and m=0.1. The purple line is a Geant4 simulation of the detector's response to the incident beam. The results have been scaled for better comparison with the data.

3.2 Detector Setup for NRF Experiments

To exploit the azimuthal asymmetry of the scattered radiation, four coaxial HPGe detectors are mounted perpendicular to the polarization plane of the γ-ray beam ($\theta = 90°$) approximately 5 m from the end of the collimator. A 1-m plastic tube secures the target at the center of the γ-ray beam. As magnetic-dipole transitions are emitted almost entirely into the plane parallel to the polarization plane, two Ge detectors are placed in the horizontal plane at azimuthal angles of $\phi = 0°$ and 180°. The other two Ge detectors are positioned in the vertical plane ($\phi = 90°, 270°$) for the detection of electric-dipole transitions, which are emitted perpendicular to the polarization plane. The detectors have almost identical crystals of length (78 mm) and diameter (68 mm). Each detector has been characterized as having an efficiency of approximately 60% (relative to 3×3 in^2 NaI(Tl) scintillation crystal) and an energy resolution of around 2 keV at 1.33 MeV. These values are determined under ideal circumstance, and do not relate to the current conditions (see Sections 3.2.1 and 3.2.3). A 10-cm

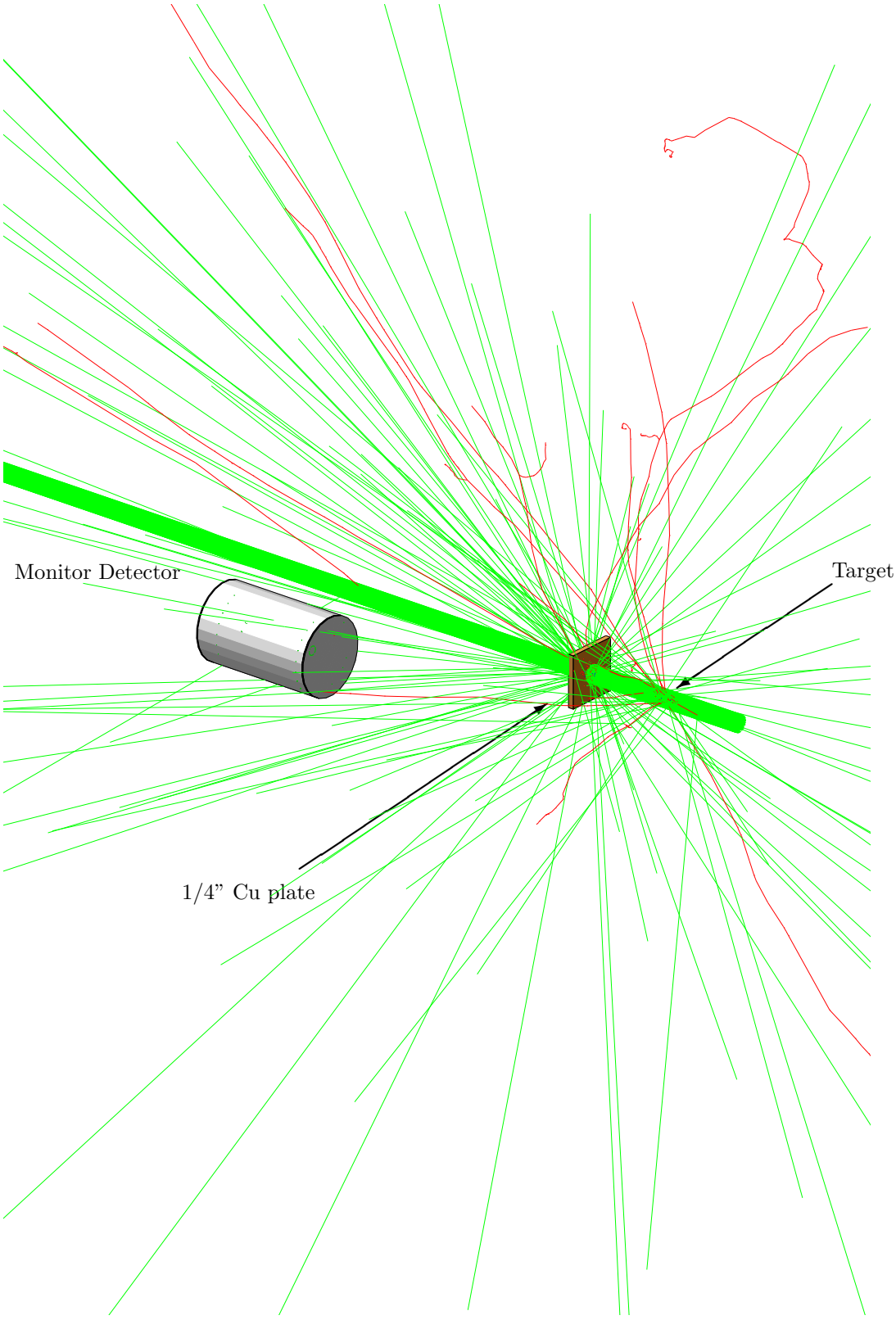

Figure 3.2: The flux measurement setup in Geant4. The setup here consists of the 123% HPGe detector placed 5° off-axis, a Cu plate and a Sn target in the beam. Here, the distances are not to scale for easier viewing. The green lines are γ-rays, and the red lines are the electrons and positrons.

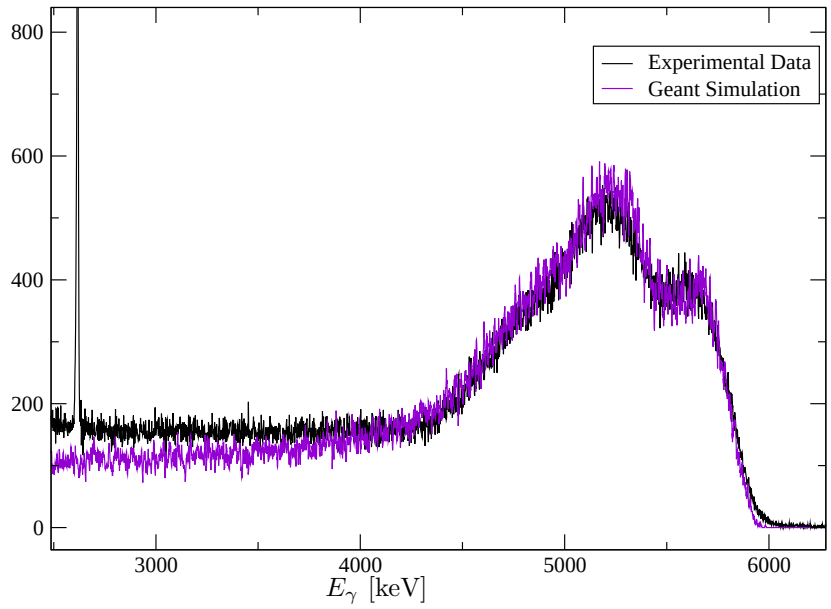

Figure 3.3: Comparison of an off-axis γ-ray flux measurement with a Geant4 simulation. The black line shows response of Ge detector at 5° to 6.40-MeV γ-rays. The purple line is a Geant4 simulation using the energy distribution from the simulated beam energy measurement. The results have been scaled for comparison with the data.

long lead brick wall shields the Ge arrangement from direct radiation from the collimator.

Figure 3.4 shows γ-ray spectra obtained from an 6.9-MeV incident γ-ray beam exciting a ^{124}Sn target. The arrows denote transitions observed in the Gent experiment [Gov98]. The figure on the left shows the summed spectra of the horizontal detectors. At this energy two possible M1 excitations were observed, one of which (6.917 MeV) was observed only in the horizontal plane.

3.2.1 Detector Efficiencies

During the course of the experiment the γ-ray efficiency for experimental setup was measured multiple times using several radioactive sources which are listed, along with their γ-ray transitions, in Appendix B. The efficiency curve in Figure 3.5a was generated using the 19 γ-ray transitions of ^{56}Co. The full-energy peak efficiency is given by

$$\epsilon_{det} = \frac{A_{co}(E)}{R(E)}, \tag{3.3}$$

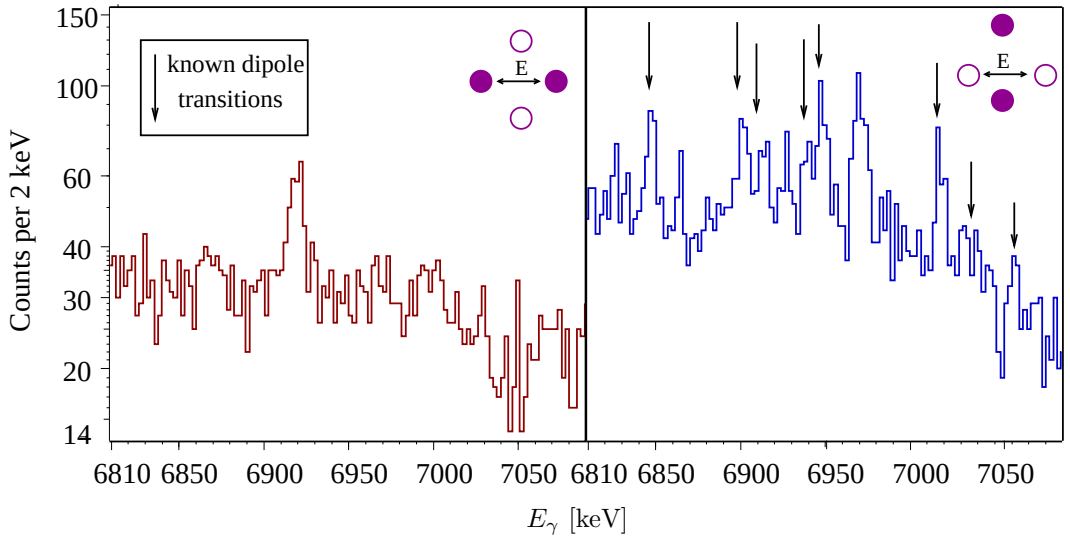

Figure 3.4: NRF spectra observed in the experiment. The arrows denote transitions observed in the Gent experiment[Gov98]. The figure on the right shows the summed spectra observed in two vertical detectors. There is a single M1 transition in this energy range, which is observed only in the horizontal plane.

where $A_{co}(E)$ is the number of counts in the photo-peak at energy E and R(E) is the number of photons of energy E emitted from the source. The efficiency is calculated individually for each detector. To determine the efficiency of the full-energy peak, the number of incident photons emitted from the source must be known. Because there are very few short-lived radionuclide sources of energies extending above 4 MeV, the detector efficiency was modeled using a Monte Carlo simulation (Geant4). Figure 3.6 shows the detector assembly for the 60% Ge detectors, known as the *Star Polarimeter*. This entire configuration was scripted into the Geant4 efficiency simulation. In this figure, a volume radioactive source is simulated at the center of the polarimeter, 5 cm away from the four detectors. The simulation is done with all detectors present to account for cross talk between detectors. In the case of the monitor detector, the radioactive source was placed 158 cm away on the detector side of the Cu plate.

Geant4 begins with the radioactive parent nucleus (^{56}Co in this case), and then randomly selects an excited state in the daughter nucleus (^{56}Fe) to which the nucleus decays [gnt03]. In reality, these excited states are not exactly random. Rather, they are selected according to accepted transition and photon emission probabilities. Once a decay mode is selected, the kinematics of the daughter photons

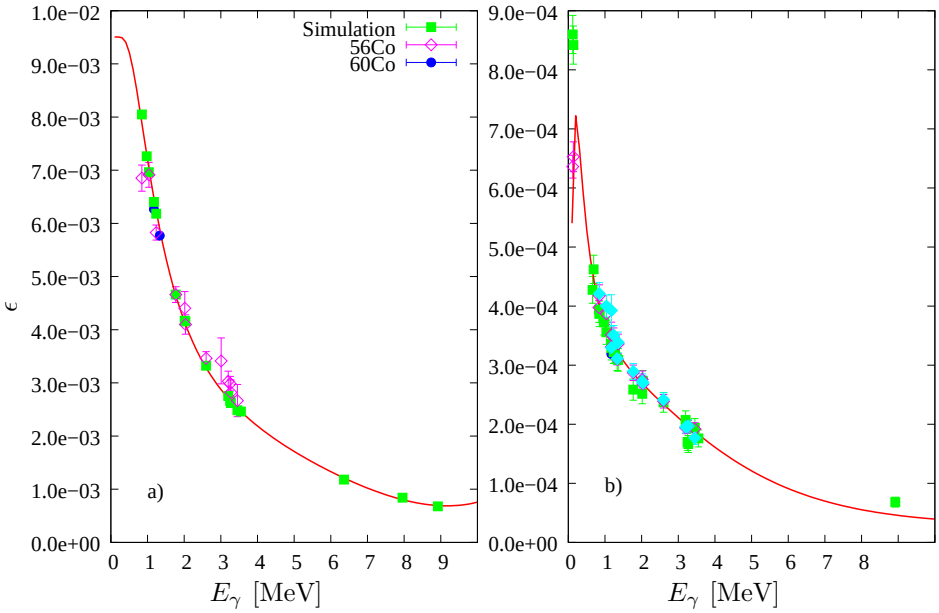

Figure 3.5: Detector efficiency for a single 60% germanium detector (a) and the 123% monitor detector (b). The figure shows the results of the simulated data, and the efficiency measurements made with ^{56,60}Co sources. In the case of the polarimeter, the source placed at the center of the setup 5-cm away from each 60% detectors. In case of the monitor detector, the sources were placed on the copper plate, 158 cm away from the monitor detector. These setup differences account for the higher efficiencies of the 60% detector over the 123% detector. The efficiency curves have been extrapolated out to 9 MeV using the simulated efficiencies.

are generated in the rest frame and then boosted into the lab frame. The simulation does not account for the polarization of the photons in the decay process.

In general, the simulated efficiencies were higher than the measured efficiencies due to a variety of reasons, mostly to an incomplete knowledge of the active volume of the germanium crystal and to its placement within the aluminum casing. To correct for these effects, the simulated efficiencies were scaled to the measured efficiencies. The efficiencies were fit to a curve so that the efficiencies at intermediate energies can be determined with relative ease. The equation describing the efficiencies shown in Figure 3.5 is given by

$$\epsilon_{fep} = \left(aE + \frac{b}{E}\right) e^{\left(cE + \frac{d}{E}\right)} + f, \tag{3.4}$$

where, a, b, c, and d are determined from fits to the experimental data (see Table 3.1). The uncertainty

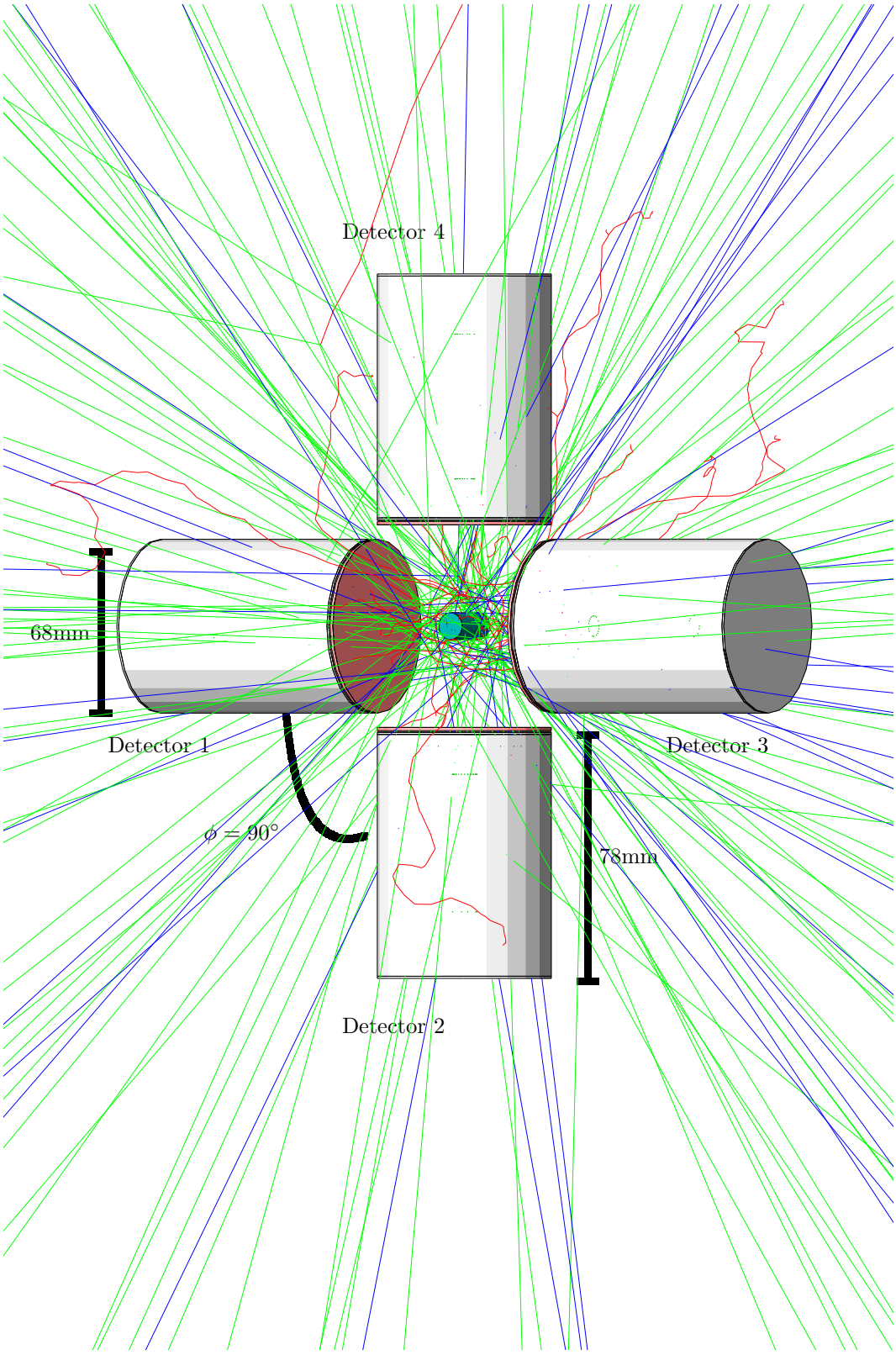

Figure 3.6: Geant4 simulation of the Star polarimeter setup. In this setup, a γ-ray source is placed at the center of the polarimeter, 5 cm away from the detector. The blue lines are γ-rays trajectories, the red lines represent the trajectories of electrons.

Detector	a	b	c	d	f
	1/MeV	MeV	1/MeV	MeV	
1	9.73e-05	-2.31e-02	1.95e-01	-2.65e+00	7.84e-03
2	1.06e-04	-2.53e-02	1.94e-01	-2.73e+00	8.47e-03
3	1.68e-04	-4.07e-02	1.92e-01	-2.65e+00	1.36e-02
4	1.26e-04	-2.93e-02	1.96e-01	-2.66e+00	1.00e-02
Monitor	5.25e-05	7.36e+02	-9.86e-01	-1.81e+05	2.69e-02

Table 3.1: Efficiency parameters for all detectors.

in Equation 3.4 is given by

$$\begin{aligned}\left(\frac{\Delta\epsilon_{fep}}{\epsilon_{fep}}\right)^2 &= \left(Ee^{cE+d/E}\right)^2\sigma_{aa}^2 + \left(\frac{e^{cE+d/E}}{E}\right)^2\sigma_{bb}^2 \\ &+ \left(\epsilon_{fep}c\right)^2\sigma_{cc}^2 + \left(\frac{\epsilon_{fep}}{E}\right)^2\epsilon_{dd}^2 \\ &+ 2\left(e^{cE+d/E}\right)^4\sigma_{ab} + 2\left(cE\epsilon_{fep}e^{cE+d/E}\right)^2\sigma_{ac} + 2\left(\epsilon_{fep}e^{cE+d/E}\right)^2\sigma_{ad} \\ &+ 2\left(\frac{c}{E}\epsilon_{fep}e^{cE+d/E}\right)^2\sigma_{bc} + 2\left(\frac{\epsilon_{fep}}{E^2}e^{cE+d/E}\right)^2\sigma_{bd}. \end{aligned} \tag{3.5}$$

The relative errors on the efficiency measurements are given in section 4.6. The errors associated with the parameters of Table 3.1 are given in Table 3.2.

3.2.2 Electronics Setup

The data acquisition system for one of the five HPGe detectors in the NRF setup is depicted in Figure 3.7. Each HPGe detector has its own internal preamplifier to amplify and to shape slightly the signal. The signal from the preamplifier is analyzed for two major components, the energy of the incident radiation, which corresponds to the amplitude of the pulse and the production time of the signal, determined by the signals rising edge. The preamplifier produces two copies of the same signal, the first of which, the energy signal, is sent to a Spectroscopic Amplifier (Ortec 572) in which the pulse is amplified and shaped before being sent to the Analog to Digital Converter.The second signal, the timing signal, is fed into a Timing Filter Amplifier (TFA Ortec 474) for amplification and shaping before being processed by a Constant Fraction Discriminator (CFD Ortec 935) to eliminate signals

Detector 1

σ_{ij}	a	b	c	d	f
a	1.81e-11	0.00e+00	0.00e+00	0.00e+00	0.00e+00
b	1.83e-09	4.16e-07	0.00e+00	0.00e+00	0.00e+00
c	2.74e-08	4.27e-06	5.47e-05	0.00e+00	0.00e+00
d	3.07e-07	4.40e-05	6.94e-04	1.24e-02	0.00e+00
f	5.37e-10	5.10e-08	1.12e-06	2.31e-05	4.72e-08

Detector 2

σ_{ij}	a	b	c	d	f
a	1.77e-11	0.00e+00	0.00e+00	0.00e+00	0.00e+00
b	2.00e-09	4.81e-07	0.00e+00	0.00e+00	0.00e+00
c	2.51e-08	4.47e-06	4.85e-05	0.00e+00	0.00e+00
d	2.69e-07	4.94e-05	6.17e-04	1.09e-02	0.00e+00
f	4.60e-10	6.20e-08	9.81e-07	2.00e-05	4.07e-08

Detector 3

σ_{ij}	a	b	c	d	f
a	5.11e-11	0.00e+00	0.00e+00	0.00e+00	0.00e+00
b	5.03e-09	1.07e-06	0.00e+00	0.00e+00	0.00e+00
c	4.29e-08	6.25e-06	4.61e-05	0.00e+00	0.00e+00
d	4.73e-07	6.33e-05	5.75e-04	1.00e-02	0.00e+00
f	1.45e-09	1.29e-07	1.63e-06	3.30e-05	1.19e-07

Detector 4

σ_{ij}	a	b	c	d	f
a	2.51e-11	0.00e+00	0.00e+00	0.00e+00	0.00e+00
b	2.56e-09	6.08e-07	0.00e+00	0.00e+00	0.00e+00
c	3.02e-08	4.89e-06	4.90e-05	0.00e+00	0.00e+00
d	3.35e-07	5.09e-05	6.22e-04	1.12e-02	0.00e+00
f	7.39e-10	7.49e-08	1.26e-06	2.63e-05	6.81e-08

Monitor Detector

σ_{ij}	a	b	c	d	f
a	3.73e-12	0.00e+00	0.00e+00	0.00e+00	0.00e+00
b	1.28e-07	6.50e-02	0.00e+00	0.00e+00	0.00e+00
c	-4.50e-08	-2.30e-03	5.61e-04	0.00e+00	0.00e+00
d	-2.09e-04	-1.21e+02	4.05e+00	2.44e+05	0.00e+00
f	6.10e-10	3.90e-05	-7.85e-06	-7.22e-02	1.14e-7

Table 3.2: Efficiency uncertainty parameters for all detectors.

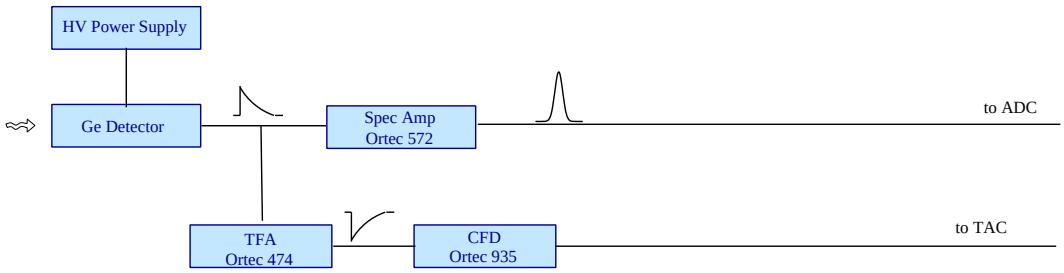

Figure 3.7: Electronics configuration for an individual HPGe detector. This setup is the same for all four 60% detectos and the monitor detector.

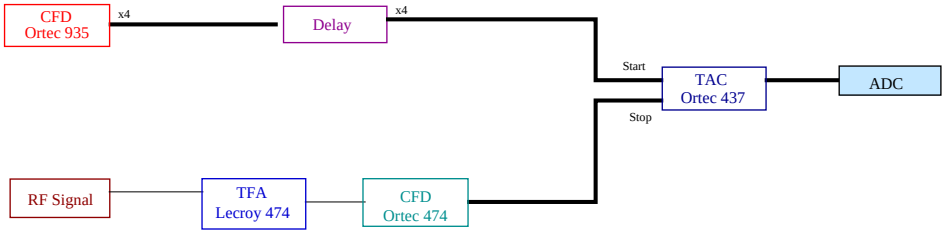

Figure 3.8: The timing signal from each of the 60% detectors starts a Time to Analog Converter (TAC), the stop signal comes from the RF cavity in the storage ring linac. Thicker lines are used to indicate the four signals from the four 60% detectors. The output of the TAC is then digitized by the ADC.

below a certain threshold and provide a clean time reference signal (see Figure 3.7).

The timing signals from the 60% HPGe detectors are fed into a time-to-analog converter (TAC Ortec 437), measuring the time between the production of γ-ray beam in the wiggler and the detection of a γ-ray in one of the 60% detectors. Since electrons do not continuously enter the wiggler, a pulsed γ-ray beam is produced every 179 ns for about 200 ps [Cro01]. The output of the TAC is then digitized by an ADC. Figure 3.9 shows the TAC spectrum, consisting of the number of events versus the time in which an event occurred relative to the RF pulse (or wiggler pulse). Most of the events are related to the beam, and these events correspond to the narrow peak in the center.

A logic OR gate is used to detect the presence of either an energy signal in the monitor detector or a timing signal in one of the 60% detectors (see Figure 3.10). If any of the signals are present, a signal is sent to a scalar (1), where the presence of the event is counted for the purposes of dead time corrections later. A second signal is sent to a second logic gate, where it will pass unaffected unless a

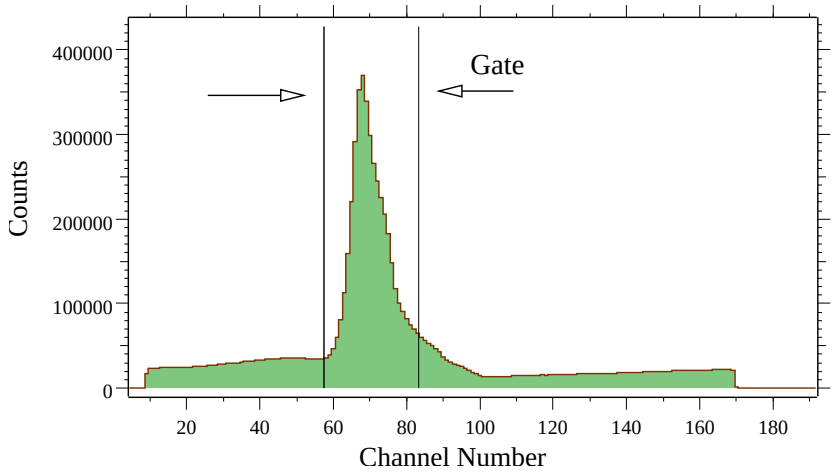

Figure 3.9: Typical TOF spectrum. On the horizontal scale is the time in which an event occurred relative to an RF pulse. A majority of the beam-related events are detected in coincidence with the beam, producing a narrow peak at the center of the spectrum. Excluding events outside of this peak (or setting a gate) can greatly reduce the background counts in a spectrum.

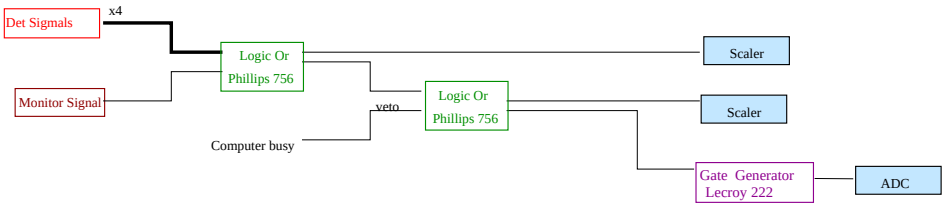

Figure 3.10: In order to avoid unnecessary conversion of data, a gate generator is used to tell the ADC to begin digitizing a pulse. A logical OR gate is used to signal the presence of an event in one the 60% detectors or the monitor. Since the ADC requires several μs to digitize a signal, a second gate is used to prevent signals from triggering the ADC until it is finished digitizing the previous event.

signal is sent by the computer indicating that it is busy writing the previous event. If the computer is not busy, a signal is sent to initiate gates notifying the ADC's that an event is present. A third signal is sent to a scalar (2) indicating that a signal has been processed. The ratio of counts in scaler (2) to scalar (1) gives the ratio of recorded events to total events. The ratio is known as the experimental dead-time.

3.2.3 Detector Calibration

The typical ADC is capable of keeping track of 8192 increments (or channels). As a result, the increments recorded by the ADC do not correspond directly to the energy of the incident photon. The channel numbers in the detector spectrum must be calibrated such that they correspond to the energy deposited in the detector by the photon. In the current experimental setup, a linear relationship between between the channels (x_{ch}) and energies was assumed such that

$$E(x_{ch}) = a + bx_{ch}. \tag{3.6}$$

The ^{40}K and ^{208}Tl background lines (1460.8 and 2614.5 keV respectively) were used as reference energies for the energy calibration of all the runs. Figure 3.11a shows the deviation of the linear fit from the actual energy of γ-rays from known calibration sources. The lower squares are taken from a ^{56}Co source, while the high-energy point corresponds to known transition in ^{11}B. The linear fit accurately reproduces the energies in the region of the background peaks. The calibration procedure seems to experience significant problems at energies much higher than the calibration lines. Since the calibration peaks are very far energetically from the region of interest, very strong ^{124}Sn peaks were included in the energy calibration of the experimental data.

Figure 3.11b shows a plot of the width of the observed γ-ray peaks as a function of γ-ray energy. There is very clearly a pattern of increasing resolution with channel (or γ-ray energy). A quadratic

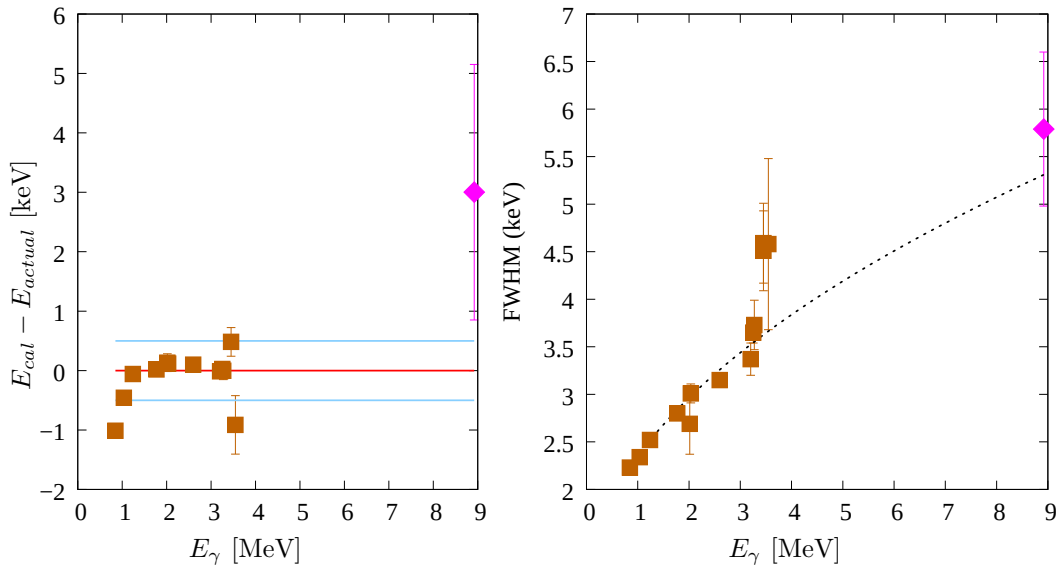

Figure 3.11: The figure on the left shows the difference between the calibrated energies and the established energies of the calibration sources. The figure on the right shows the results of the width calibration. In both figures, the squares correspond to measurements taken using a ^{56}Co source while the diamonds corresponds to an ^{11}B target.

relationship was assumed between the FWHM and the γ-ray energy, such that

$$FWHM(E_\gamma) = a + b\sqrt{E_\gamma}. \tag{3.7}$$

The data points shown in the figure are not all taken during the same run. The lower energy points correspond to a ^{56}Co calibration source, while the high-energy peak corresponds to a well-known transition in ^{11}B. As can be seen in Figure 3.11b, the energy resolution in the laboratory is much worse than the manufacturers quoted resolution of 2.15 keV at 1.33 MeV with a compression rate of 0.2keV/channel. In fact, for the 1.33 MeV peak in ^{60}Co, the resolution was 2.5 keV. This decrease in resolution is due to the high compression of 1.1 keV/channel needed to obtain the energy range of 0.1-9 MeV covered in the current experiment.

4 Data Analysis

All of the important spectroscopic information (J, π, I_s, Γ_0) can all be extracted from observed photo-peak areas. The procedure for extracting these quantities will be discussed in detail in this chapter.

4.1 Parity Measurement

Recall from Section 2.4 that the angular distribution for resonantly scattered photons is given by

$$W(\theta,\phi) = W(\theta) + (\pm)_{\ell\prime} \sum_{\nu even}^{min(2J,2\ell_1,2\ell_2)} A_\nu(1) A'_\nu(2) P_\nu^{(2)}(\cos\theta)\cos(2\phi). \tag{4.1}$$

As discussed in Section 2.4, the angular distribution of emitted γ-rays is strongly dependent on the spin and parity of the initial and final states in the reaction. If the spin and parity of the ground state is known, then the spin and parity of the excited state can be determined by measuring the difference between the number of γ-rays scattered parallel to the electric field vector of the incident photon beam, and those scattered into the perpendicular plane. Such an observable, is termed an *analyzing power*, and quantitatively corresponds to

$$\Sigma = \frac{W(\frac{\pi}{2},\phi_\parallel) - W(\frac{\pi}{2},\phi_\perp)}{W(\frac{\pi}{2},\phi_\parallel) + W(\frac{\pi}{2},\phi_\perp)} = \begin{cases} +1 & \text{for } J^\pi = 1^+, 2^-, \\ -1 & \text{for } J^\pi = 1^-, 2^+. \end{cases} \tag{4.2}$$

In the case of the current experimental setup, four detectors are placed at a scattering angle $\theta = 90°$, and parallel ($\phi = 90°$ or $\phi = 270°$) or perpendicular ($\phi = 0°$ or $\phi = 180°$) to the polarization plane of the incident γ-ray beam. Under ideal circumstances, electric (magnetic) dipole transitions would be detected only in the vertical (horizontal) plane. Factors such as detector solid angle and beam polarization, however, diminish our ability to isolate these scattering planes. Thus, it is more effective to discuss identifying these transitions according to their azimuthal asymmetry, given by:

$$\varepsilon = \frac{N_{\parallel} - r(E_{\gamma})N_{\perp}}{N_{\parallel} + r(E_{\gamma})N_{\perp}} = Q\Sigma, \tag{4.3}$$

$N_{\perp(\parallel)}$ represents the number of counts in the vertical (horizontal) plane detectors and r(E_{γ}) is a normalization factor, correcting for the different responses of the detector pairs. Since the incident photon beam is 100% linearly polarized, the asymmetry is not diminished by the beam. Q is a detector-dependent polarization sensitivity factor that accounts for the finite solid angle of the detectors, and Σ is defined in Equation 4.2. Ideally, Q would be one, however, the finite range of observation angles leads to a reduction in the azimuthal asymmetry. Integrating the angular distribution function over the solid angle of the detectors,

$$< W(\phi) >= \frac{d\Omega}{(\phi_1 - \phi_2)} \int_{\phi_1}^{\phi_2} W(\phi')d\phi', \tag{4.4}$$

where $d\Omega$ is the solid angle subtended by the detector, and ϕ_1 and ϕ_2 correspond to the angular acceptance of the detector. This correction factor amounts to about 0.529 for dipole transitions.

4.2 Peak Counts

Due to the small size of the detectors and the high energies of the γ transitions, a large percentage of the target related γ-rays will escape the detector before depositing all of the their energy. As a result, in the analysis, both the full-energy peaks, as well as, the escape peaks were used in the cross-section calculations. The escape-peak efficiencies were determined in the same manner as the full-energy peak

efficiencies. The total peak area is defined as follows

$$A_T = \frac{N_{fep}}{\epsilon_{fep}} + \frac{N_{esc}}{\epsilon_{esc}}, \tag{4.5}$$

where ϵ_{fep} is the full energy peak efficiency of the detector described earlier in section 3.2, and ϵ_{esc} is the efficiency of the first escape peak. The uncertainty in A_T is given by

$$\begin{aligned}(\Delta A_T)^2 = &\left(\frac{\Delta N_{fep}}{\epsilon_{fep}}\right)^2 + \left(\frac{N_{fep}}{\epsilon_{fep}}\right)^2 \left(\frac{\Delta \epsilon_{fep}}{\epsilon_{fep}}\right)^2 \\ &+ \left(\frac{\Delta N_{esc}}{\epsilon_{esc}}\right)^2 + \left(\frac{N_{esc}}{\epsilon_{esc}}\right)^2 \left(\frac{\Delta \epsilon_{esc}}{\epsilon_{esc}}\right)^2.\end{aligned} \tag{4.6}$$

The peak area and its uncertainty are obtained by integrating over the energy region using the program Tv [Fit00]. The error in the efficiency is calculated using Equation 3.5.

4.3 Determination of Excitation Energies

If a nucleus decays while in motion with respect to an observer, the emitted γ-ray is susceptible to Doppler shifting [Mac70]. In such cases, the energy of the γ-ray (E_γ) observed at an angle θ is related to the energy (E_r) of the absorbed γ-ray by the expression

$$E_r = \frac{E_\gamma^2}{2Mc^2}(1 - 2\cos\theta). \tag{4.7}$$

Once the energies of the resonant peaks have been determined from the calibration procedure described in Section 3.2.3, they can be converted to excitation energies using Equation 4.7. In the case of heavy nuclei such as ^{124}Sn and ^{112}Sn, this correction is not substantial, amounting to 0.31 keV for an 8.4-MeV γ-ray elastically scattering off a resonant level in ^{124}Sn. For the purposes of parity measurements,the NRF measurements are taken with four 60% HPGe detectors at four angles. To reduce the systematic uncertainty, the excitation energies used in this analysis were obtained by taking a weighted average over all detectors.

4.4 Total Scattering Cross Section I_s

The integrated cross section in Equation 2.23 can be related to the number of counts detected at particular energy and angle ϕ according to

$$A_T(E,\phi)dE = N_\gamma(E)N_{tar}I_s(E)\frac{W(\theta,\phi)}{4\pi}dE, \tag{4.8}$$

where A_T is the number of counts detected in the escape and full energy peaks defined in Section 4.2. N_γ is the total number of incident γ-rays corresponding to an energy E_γ $W(\theta,\phi)$ is the angular distribution given in Chapter 2, and N_{tar} is the number of target nuclei in units of atoms/cm^2 given by

$$N_{tar} = \frac{M}{m}\frac{N_A}{S}, \tag{4.9}$$

where M(m) is the mass (molar mass) of the target, N_A is Avogadro's number, and S is the projected area of the target in cm^2 on a plane perpendicular to the γ-ray beam. In the case of an impure sample, the target mass must be corrected to account for the isotopic enrichment of the sample.[1]

The total peak area at a scattering angle ϕ is obtained by integrating over a single resonance.

$$A_T(\phi) = \int_0^{+\infty} A_T(\phi,E)dE = N_\gamma N_{tar} I_S(\phi)\frac{W(\theta,\phi)}{4\pi}. \tag{4.11}$$

Notice that the energy dependence of the incident flux and integrated cross section have been removed. As discussed in Section 3.1, the incident γ-ray beam has some energy distribution, thus the number of incident γ-rays changes depending on the energy. In order to correct for this energy dependence, the N_γ used in equation 4.11 is only a tiny slice of the incident γ-ray spectrum in the energy region of the peak.

[1] For example, the number of target nuclei in a 73% enriched ^{124}Sn target is given by

$$N_{tar} = 0.73\left(\frac{45.62g}{123.905273g/mol}\right)\left(\frac{6.022e23atoms/mol}{\pi(0.795cm)^2}\right) = 8.15\times10^{22}atoms/cm^2. \tag{4.10}$$

The N_γ calculated in Section 3.1 is not the same as the incident flux seen by the individual atoms in the target [Leo94]. In fact, as the γ-rays pass through the target, a certain percentage of them will interact with the target producing low-energy photons and electrons. The measured γ-ray flux is related to the unattenuated beam flux by

$$\frac{N_\gamma}{N}_{\gamma_0} = e^{-\mu x}, \tag{4.12}$$

where $\mu = \rho_{tar}\sigma$ is the total atomic absorption cross section in the target, σ is the total cross section for interaction with the target material in units of cm^2/g. Integrating over the target thickness d gives

$$\begin{aligned} N_\gamma &= N_{\gamma_0} \int_0^d e^{-\mu x} dx \\ &= N_{\gamma_0} \frac{1 - e^{-\mu d}}{\mu d}. \end{aligned} \tag{4.13}$$

In the case of an 8.4 MeV γ-ray beam, 25% of the incident γ-ray will be attenuated by a 45-g, 1.6-cm ^{124}Sn target.

The total cross section is obtained by taking the weighted average of the individual cross sections in all four detectors. The uncertainty in the integrated cross section is given by

$$(\Delta I_s)^2 = \left(\frac{\Delta A_T}{A_T}\right)^2 + \left(\frac{\Delta N_\gamma}{N_\gamma}\right)^2 + \left(\frac{\Delta \Omega}{\Omega}\right)^2. \tag{4.14}$$

4.5 ^{11}B Measurement

As an example of what is involved in a cross-section measurement, and as a preliminary check of the measurement, I will demonstrate the procedure using data taken on a ^{11}B target. The transitions in ^{11}B are very well studied because of their use in flux normalizations at bremsstrahlung facilities [Gov98]. Figure 4.1 shows the observed spectra from 8.3 to 9.0 MeV. The upper plot shows the counts observed in the horizontal plane, while the lower plot shows the counts observed in the vertical plane.

Energy (keV)	J^π	Γ (eV)	Γ_0 (eV)	B(M1) Wu	B(E2) Wu	δ	reference
8920(2)	$\frac{5}{2}^-$	4.37(2)	4.15 (20)	0.28(1)	0.75(2)	-0.11(4)	[Ajz90]
8923.54(79)			3.94(47)				

Table 4.1: The results of the flux calculation (second line) are shown here in comparison with the known properties (first line) of the 8.920 MeV level in ^{11}B. In the first column, the calibrated energy is compared with the known energy. In the fourth column the calculated ground-state decay width is compared with the known value.

The properties for the 8.920 MeV state are shown in Table 4.1. The observed transition is known to be an M1+E2, with an angular distribution shown in Figure 4.2. A ^{11}B target was placed in the beam for approximately 30 minutes.[2] The measured energy distribution of the incident beam is shown on the left in Figure 4.3. The simulated energy spectrum is shown in the same figure along with the corresponding incident γ-ray distribution. In order to determine the optimal beam profile parameters for this distribution, a Geant4 simulation was run using a variety of beam profile parameters, and the detector response was compared with the experimental spectrum. In some cases this procedure took several days.

The figure on the right of Figure 4.3 shows a comparison of the simulated and measured off-axis γ-ray flux. Due to the large number of events, the Geant4 flux simulations were run over several days for each of the 13 beam energies. In the case of the 9.06 MeV beam-energy measurement, the simulated and measured spectra agree considerably well at the high-energy portion of the spectra. At lower incident γ-ray energies, the simulation seems to underestimate the response of the detector. These issues do not occur at lower incident γ-ray energies (see Figure 3.3). Possible sources of disagreement will be discussed in Section 4.6.

The incident γ-ray flux (N_{inc}^{data}) was given by

$$N_{inc}^{data}(E) = N_{inc}^{Sim}(E)\frac{N_{compton}^{data}\epsilon^{sim}}{N_{compton}^{sim}\epsilon^{data}}, \tag{4.15}$$

where $N_{compton}^{data}$ is the number of counts in the full energy Compton spectra, and $N_{compton}^{sim}$ is the cor-

[2]The ^{11}B target was an enriched 20 g cylinder of height 6.35 cm and diameter 1.27 cm

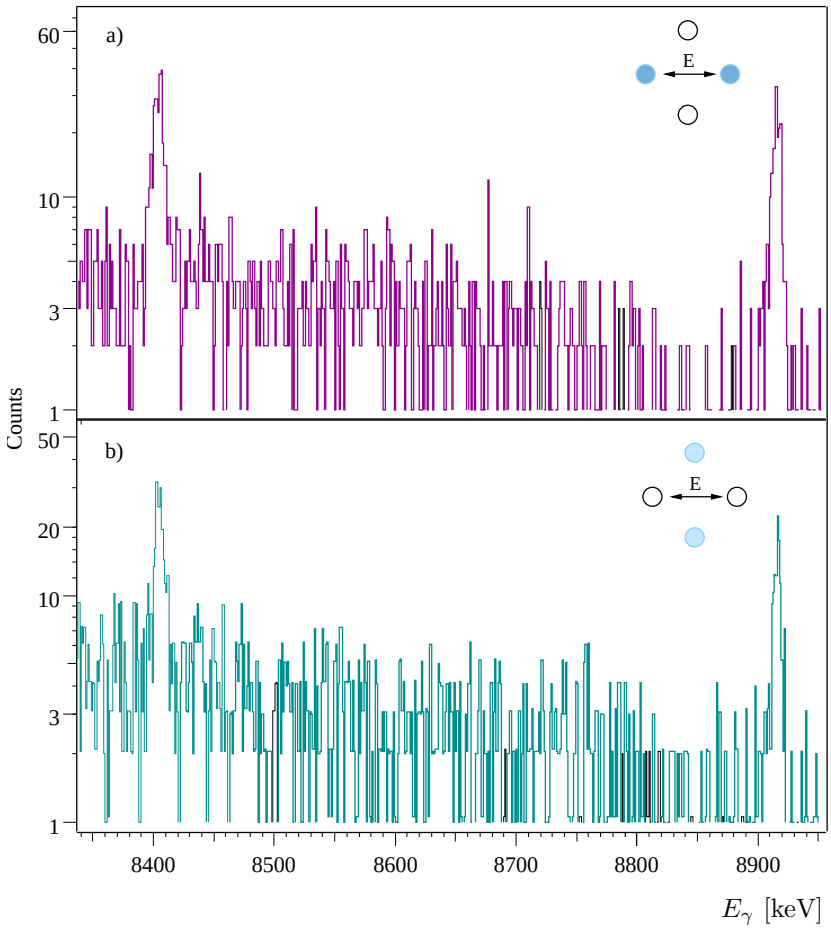

Figure 4.1: Full energy and escape peaks used in the cross-section measurement on ^{11}B. Since this transition is an M1+E2 transition, γ-rays are emitted in both horizontal and vertical planes. Figure a) shows the summed spectra in the horizontal plane, while figure b) shows the summed spectra in the vertical plane.

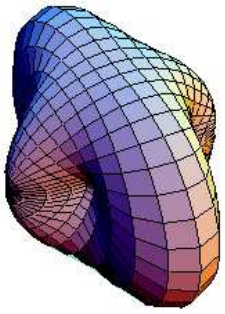

Figure 4.2: Angular distribution correlation function $W(\theta, \phi)$ representing the emitted γ-ray in the decay sequence $\frac{5}{2}^- \rightarrow \frac{3}{2}^-$ observed in ^{11}B.

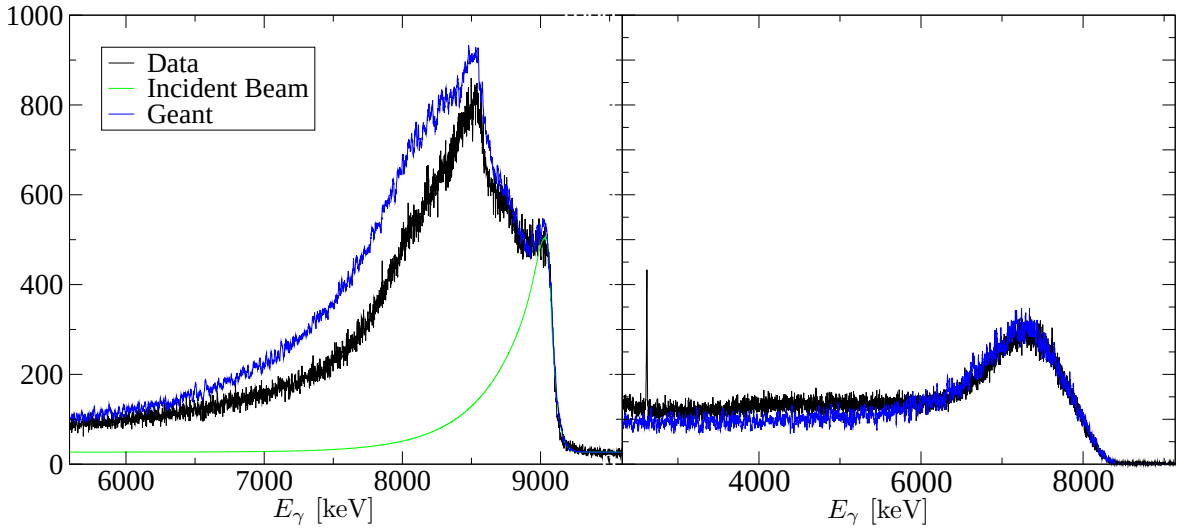

Figure 4.3: The figure on the left shows the simulated detector response to the beam profile along with the actual measurement. The beam profile of a 9.06 MeV γ-ray beam is shown in green. The figure on the right shows the corresponding simulated and measured off-axis spectrum at E_γ=9.06 MeV.

responding number of counts in the Geant4 simulated Compton spectra. Both $N^{data}_{compton}$ and $N^{sim}_{compton}$ are corrected for the efficiencies of the actual detector (ϵ^{data}) and the simulated detector (ϵ^{sim}). The regions of integration are determined to be regions were the simulated and actual data agree closely. $N^{sim}_{compton}$ corresponds to the number of simulated incident counts in an energy region. In this case of this measurement, $N^{sim}_{compton}$ is taken over a 200-keV bin centered at 8920 keV.

The results of the cross-section measurement are shown in Table 4.1. The calculated ground-state decay width was $\Gamma_0 = 3.94 \pm 0.47$ eV, which agrees with measurement in [Ajz90].

4.6 Sources of Error

There are two types of errors associated with any measurement, systematic and statistical. The latter is simply a result of the random fluctuations in the natural world, and can be overcome by repeating the experiment [Bev92]. The former are much more complicated. Systematic errors are associated with the measurement process, and are not necessarily eliminated by repeating the same experiment. An attempt was made to identify all possible sources of systematic errors. The analysis of these

sources are discussed in the following subsections. Table 4.2 and 4.3 give an overview of the percent difference in the statistical and systematic error, respectively. The uncertainties in the statistical error are reported in relative uncertainties ($|\frac{unc}{\text{measured quantity}}|$), while the systematic errors are reported in relative errors ($\frac{(\text{measured value}-\text{adjusted value}}{\text{measured value}}$).

Source of statistical error	FEP%	ESC%
Peak Counts	6	9
Efficiency	2	2

Table 4.2: The first column shows the various components of the total statistical error. The second and third column give their relative uncertainties.

Source of systematic error	relative error
Energy calibration	1.7%
Detector Geometry	1%
Beam profile parameters	5%

Table 4.3: The first column shows the sources of systematic error. The second column details their average relative uncertainties. A discussion of the factors included in each of these estimates are given in the text.

Statistical Error

The statistical error quoted in the measurements has been further analyzed to determine the effects of various aspects of the experiment on the overall error. These aspects are statistical error in the full energy (FEP) and escape peak (ESC) counts and efficiency. The largest source of statistical error is associated with the raw counts in the full and the escape peaks (see Table 4.2) . The error associated with the escape efficiency is higher than the full energy efficiency because of the relatively few peaks available for the escape efficiency calculation. The flux calculations introduced negligible error, less than a tenth of a percent.

Energy Calibration

There are several ways of performing the energy calibration. The program Tv provides an internal calibration tool by fitting a line through two points. There are also external means of calculating the

coefficients of Equation 3.6. When possible, Equation 3.6 was fit to four γ-ray peaks. The first three peaks were background peaks (^{40}K, ^{214}Bi, and ^{208}Tl) while the last peak was a high-energy peak taken from the Gent data. To minimize uncertainties, only intense and isolated peaks from the Gent data were used. In some energy ranges no such peaks were available and the Tv calibration technique was used.

These different calibration methods were applied to the six ground-state transitions observed at 6.4 MeV. The 6.369 MeV Gent peak was used as a high-energy calibration point. The calculated energies were compared with those quoted in the Gent experiment. Calibrating the energies using four lines resulted in the same coefficients for Equation 3.6 as the internal Tv method. Both calibration procedures differ by an average of 1.7% from the Gent energies. The energies resulting from the three peak calibration method were less accurate, experiencing an average difference of 3.7% from the Gent data.

Detector Geometry

The current experimental setup relied heavily on Monte Carlo simulations of both the detector efficiency and the flux measurements. One of the main concerns was an accurate description of the geometries of the various Ge crystals. The manufacturers (Ortec) supplied internal dimensions for each of the detectors; however, some of the details of the detector construction could not be supplied due to company regulations. These issues include the size of the cold finger and the radius of curvature of the rounded corners of the crystal. In addition, the size of the inactive Ge was only estimated ($\approx$ 3 μm for 60% detectors). To estimate the effects of changes in the crystal size on the simulations, the crystal's radius and length were adjusted on one of the 60% detectors. Using the new crystal dimensions, the efficiency was recalculated and compared with the crystal dimensions supplied by the manufacturer. Decreasing the crystal's length by 1-mm resulted in an average difference of 1% from the efficiency simulation using the manufacters specifications.

In addition to a sensitivity to crystal dimension, the geometry of the setup is also an important factor to consider in estimating the error in the Monte Carlo simulations. One of the largest concerns

in this measurement was the location of the center of the γ-ray beam. An alignment laser inside the collimator hut is used to set-up the experimental apparatus. Under ideal circumstances, the center of the laser corresponds with the center of the γ-ray beam. To estimate the effects of a γ-ray beam that is out of alignment with the laser, the distance to the calibration source was varied. Moving the detectors 0.1 cm farther from the source resulted in an average difference in the efficiency of 3%, and a similar difference (3.1%) was observed when the detectors were moved toward the source by the same distance.

Beam Profile Parameters

Essential to the calculation of the integrated cross sections is a precise knowledge of the γ-ray flux. As discussed earlier (Section 3.1), a Monte Carlo simulation was used to determine the initial beam profile. The parameters used in this beam profile were determined by comparing the simulated detector response to the actual response. To estimate the agreement between the two spectra, a chi-squared value was assigned to the various spectra [Tay97]:

$$\chi^2 = \sum_{ch=3000}^{n} \frac{(N_{ch}^{sim} - N_{ch}^{data})^2}{N_{ch}^{data}}. \tag{4.16}$$

N_{ch}^{sim} and N_{ch}^{data} are the number of counts in a single channel of the simulated and actual spectra, respectively. Since the background radiation was not included in the simulation, the spectra were compared above 3 MeV. The results of the comparison are shown in Table 4.4.

The deviations in the simulated detector response from the measured detector response might be due in part to linearity issues in the ADC. The correlation between the ADC channels and measured γ-ray energy were not linear over the entire energy scale for the monitor detector. As a result, the energies of several of the flux measurements had to be scaled by a factor to agree with the actual data. This scaling was not preformed in the initial simulation of the beam energy measurement. As a result, the optimal beam profile parameters might not have been used in these flux measurements. In the future, these effects should be accounted for either by investigating the energy dependence of the

Dec 2004	E_γ MeV	0° spectrum	5° spectrum	xE_γ factor
	8.2	4.26	4.44	0.993
	8.4	14.05	5.58	1.000
March 2005	E_γ MeV	0° spectrum	5° spectrum	xE_γ factor
	6.9	3.95	5.36	0.995
	7.2	7.75	4.01	0.995
	7.5	3.41	4.66	0.99
	7.7	2.67	3.57	0.995
	7.9	6.82	3.41	0.99
Aug 2006	E_γ MeV	0° spectrum	5° spectrum	xE_γ factor
	6.4	4.53	10.72	0.95
	7.0	3.57	2.61	0.96
	7.28	4.26	13.55	0.95
	7.3	10.35	4.50	0.95
	9.0	5.30	14.85	0.96

Table 4.4: Comparison of simulated to measured spectra.

ADC or by incorporating the linearity corrections into the beam energy measurement via an iterative procedure with the flux measurement.

As shown in Table 4.4, the spectra with the largest χ^2 in both the off-axis measurements correspond to the spectra with the largest scaling factors. Since the γ-ray energies had to be scaled in most cases, the beam profile parameters reproducing the on-axis measurements might not correspond to the actual beam. To test the effects of the original beam profile on the resulting cross sections, the width of the beam profile was varied, and the resulting flux spectra were compared with the original beam profile. The profile width of the 6.4 MeV beam profile was varied by 5 keV, a process that resulted in a minimal change in both the on- and off-axis χ^2. In the case of increasing the beam profile width, the on- and off-axis χ^2 changed by 7% and 2%, respectively. Decreasing the beam profile width had much less of an effect on the χ^2, changing the on-axis χ^2 by .04% and having no effect on the off-axis χ^2.

In regards to the cross-section measurements, increasing the beam-profile width from 65 keV to 70 keV resulted in an average difference of 4% for the nine cross-section measurements at 6.4 MeV. The new parameters had very little effect on the most pronounced peaks in the spectra, specifically,

the integrated cross section at 6.387 MeV increased to 481(24) eV b from 473(19) eV b. Decreasing the beam profile width to 60 keV resulted in an average change of 5.2% for the nine calculated cross sections. The integrated cross section at 6.387 MeV changed to 428(19) eV b. The effect was more pronounced at the extremes: the integrated cross section at 6.466 MeV decreased from 126(4) eV b to 110(6) eV b, a 12% deviation from the original value.

4.7 Monte Carlo Simulation of γ-ray Cascades in Photon Induced Reactions

As discussed in Section 2.3, the total absorption cross section is given by

$$\sigma_\gamma = \frac{\pi}{2}\frac{\hbar^2 c^2}{E_\alpha^2}\sum_f \frac{\Gamma_0 \Gamma_f}{(E_\gamma - E_0)^2 + \frac{1}{4}\Gamma^2}, \tag{4.17}$$

where the summation is over the total number of final states available. According to the principle of detailed balance, this cross section is proportional to the de-excitation probability of the same level. In the elastic scattering case, the nucleus decays to the ground state 100% of the time ($\Gamma_0 = \Gamma_f = \Gamma$). At higher excitation energies, however, the excited state tends to decay through multiple intermediate nuclear levels in a process known as nuclear cascading. Such high excitation energies and level densities produce numerous possible decay paths, many of which cannot be detected above the background. One way of correcting for this undetectable strength is to simulate the decay pattern using the statistical model [Bec00].

The DICEBOX program is a Monte Carlo γ-cascade simulator useful in estimating the effects of the statistical behavior of γ-ray cascades through intermediate levels. The main features of the program are described as follows:

- The properties of all the levels below a certain energy (E_{crit}) are supplied to the program. These properties include the energies E, spins J, parities π, branching ratios I, multipole mixing coefficients δ, and the internal conversion coefficients α.

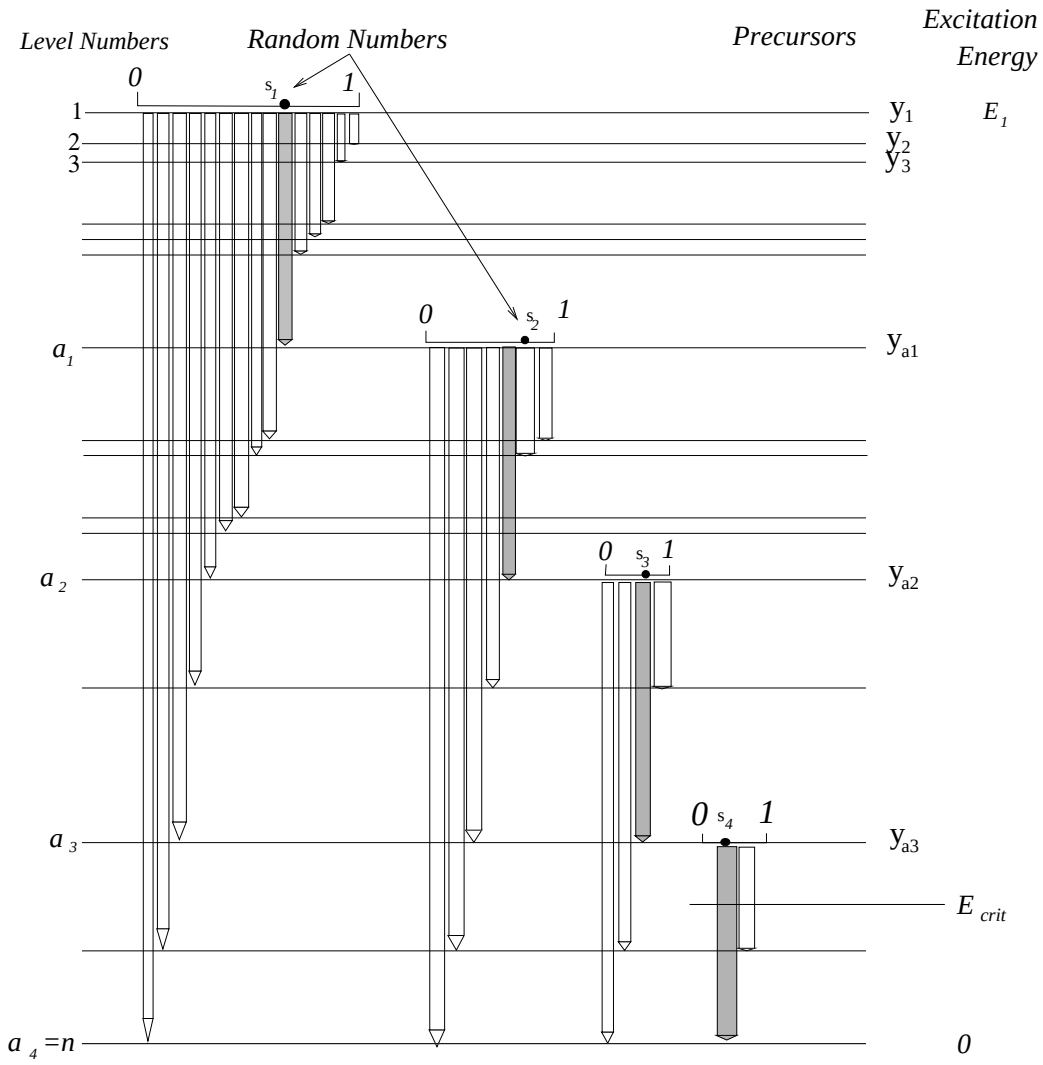

Figure 4.4: Schematic description of the simulated cascade process. The arrows correspond to possible decay paths from each of the exited levels. The shaded arrows correspond to a possible decay pattern from an initially excited state at E_1. E_{crit} represents the region below which the energies E, spins J, parities π, and branching intensities are all known. This figure is adapted from a similar figure presented in reference [Bec00].

- All of the γ-ray cascades begin from a single resonance. The parameters characterizing this initial level are input parameters to the code and include the energy E_1, spin J_1, and parity π_1.

- The intermediate energy levels between the lowest observed state and the excited state (E_1) are generated from either the back-shifted Fermi gas model or the constant temperature formula. These two models are discussed in detail later (see page 52). A generated level scheme is shown in Figure 4.4. The levels are labeled by integers (a=1,...,m) where E_a decreases with increasing a.

- The intermediate partial radiation width $\Gamma_{\alpha,\gamma,b}$ for a γ transition between level a and level b is given by

$$\Gamma_{a\gamma b} = \sum_{X,L} y_{XL}^2 (E_a - E_b)^{2L+1} \frac{S_\gamma^{(XL)}(E_a - E_b)}{\rho(E_a, J_a^\pi)}, \tag{4.18}$$

  where $S_\gamma^{(XL)}(E_a - E_b)$ is the photon strength function for a given γ-radiation of type X (X=E,M) and multipolarity L. These models are discussed in detail below (see page 53), with an overview in Table 4.7. The summation accommodates mixing of the allowed multipolarities. The y_{xl} coefficients are random numbers generated from a normal distribution with zero mean and unit variance, ensuring a Porter-Thomas distribution of the partial widths.

- The total radiation ($\Gamma_{a\gamma}$) for the initial level (a=1) is given by

$$\Gamma_{1\gamma} = \sum_{a'>1} \Gamma_{1\gamma a'}. \tag{4.19}$$

  The sum over $a\prime$ represents the sum over all the possible levels populated by the initial level a=1. The branching ratios for these transitions are defined as

$$I_{1a'} = \Gamma_{1\gamma a'} / \Gamma_{1\gamma}. \tag{4.20}$$

- The generated level scheme is allowed to fluctuate about the nearest-neighbor-spacings of levels with the same spin. These fluctuations are generated according to either a Poisson or a Wigner

distribution:

$$P(x) = \frac{1}{2}\pi x e^{-(\pi/4)x^2} \qquad \text{Wigner distribution,} \tag{4.21}$$

$$P(x) = e^{-x} \qquad \text{Poisson distribution.} \tag{4.22}$$

In the current analysis, the Wigner distribution was used.

A schematic representation of the simulated γ-cascade is presented in Figure 4.4. An input file specifies the parameters and type of level density as well as the incident beam energy and energy distribution. Since each generation of the level density represents only an approximation of the actual level structure, the process is repeated several times.[3] Each new set of level densities and their decay paths is called a *nuclear realization*. Since this process is a Monte Carlo process, each realization must be repeated many times to ensure that the average of the results correspond to the most likely scenario.

Once a realization has been determined, a cascade begins by populating the resonance level. The level a_1, to which this initial state decays, is determined by a random number s_1. If the energy of the final level (E_{a_1}) is the ground state, then the cascade is over. If $E_{a_1} < E_{crit}$, then the branching ratios of the state a_1 are known, and the cascade is over. If $E_{a_1} > E_{crit}$, then another random number s_2 is generated to determine the next populated state a_2. The procedure is repeated until the cascade reaches the final state.

To compare the results of the DICEBOX simulation with experimental results, the efficiency of the detectors are included in the results. The average number of counts in a γ-ray transition was multiplied by the full-energy efficiency at that energy. The procedure for determining the efficiency was discussed in Section 3.2.1.

[3] While formulas are used to specify the number of levels between the E_{crit} and the initial level, the decay widths of the branching ratios for these levels are determined by a random number.

Level Densities

The DICEBOX program allows the user to choose between two level density models, the constant temperature formula and the back-shifted Fermi gas model. The latter is given by

$$\rho(E) = f(J)\frac{e^{2\sqrt{a(E-E_0)}}}{12\sqrt{2}a^{1/4}\sigma_c(E-E_0)^{5/4}}, \tag{4.23}$$

where f(J) is the spin distribution factor assuming a Gaussian distribution of spin projections [Krt02, Gil65], such that

$$f(J) = e^{-J^2/2\sigma_c^2} - e^{-(J+1)^2/2\sigma_c^2} \approx \frac{2J+1}{2\sigma_c^2}e^{-(J+\frac{1}{2})^2/2\sigma_c^2}. \tag{4.24}$$

The spin-cutoff factor, σ_c, is given by

$$\sigma_c^2 = 0.0888A^{2/3}\sqrt{a(E-E_0)}. \tag{4.25}$$

The parameters a and E_0 are determined from fitting the known level densities at low energies. The other level density model, the constant temperature formula (CTF), is given by

$$\rho(E) = \frac{1}{T}e^{(E-E_0)/T}, \tag{4.26}$$

where E_0 and T are parameters that are determined from fits to experimental data. The distribution of levels of a specific spin can be determined by multiplying Equation 4.26 by Equation 4.24. In this model, however, the spin-cutoff factor is energy independent and is given by

$$\sigma_c = (0.98 \pm 0.23)A^{0.29\pm0.06}. \tag{4.27}$$

The CTF is used at the lower energies (4-6 MeV), while the BSFG works better for higher excitation energies. Both models assume that the level density is parity independent. This assumption seems to

BSFG	Nucleus	a (1/MeV)	E_0 [MeV]
	^{112}Sn	12.495	1.124
	^{124}Sn	13.615	1.031

BSFG-ED	Nucleus	a	E_0
	^{112}Sn	13.088	1.124
	^{124}Sn	14.356	1.031

CTF	Nucleus	T	E_0
	^{112}Sn	0.77743	2.800
	^{124}Sn	0.72995	2.994

Table 4.5: Level density parameters for ^{112,124}Sn determined using the procedure defined in Reference [Egi05].

Nucleus	σ_G [mb]	E_G [MeV]	Σ_G [MeV]
^{112}Sn	185	14.92	3.89
^{124}Sn	283	15.19	4.81

Table 4.6: GDR parameters for ^{112,124}Sn taken from [Bel06].

be validated by the pattern of single-particle excitations around the Fermi energy, although in many nuclei the low-energy regions do demonstrate substantial parity dependence [Krt02].

The parameters for Equation 4.26 and 4.23 have been determined for 300 nuclei from s-wave neutron resonance data [Ply00]. Unfortunately, the parameters are not available for ^{112,124}Sn; rather, they have been estimated using the methods described in reference [Egi05]. Table 4.5 gives the estimated parameters and the corresponding level densities in the energy region of interest.

4.7.1 E1 Strength Functions

Six E1 strength functions were used in the DICEBOX simulation. Though, DICEBOX has many different strength function models, only six were used for the purposes of this analysis. The theories behind these models are complicated, and will not be described in detail here.

A. **Single-Particle Model**

The simplest of these models, the Single-Particle estimate (SP) is given by

$$S_{SP}^{E1}(E_\gamma) = const_{E1} A^{2/3}, \tag{4.28}$$

where $const_{E1} = 6.8 \times 10^{-8}\ MeV^{-2}$ [Bla52]. This model is essentially a constant strength function, and it leads to small branching ratios to the ground state.

B. **Brink-Axel Approach**

The most frequently used E1 strength function is the Brink-Axel (BA) model, given by

$$S_{BA}^{E1}(E_\gamma) = \frac{1}{3(\pi\hbar c)^2}\sigma_G \frac{E_\gamma \Gamma_G^2}{(E_\gamma^2 - E_G^2)^2 + E_\gamma^2 \Gamma_G^2}, \tag{4.29}$$

where E_G and Γ_G are the position and half-width of the resonance, and σ_G corresponds to the cross section at the maximum resonance, usually taken to be the giant dipole resonance. The parameters used for ^{124}Sn and ^{112}Sn are given in Table 4.6. The Brink-Axel form of the photon strength function very successfully describes the photo-absorption data of medium and heavy nuclei [Bel06]. The Lorentzian shape of this model, however, fails to describe experimental data close to the neutron binding energy [Kop90].

C. **Kadmenskii, Markushev, and Furman Model**

To deal with this low-energy failure of the Brink-Axel model, the *Fermi liquid model* was used to develop a theoretical description of the spreading width [Krt02, Kad83]. According to this model, which incorporates the effects of quasi-particles, the photon strength function is given by

$$S_{KMF}^{E1}(E_\gamma, T) = \frac{1}{3(\pi\hbar c)^2} F_k \frac{\Gamma_G^2(E_\gamma, T_f)}{E_G(E_\gamma^2 - E_G^2)^2}. \tag{4.30}$$

F_k can be expressed in terms of the Landau-Migdal Fermi liquid force constants, f_1 and f', describing the interaction between quasiparticles such that

$$F_k = \sqrt{\frac{1 + f_1'/3}{1 + f'}}. \tag{4.31}$$

In an analysis of high-energy E1 γ-ray spectra for 20 medium and heavy nuclei, the weighted average of F_k was determined to be 0.62(2) and 0.68(4) for spherical and deformed nuclei, respectively [Mug00]. The factor $\Gamma_G(E_\gamma, T_f)$ is the energy and temperature dependent dampening width given by

$$\Gamma'_G(E_G, T_f) = \frac{\Gamma_G}{E_G^2} \times (E_\gamma^2 + 4\pi^2 T_f^2), \tag{4.32}$$

where T_f is the temperature of the nuclear state at excitation energy E_x, given by

$$T_f = \sqrt{\frac{E_x - \Delta_p}{a}}, \tag{4.33}$$

where a is the level-density parameter described earlier (see Equation 4.26), and Δ_p is the pairing correction. The beauty of this model is its low-energy behavior, specifically, it is the only model discussed so far that doesn't fail in the limit of $E_\gamma \to 0$:

$$\lim_{E_\gamma \to 0} S^{E1}_{KMF}(E_\gamma, T_f) = \frac{1}{3(\pi\hbar c)^2} F_k \frac{4\pi T^2 \Gamma_G^2}{E_G^5}. \tag{4.34}$$

D. **Generalized Lorentzian Model**

One of the main problems with the KMF model (see Equation 4.30) is that, as $E_\gamma \to E_G$, the denominator diverges. Chrien [Kop87] recognized this feature, and by adding Equation 4.34 to

Equation 4.29, achieved an equation that is defined as both $E_\gamma \to 0$ and $E_\gamma \to E_G$:

$$S^{E1}_{GLO}(E_\gamma) = \frac{\sigma_G \Gamma_G}{3(\pi\hbar c)^2} \frac{E_\gamma \Gamma_G(E_\gamma, T_f)}{(E_\gamma^2 - E_G^2)^2 + E_\gamma^2 \Gamma_G^2} + F_K \frac{4\pi^2 T_f^2 \Gamma_G}{E_G^5}. \tag{4.35}$$

This formula is known as the *Generalized Lorentzian Model*. $\Gamma_G(E_\gamma, T_f)$ is defined by Equation 4.32, T_f is defined by Equation 4.33, and F_K is defined by Equation 4.31.

E. Sirotkin Model

Sirotkin [Zar78, Krt02] also proposed a modified version of Equation 4.30. In his modified version, Sirotkin expanded the Fermi liquid theory to include the effects of Pauli-blocking and the behavior of the electromagnetic interaction under time reversal [Zar78, Krt02]:

$$S^{E1}_{Sir}(E_\gamma) = \frac{1}{3(\pi\hbar c)^2} \frac{2e^2\hbar A}{mc} \frac{E_\gamma + F_K^2 E_G^2}{F_K^2 E_G^2 (E_\gamma^2 - E_G^2)^2} \frac{E_\gamma \Gamma'_G(E_\gamma, T_f)}{1 - e^{-E_\gamma/T_f}}. \tag{4.36}$$

The scaling factor, $1 - e^{-E_\gamma/T_f}$, accounts for effect of the temperature on the strength function [Bel06]. Again, $\Gamma_G(E_\gamma, T_f)$ is defined by Equation 4.32, T_f is defined by Equation 4.33, and F_K is defined by Equation 4.31.

F. γ-ray Enhancement Model

The final strength function used in the examination is given by:

$$S^{E1}_{GEM}(E_\gamma) = const_{E1} e^{E_\gamma^2}. \tag{4.37}$$

This strength function has been dubbed the *γ-ray enhancement model* and is purely phenomenological in nature. The factor $const_{E1}$ is the same as in Equation 4.28. This strength function rises exponentially with energy and thus leads to large ground-state branching ratios. Such a quick rise in the strength function with energy is unphysical, but it does provide an upper limit on the ground-state branching and thus a lower limit on the photo-absorption cross-sections.

Single-Particle Estimate (SP)	$S_{SP}(E_\gamma) = 6.8 \times 10^{-8} A^{2/3}$
Brink-Axel (BA) or GDR Lorentzian	$S_{BA}(E_\gamma) = \frac{1}{3(\pi\hbar c)^2}\sigma_G \frac{E_\gamma \Gamma_G^2}{(E_\gamma^2 - E_G^2)^2 + E_\gamma^2 \Gamma_G^2}$
Sir	$S_{Sir}(E_\gamma) = \frac{1}{3(\pi\hbar c)^2}\frac{2e^2\hbar A}{mc}\frac{E_\gamma + F_K^2 E_G^2}{F_K^2 E_G^2 (E_\gamma^2 - E_G^2)^2}\frac{E_\gamma \Gamma'_G(E_\gamma, T_f)}{1 - e^{-E_\gamma/T_f}}$
Kadmenskij, Markushev, and Furman (KMF)	$S_{KMF}(E_\gamma, T) = \frac{1}{3(\pi\hbar c)^2} F_K \frac{C_s E_G \Gamma_G(E_\gamma, T_f)}{(E_\gamma^2 - E_G^2)^2}$ $C_S = \frac{\Gamma_G}{E_G^2}$
Generalized Lorentzian (GLO)	$S_{GLO}(E_\gamma) = \frac{\sigma_G \Gamma_G}{3(\pi\hbar c)^2}\frac{E_\gamma \Gamma_G(E_\gamma, T_f)}{(E_\gamma^2 - E_G^2)^2 + E_\gamma^2 \Gamma_G^2} + F_K \frac{4\pi^2 T_f^2 \Gamma_G}{E_G^5}$
γ-ray Enhancement Model (GEM)	$S_{GEM}(E_\gamma) = 6.8 \times 10^{-8} A^{2/3} e^{E_\gamma^2}$

Table 4.7: Available strength functions for use in DICEBOX code.

4.7.2 DICEBOX Simulation

The continuous nature of the bremsstrahlung beam often makes difficult the process of discerning the decay paths of individual levels, which is necessary for calculating photo-absorption cross-sections. Recently, the ELBE facility in Dresden used a slightly modified version of the DICEBOX code to estimate the branching ratios for ground-state transitions in ^{88}Sr [Sch07]. The cascade simulations were performed for each of the three isotopes with the parameters shown in Table 4.8. An example of the de-excitation spectra is shown in Figure 4.5. The DICEBOX simulation was run assuming the back-shifted Fermi gas model for the level density, the Wigner distribution for the nearest-neighbor spacing fluctuations, and the BA model for the strength function. The parameters for the E1 Lorentzian strength function were obtained by fitting the (γ, n) data from references [Lep71, Gor82] between 13 and 18 MeV (see Table 4.8).

The energy range studied by the ELBE group was 6 to 12 MeV. To speed up the simulation time, the energy regions were divided into 100-keV wide bins. The branching ratio in an energy bin was determined by dividing the number of ground-state transitions ($N_{\gamma i}^{gs}$) by the total number of simulated transitions ($N_{\gamma i}^{all}$). As discussed in Section 2.3, the photo-absorption cross-section is related to the elastic scattering in a bin divided by the simulated branching ration in that bin:

$$\sigma_\gamma^\Delta = \sigma_{\gamma\gamma}^\Delta / b_0^\Delta. \tag{4.38}$$

Level Density Parameters in ^{88}Sr Simulation

Model	a [1/MeV]	Δ [MeV]	Reference
BSFG	8.95(41)	1.97(30)	[Sch07, Egi05]

E1 Photon Strength Function Parameters in ^{88}Sr

Model	E_G [MeV]	Γ_G [MeV]	σ_G [mb]	Reference
BA	16.81(2)	4.0(10	206(2)	[Sch07]

Table 4.8: Parameters used for DICEBOX simulation of ^{88}Sr.

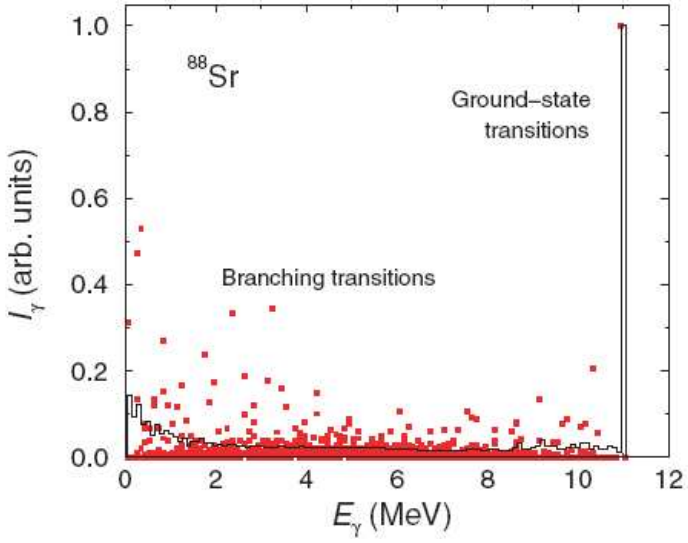

Figure 4.5: DICEBOX simulation of intensity distribution of transitions depopulating levels in a 100-keV bin around 11 MeV in ^{88}Sr[Sch07]. The black line represents the mean distribution of 1000 nuclear realizations. The red squares depict the intensities obtained in 10 individual nuclear realizations.

The photo-absorption cross section for ^{88}Sr are shown in Figure 4.6 along with a previous measurement involving mono-energetic photons [Dat73], and data from (γ, n) measurements [Lep71, Gor82]. The photo-absorption cross sections from the ELBE measurements were consistent with the previous measurements involving mono-energetic photons. In addition, the data show a smooth connection with the (γ, n) data. The success of the ELBE collaboration in comparing its experimental results with other photo-absorption data with DICEBOX encouraged us to perform similar calculations for ^{124}Sn and ^{112}Sn.

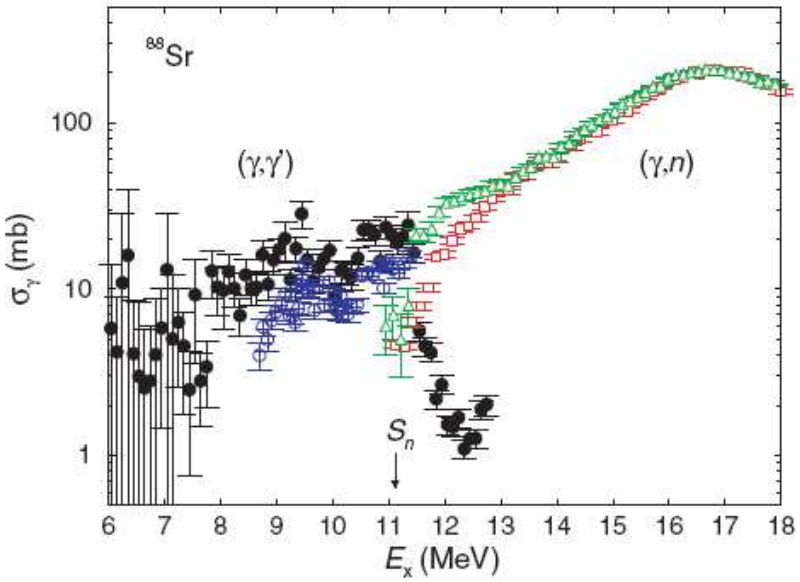

Figure 4.6: Photo-absorption cross-sections deduced from the photon-scattering data for ^{88}Sr[Sch07] according to $\sigma_\gamma = \sigma_{\gamma\gamma}/b_0$ after correction for branching transitions (filled black circles) in comparison with (γ, n) data taken from other mono-energetic photon sources [Lep71, Gor82].

5 Data Analysis Results

The goal of the current analysis is to study the response of a nucleus to absorbed radiation. In theory, this analysis should be easy: the incident radiation transfers energy to the nucleus, and the nucleus occupies some excited energy state for a short time before returning to its initial configuration. Even if the nucleus responds the same way every time it absorbs the radiation, the return to the ground state can proceed in many different ways. To simplify this picture, the de-excitation paths are organized into two groups: elastic transitions and inelastic transitions. The first part of this chapter is devoted to estimating the effects of these inelastic transitions. The second part of this chapter is devoted to determining the spin and parity of the excited levels through polarization measurements of elastic transitions. In the last section, the analysis from the first two sections is combined to produce a comprehensive image of the photo-absorption cross sections of the investigated nuclei. These cross sections will then be compared with the results from the (γ, n) reactions. Lastly, the dipole strength in this region is compared with various theoretical models, shedding light on the specific nuclear configurations characterizing the 6-9 MeV energy region.

Several previous photon-scattering measurements on ^{124}Sn exist below the particle emission threshold. The results of the current work are compared with previous measurements throughout this chapter.

5.1 Low-Lying Dipole Excitations in ^{112,124}Sn

In the case of inelastic transitions, the integrated cross section can , according to [Gov98], be given by

$$I_s = \frac{2J+1}{2J_0+1}\left(\frac{\pi\hbar c}{E_x}\right)^2(\Gamma_0+\Gamma_{feed})\frac{\Gamma_0}{\Gamma}, \tag{5.1}$$

where Γ_0 refers to the ground-state decay width, while Γ_{feed} refers to the inelastic transitions' decay widths from higher lying levels. Of course, Equation 5.1 assumes that the decay pattern of isolated resonances can be determined, which is not always true. If the incident γ-ray beam has an energy spread of ΔE, which can excite m energy levels, the energy-averaged elastic cross section is given by

$$< \sigma_{\gamma\gamma} >= \frac{2J+1}{2J_0+1}\left(\frac{\pi\hbar c}{E_x}\right)^2\left\langle\frac{\left(\frac{\Gamma_0\Gamma_i}{\Gamma}\right)}{D}\right\rangle, \tag{5.2}$$

where D is the average level spacing ($D = \Delta E/m$)[Axe62]. As discussed in Section 4.7, the number of intermediate levels that an excited state can populate is related to the level density of the nucleus. In the case of Sn, there are numerous levels at intermediate energies,[1] and it is very likely that they will be populated, although not frequently enough to exceed the background. Excluding these weak inelastic transitions can cause significant under-estimation of the absorption cross section.

The effect of these inelastic transitions has been investigated using the Monte Carlo simulation DICEBOX discussed in Section 4.7. Of particular interest here is understanding the properties of these inelastic transitions and their expected decay paths. Figure 5.1 shows the probability for various n-step de-excitations as a function of n for the various γ-ray strength function models at the various energies.[2] A transition that decays directly to the ground state is considered to be a one-step cascade. A high-lying state populating an intermediate state that then de-excites directly to the ground state is a two-step cascade. If an inelastic transition populates any more intermediate levels, then the energies of the transitions in these cascades become smaller and less likely to be detected. In terms of energy

[1] Intermediate energies refer to the energy range between the incident γ-ray beam energy and the first excited state.
[2] Appendix E shows the detailed results of this study in both ^{124}Sn and ^{112}Sn. Only an overview of these results has been presented here to preserve the flow of ideas.

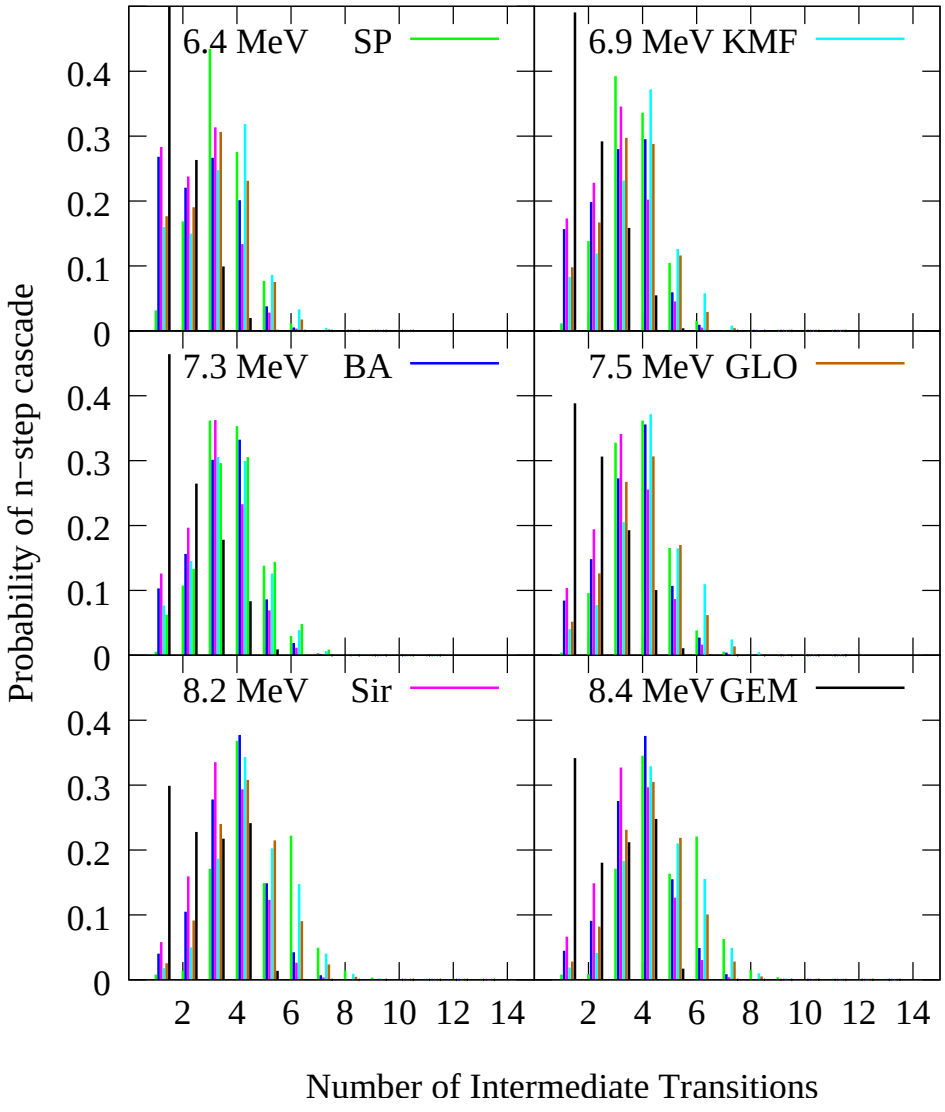

Figure 5.1: Average number of transitions needed to get to the ground state in ^{124}Sn for various models. All the models seem to prefer 4-step cascades in decaying to the ground state, although lower energies show a higher probability of cascades that involve fewer than four-steps. Table E.1, in Appendix E, gives the average number of transitions for each model as a function of energy.

dependence, most of the models seem to prefer three- or four-step cascades in decaying to the ground state. The two extreme models, the SP and GEM models, do not exhibit this pattern. In the case of the SP model, direct decays to the ground state almost never happen, while in the case of the GEM model, these transitions occur between 30 to 50% of the time. The hope is that these multi-step cascades eventually converge at some lower energy, populating one low-energy state frequently enough for detection.

As discussed in the Chapter 1, the Gent group attributed a considerable amount of the strength to inelastic decays (see Table 5.1) [Gov98]. The transitions feeding these levels could not be directly measured in the Gent experiment due to the nature of the bremsstrahlung beam. The continuous energy of the bremsstrahlung beam is such that these intermediate transitions can be both directly populated by the beam and indirectly by the higher-lying levels. The feeding widths are determined by comparing decay widths at higher endpoint energies to ground-state decay widths at lower energies, which are assumed to be populated by the γ-ray beam only. The Gent group estimated that the average branching ratio for ground-state transitions was 72% [Gov98].

E_x (keV)	J_π	Γ_0(4.1 MeV) (meV)	Γ_{feed}(7.5 MeV) (meV)	Γ_{feed}(10 MeV) (meV)
1132	2^+	0.49(7)	16.3(18)	88.5(91)
2426	2^+	0.62(16)	18(3)	84.2(79)
3214	2^+	10.4(13)	13(3)	27.5(27)
3264	2^+		7.9(17)	21.6(28)
3490	1^-	90.2(98)	14(11)	57(11)
3697	1	13.3(21)	11(6)	54(6)
3710	2^+	8.6(14)	7(4)	46(7)
3762	2^+		10.4(29)	32(6)

Table 5.1: Feeding of intermediate levels as a function of maximum bremsstrahlung energy in the Gent experiment [Gov98]. The feeding widths of these levels are determined by examining the decay width at different endpoint energies. The third column gives the decay widths when the levels are directly populated by the γ-ray beam. Columns four and five give the increased decay widths that are believed to be attributed to inelastic transitions from higher energies. Only the first excited state was observed in the current experiment with any statistical certainty.

As discussed in Section 3.1, the HIγS facility produces a nearly mono-energetic beam; therefore, any levels populated below the beam energy can be attributed to inelastic transitions. In the case of

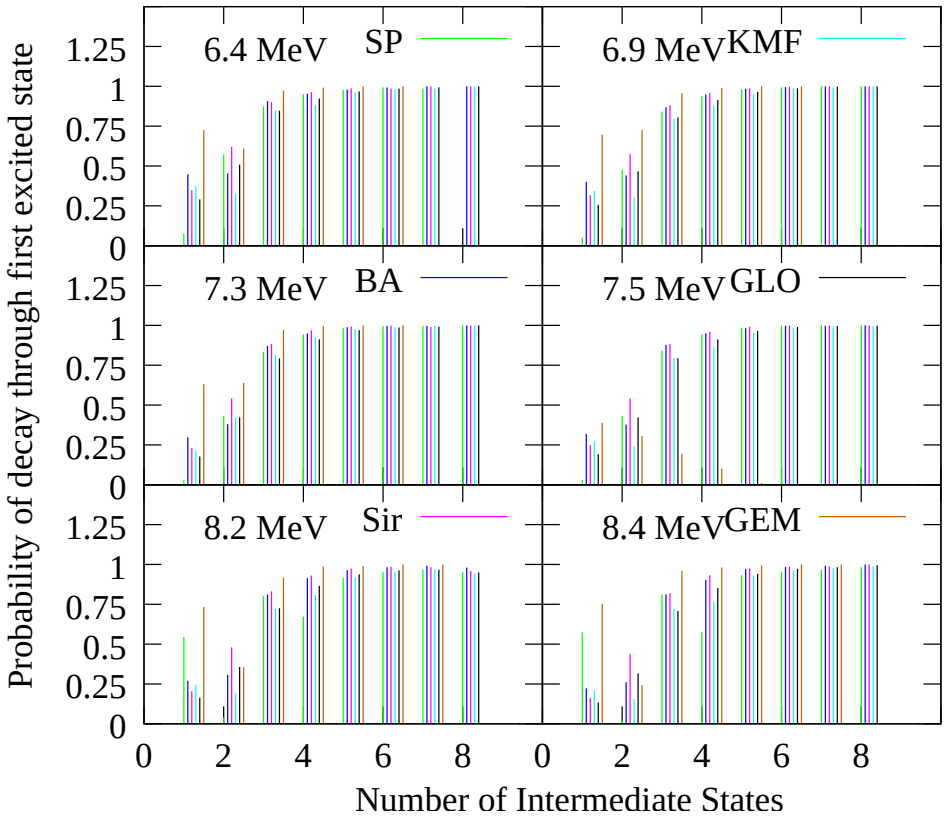

Figure 5.2: Probability of decaying through 2_1^+ in ^{124}Sn as a function of intermediate states. All the models seem to indicate the low probability a two-step decay going through the first excited state. Cascades involving more than three steps almost always populate the first excited states.

^{124}Sn, the observed decay pattern can be compared with the estimated feeding of low-lying levels from the Gent experiment. Most of the levels listed in Table 5.1 were not seen in the present experiment. In fact, the only low-lying transition observed with any statistical certainty was the decay from the first excited state to the ground state ($2_1^+ \rightarrow 0^+$). How was this state populated? Did a state directly populated by the γ-ray beam decay to the first excited state, or are more transitions involved? Figure 5.2 shows the probability of populating the first excited state as a function of the number of intermediate states for ^{124}Sn. All of the strength function models predict that de-excitations involving three or more intermediate states populate the first excited state between 80-100% of the time. In the case of one or two intermediate states, the models predict populating the first excited state between

25 to 50 % of the time. The two- and three-step cascades are much more likely at the lower energies; occurring 68% of the time at 6.4 MeV compared with 33% of the time at 8.4 MeV. Specifically, a decay path that populates only the first excited state before decaying to the ground state occurs 8% of the time at 6.4 MeV, and 3% of the time at 8.4 MeV. The experimental data on ^{112}Sn seem to support this, direct transitions ($E_x - 1256$ keV) were not observed in the experimental spectra. Such a direct examination was not possible in ^{124}Sn because the energy region of decays to the first excited states (E_x - 1132 keV) overlaps with the double escape peaks from the ground-state transitions (E_x - 1022 keV).[3] The broadening of the double escape peaks, coupled with the Compton background obscures these peaks.[4]

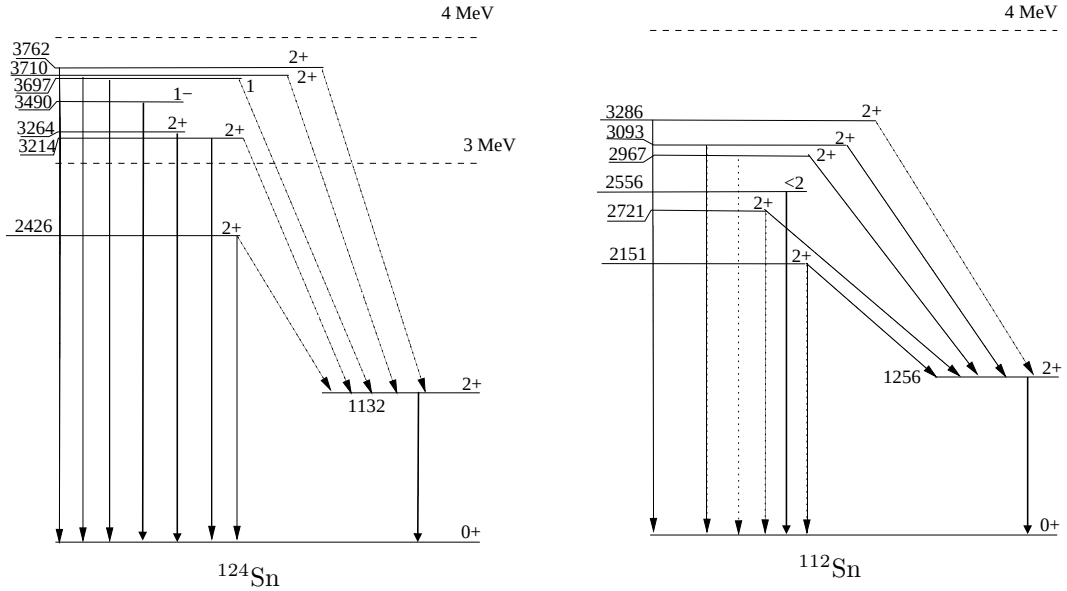

Figure 5.3: Low-lying transitions in ^{124}Sn and ^{112}Sn. In the case of ^{124}Sn, the majority of states below 4 MeV decay predominantly through the first excited state. Decays to these states,therefore, are accounted for by estimating the strength in the first excited state. The opposite was the case for ^{112}Sn, here below 4 MeV, most of the states decay directly to the ground state. In this case, the de-excitation transition strength would be lost.

While the individual decay paths populating this first excited state cannot be discerned, the average

[3] If a 511-keV γ-ray escapes the HPGe detector, the energy of the observed peak is E_x-511 keV, where 511 keV is the rest-energy of the electron. If two γ-rays escape the detector, the observed peak energy is E_x-1022 keV, or two times the rest-energy of the electron.

[4] For an example of the issues surrounding the investigation of these transitions, see Appendix F, Figure F.4.

strength in this decay channel can be determined using Equation 4.8,

$$A_T(E,\phi) = N_\gamma N_{tar} I_s \frac{W(\theta,\phi)}{4\pi}. \tag{5.3}$$

Here, A_T refers to the counts in the first-excited state peak, and N_γ refers to the total incident flux. In addition, since the polarization of the initial γ-ray populating this state was lost, the angular correlation W is taken to be isotropic. Table 5.6 give the observed de-excitation cross section for the 2^+state, while Table 5.2 gives the ratio of ground-state transitions to overall observed transitions as a function of incident beam energy.

^{124}Sn	E_x		$B = I_{gs}/(I_{gs} + I_{2_+})$ [%]					
	(keV)	data	SP	BA	Sir	KMF	GLO	GEM
	8.4	63(1)	12(3)	46(8)	63(13)	25(6)	34(7)	89(9)
	8.2	62(1)	17(4)	53(7)	69(11)	32(7)	41(7)	92(2)
	7.9	64(1)	18(8)	50(16)	63(20)	31(13)	38(15)	98(29)
	7.7	72(1)	32(13)	65(16)	74(17)	47(15)	54(16)	92(5)
	7.5	75(1)	8(5)	65(7)	75(12)	45(11)	52(10)	93(2)
	7.3	78(1)	10(4)	68(10)	76(14)	61(11)	56(11)	94(3)
	7.2	78(1)	15(5)	76(6)	81(13)	70(6)	66(7)	95(2)
	7.0	77(1)	20(4)	80(7)	85(13)	75(10)	70(13)	92(11)
	6.9	73(1)	24(14)	76(19)	80(20)	64(19)	65(22)	90(19)
	6.4	87(2)	42(13)	86(14)	87(19)	77(15)	79(15)	95(13)
	$\sum_{E_x} \frac{(B_{data} - B_{model})}{\sqrt{\sigma^2_{data} + \sigma^2_{model}}}$		36	6	1	12	17	-12
^{112}Sn	E_x		$B = I_{gs}/(I_{gs} + I_{2_+})$ [%]					
	(keV)	data	SP	BA	Sir	KMF	GLO	GEM
	9.0	0(0)	13(9)	40(19)	48(21)	56(24)	37(19)	83(20)
	7.2	76(22)	52(11)	78(10)	79(13)	81(15)	70(11)	94(4)
	6.8	74(17)	58(13)	79(13)	79(13)	81(17)	70(14)	94(8)
	6.4	88(40)	64(12)	81(12)	80(12)	82(17)	73(12)	93(11)
	$\sum_{E_x} \frac{(B_{data} - B_{model})}{\sqrt{\sigma^2_{data} + \sigma^2_{model}}}$		5	0.12	0.10	1	2	-5

Table 5.2: Observed and simulated properties of the 2_1^+ state in ^{112,124}Sn. Shown here are the number of ground state decays normalized to the number of decays to the ground- and first-excited states.

Though Equation 5.3 can account for the decay paths that pass *through* the first excited state,

calculating the *total* inelastic cross section requires knowing what percentage of these inelastic transitions never populate the first excited state. Because these inelastic transitions cannot be measured directly—they are hidden by significant background—their contribution to the total inelastic cross section must be estimated indirectly. Returning to our discussion of the DICEBOX results shown in Figure 5.2 and Figure 5.1, the total observed strength can be calculated by multiplying the probability for an n-step transitions to occur by the probability that the first excited state is populated in the de-excitation (see Figure 5.4). For most of the strength functions, between 60% and 90% of the total strength can be found in the ground- and first-excited state transitions. In fact, neglecting the two extreme models, the SP and GEM, the strength functions differ from each other by about 1%.

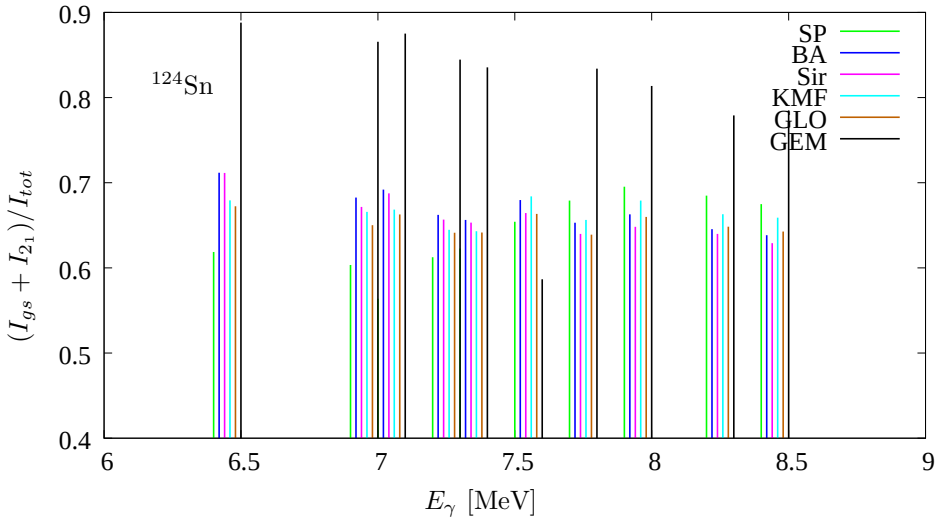

Figure 5.4: Percentage of total intensity in the 2_1^+ and ground-state transitions for various models in ^{124}Sn. A similar figure for ^{112}Sn can be seen in Appendix E, Figure E.4.

Figure 5.5 shows the ratio of the intensity of the ground-state transitions (I_{gs}) to the total observed intensity for all transitions (I_{tot}). In both nuclei, the experimental branching ratio decreases slowly as a function of energy, decaying to the ground state between 80% and 65% of the time. As we approach the neutron emission threshold, both nuclei show a slight increase in inelastic transtions through the 2_1^+ state (I_{2_1}). A trend that was amplified in ^{112}Sn. The 9.0 MeV γ-ray beam yielded no transitions to the ground state, while the 6.4 MeV γ-ray beam yielded mostly transitions to the ground state.

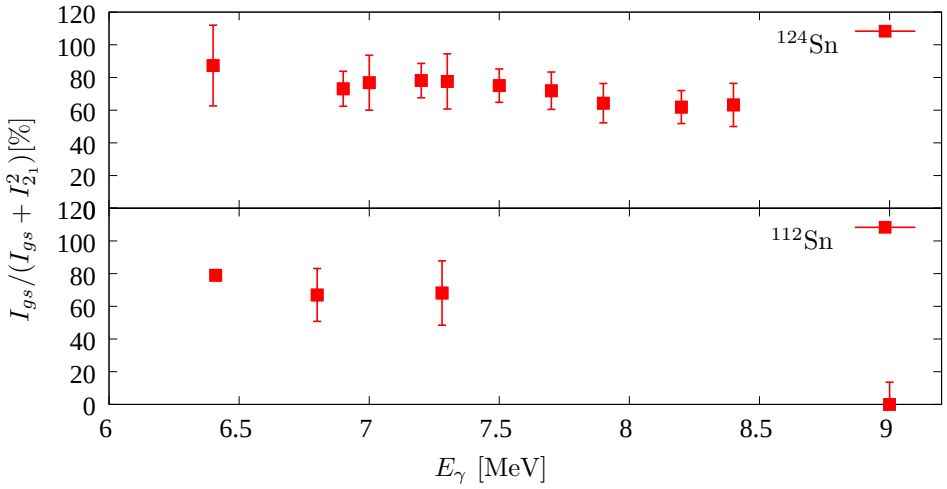

Figure 5.5: Comparison of partial widths Γ_0 of ground-state transitions and branching ratios for ^{124}Sn and ^{112}Sn.

As with the experimental data, the various models predict a slight shift from elastic ground-state decays to inelastic transitions through the 2_1^+ state with increasing energy. The increase of inelastic decays with energy is most likely due to the higher level density at higher energies. At 6.4 MeV there are fewer states available for these inelastic transitions than at 9.0 MeV. The enhancement of these inelastic transitions at 9.0 MeV is doubtful. The most likely explanation for the lack of elastic transition strength is the background. There was considerable background at the higher energies due to Compton scattering in the air and problems with the electronics. Overall, the background counts increased from around 4 counts-per-channel to 20 counts-per-channel at 9.06 MeV.

Returning to the subject of branching ratios, the model predictions have been compared to the measured ratio of ground-state transitions to the ground- and first-excited state transitions (see Table 5.2). The extreme models, the SP and GEM, do not seem to correspond to the data. In the case of the SP model, this model predicted significantly more decays to intermediate transitions than were observed. In the case of the GEM model, decays directly to the ground state were dominant at all energies, again a situation that was not observed in the experimental data. While the remaining four models seemed in agreement in the low-energy region, most slowly began to deviate as the energy increased. The GLO and KMF models both predicted a much faster decrease in the branching ratio

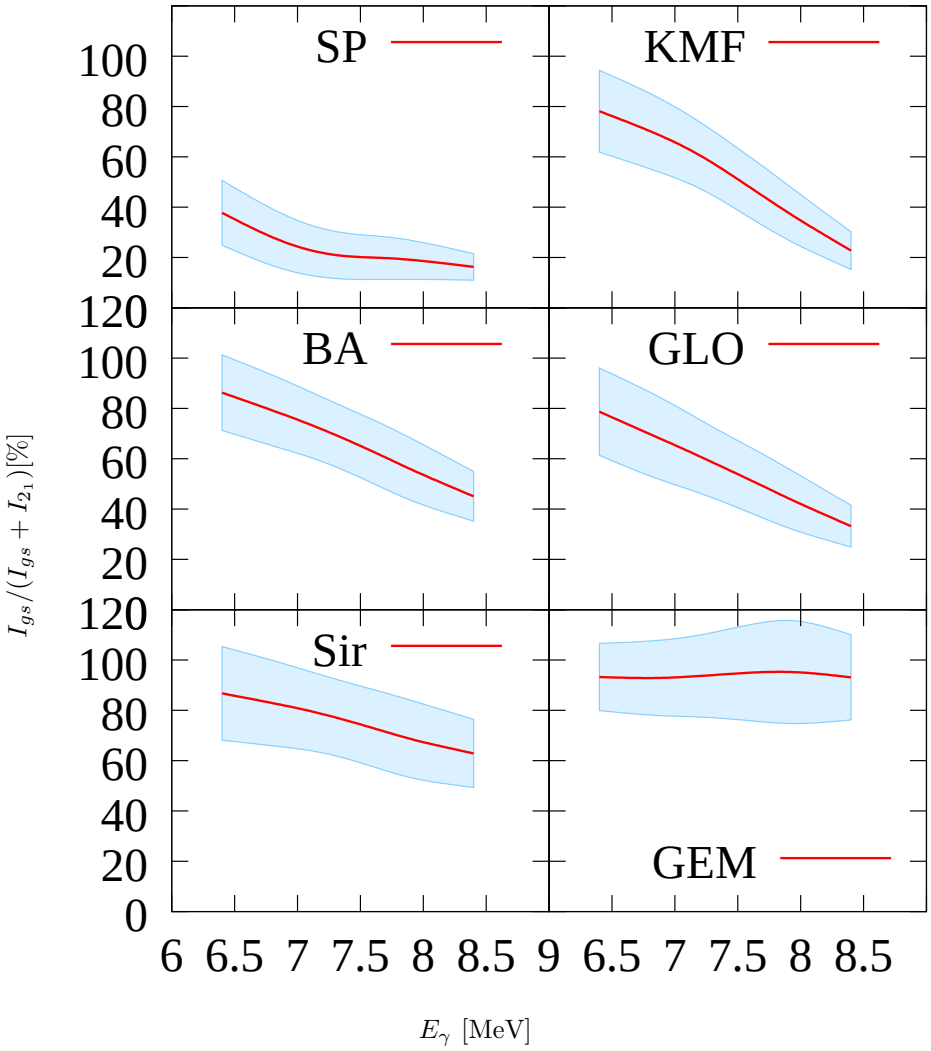

Figure 5.6: Ground-state branching ratio as a function of energy using various models in ^{124}Sn. The red line represents the average ratio from 10,000 simulations. The shaded region represents the spread in ground-state branching ratio obtained in the various nuclear realizations.

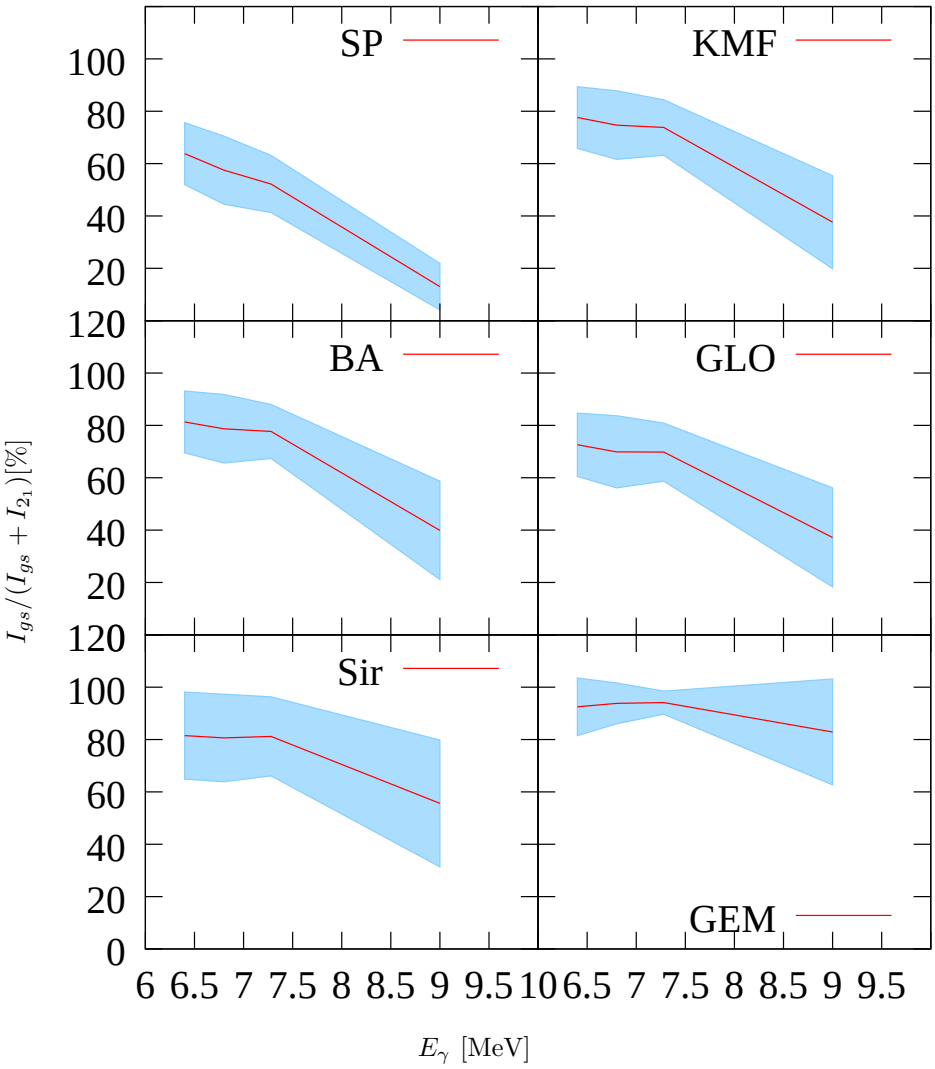

Figure 5.7: Ground-state branching ratio as a function of energy using various models in ^{112}Sn. The shaded region represents the spread in ground-state branching ratio obtained in the various nuclear realizations.

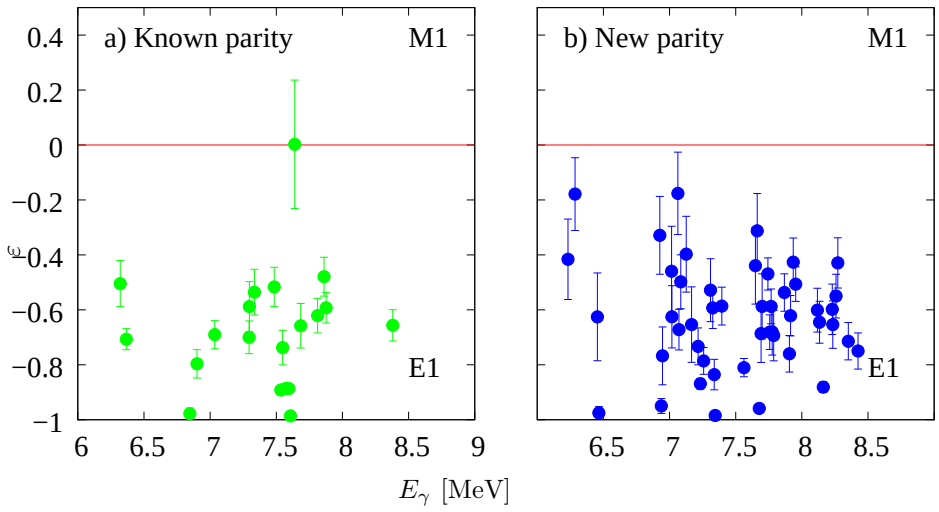

Figure 5.8: Azimuthal asymmetry for observed ground-state transitions in ^{124}Sn. Figure a) shows the states of known parities from reference [Gov98], while Figure b) shows the new parity measurements on previous Gent levels. Most levels have an average asymmetry of -0.8, indicating that they are electric dipole in character.

with energy than was experimental measured. Also shown in Table 5.2 are the summed deviations of the various models from the experimental data. These deviations have been weighted by the average uncertainties of the branching ratios. Examining this summed deviation, the Sir model produced the best agreement with the experimental data.

5.2 Observed Dipole Strength

In total, 106 ground-state transitions were observed in ^{124}Sn, and 13 ground-state transitions were observed in ^{112}Sn. We were able to observe 27 new ground-state transitions in ^{124}Sn and 13 new ground-state transition in ^{112}Sn. The energies, azimuthal asymmetries, decay widths, and ground-state transition strengths for each of these states are reported in Appendix D. Figures 5.8 and 5.9 show the azimuthal asymmetry of the observed ground-state transitions in ^{112}Sn and ^{124}Sn.

Because nuclear resonance fluorescence using Compton backscattered photons is a relatively new method for studying nuclear structure, the procedures for determining the excitation energies and cross sections have not been pursued as throughly as in facilities producing bremsstrahlung beams.

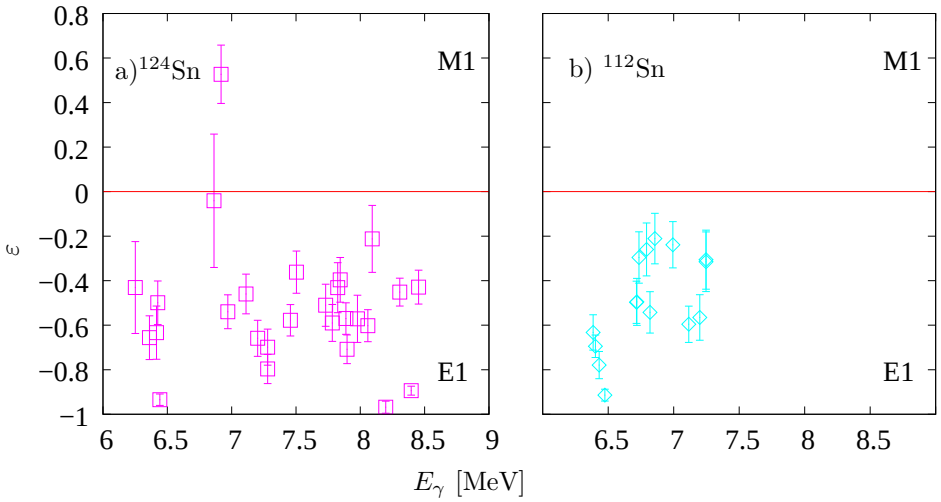

Figure 5.9: Azimuthal asymmetry for new observed ground-state transitions in ^{112,124}Sn. Most of the levels are electric-dipole transitions.

One of the goals of the current experiment is to develop a reliable procedure to extract spectroscopic information from the data. Figure 5.10 shows the discrepancy between the excitation energies determined by the Gent experiment and the present ^{124}Sn measurement normalized to the average standard deviations of the measurements. The vertical scale shows the overlap of the standard deviations of the two measurements. The excitation energies that do not lie within two standard deviations of the Gent data are reported in Table 5.3. Upon further consideration, the disagreements among several of these energies can be explained, and brought into agreement. The discrepancy between the first two levels in the table probably corresponds to the Gent group's averaging over multiple states. Both of these levels are energetically close to new measured resonances, and their average lies within two standard deviations of the Gent data. The third level is energetically close to an escape peak from a standard calibration source used in the Gent experiment. Levels 4 through 13 correspond to energy regions in which the level density is quite high, making the isolation of an individual resonance difficult. In both measurements, the Ge detector had a 5 keV energy resolution at 6 MeV.

Levels 13 through 17 simply do not agree with the Gent data; most of them vary from the Gent data by 2-3 keV. To calibrate the energies, the Gent group used several known standards we did not use. In addition, as discussed above, the Gent method for measuring excitation energies was not without

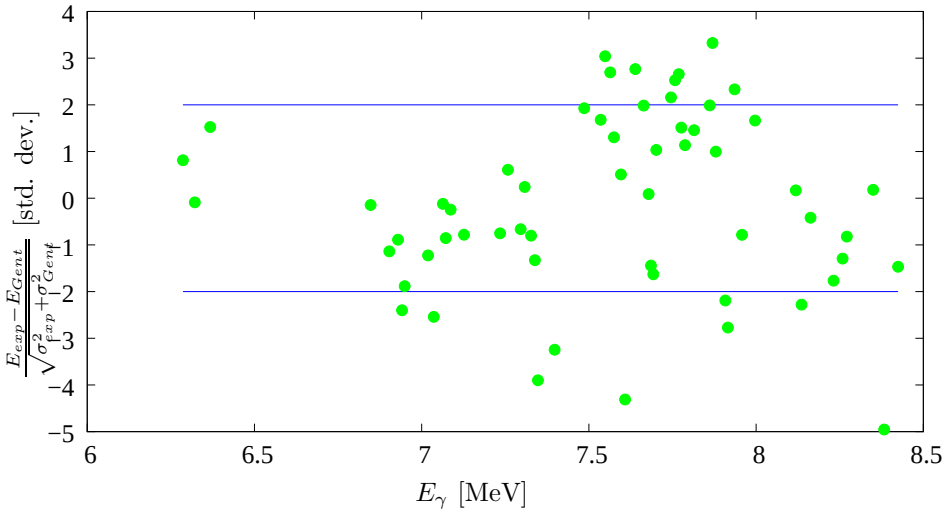

Figure 5.10: Differences between measured excitation energies for ^{124}Sn in the current experiment and those reported by the Gent group.

problems also. In the future, known calibration standards certainly need to be used to calibrate each individual energy measurement.

In addition to measuring the excitation energies, accurate cross-section measurements are also important to any NRF experiment. Figure 5.11 shows the agreement between the integrated cross sections of several levels measured both at HIγS and in Gent. Since the Gent group observed considerable feeding, only levels of assigned parity were used.[5] Most of the levels lie within two standard deviations of the Gent data. The states that lie outside of two standard deviations of the Gent data are reported in Table 5.4. Recall from the energy analysis that some of the states in the Gent data likely corresponded to two levels. In the case of the 7.5 MeV region for example, the level density was very high. The first three transitions listed in Table 5.4 seem to correspond to the effects of multiple levels. The analysis of this summing on individual peaks is given in column four of Table 5.4. As with the comparison of excitation energies, high level density contributes to the discrepancies between the current data and the Gent experiment. Two transitions at 7756 keV and 7596 keV disagree considerably with the Gent measurements. These two states specifically correspond to regions

[5] According to [Gov98], the error in the transition strengths attributed to this problem is about 10% for excitations above 5 MeV.

#	E_{Gent} keV	E_{meas} keV	z	Comments
1	7935.57	7939	2.33	Average of 7945 +7927.71=7939 with z=0.78.
2	7638.61	7642.6	2.77	
3	8382.94	8376.2	4.96	Disagreement is possibly due to an escape peak from 8872 keV (E_{esc}=8361 keV) ^{16}O peak.
	6949.23	6947.5	1.88	The average energy separation for levels in this region
4	6941.19	6938.9	2.40	is 10 keV, coupled with the to the presence of the
5	7563.70	7566.9	2.70	7980-keV escape peak (E_{esc}=6958 keV) in ^{11}B (Gent
6	7548.62	7550.9	3.04	data).
7	7347.71	7344.4	3.90	7-keV energy difference between this peak and the next peak.
8	7768.67	777 0.6	2.66	Average energy spacing in this region is 12 keV. At least two of these states carry considerable strength.
9	7757.56	7759.1	2.53	
10	7745.45	7747.4	2.16	
	7861.47	7863.4	1.98	Average energy spacing in this region is 5 keV. There
11	7869.72	7872.1	3.33	are two double escape peaks from calibration standards
12	7907.90	7905.1	2.19	located in this region from (7850 keV) ^{16}O and from
13	7915.67	7913.1	2.77	(7898 keV) ^{11}B.
14	8135.64	8131.7	2.28	
15	7768.67	7770.6	2.66	
16	7397.46	7394.5	3.24	
17	7036.03	7032.5	2.54	

Table 5.3: Comparison of excitation energies in Gent data to those of the current data. Though the numbered states listed in this table do not lie within two standard deviations of the Gent data, they do not necessarily disagree with each other. Possible explanations for the disagreements are given in column four.

where individual peaks could not be discerned. Summing up the strength of the densely packed states results in agreement between the current data and the Gent data. Finally, the problems attributed to calibration sources in the energy comparison seem to also manifest themselves in the integrated cross sections. The last two transitions listed in Table 5.4 are energetically close to a calibration line.

There was some concern that the γ-ray beam might excite either ^{14}N or ^{16}O present in the air. In total there were seven transitions in ^{14}N and ^{16}O that might be populated by the incident γ-ray beam (see Table E.3 in Appendix E). The degree of peak contamination was calculated by comparing the estimated number of counts attributable to air with the observed number of counts in the peak. Of course, peak here means the total efficiency corrected escape- and full-energy peak (see Equation 4.5). The estimated number of counts due to interaction with the air was calculated using Equation 4.8. The results of these calculations are given in Table 5.5.

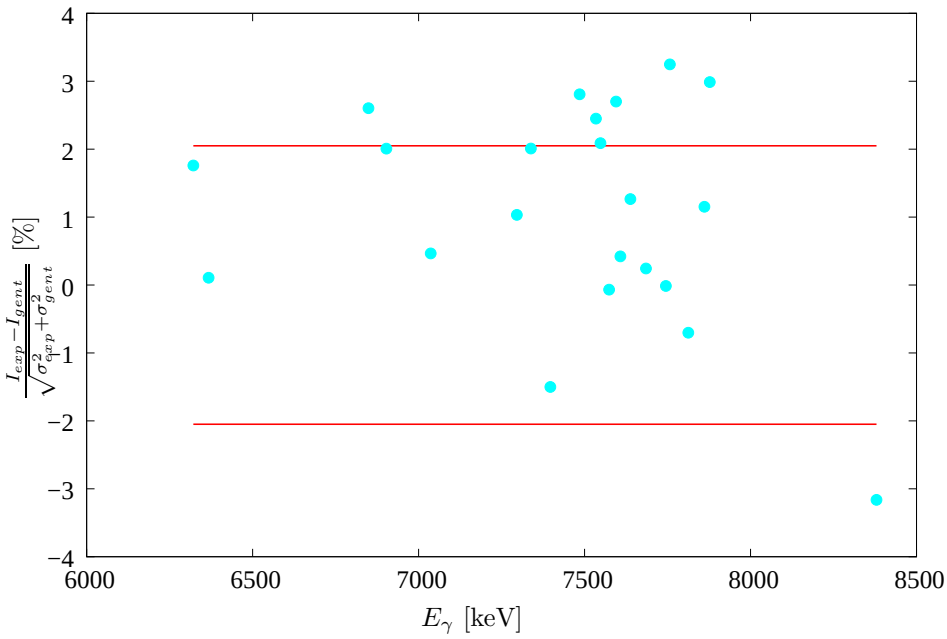

Figure 5.11: Comparison the measured cross sections in the current experiment to those measured by the Gent group. Since the Gent group experienced considerable feeding, only levels of assigned parity were used. Cross sections that do not lie within one standard deviation of the Gent data are given in Table 5.4.

The most likely case of interference is the 8.06-MeV state in ^{14}N, decaying to the ground state 80% of the time and populating the 3.95-MeV state 13% of the time. Both of these transitions have very large radiative widths, on the order of 10 eV for the ground-state transition and 1 eV for the 4113-MeV transition. A ground-state transitions was observed at 8.059 MeV in ^{124}Sn. As shown in Table 5.5, depending on the assumed height of the air, a significant portion of the observed counts in this peak can be attributable to air. Assuming a 300-cm long column of air, 100% of the detected counts would be due to this transition. Although, considering the branching ratio of the 8.06-MeV state and the size of the target, there should be some population of the 3.95-MeV state. Transitions to this state, or from this state to the ground state were not seen in the experimental data, even after removing much of the background through TOF cuts.

There are two additional cases of interference in the ^{124}Sn data, specifically transitions observed at 6.92 and 6.45 MeV. In both cases, multiple targets were used at these energies, and the transitions were seen in only the ^{124}Sn target. In the case of 6.45-MeV transition, the ^{124}Sn target was replaced

E_x keV	I_{exp} eV b	I_{gent} eV b	z	
7535.17	80(5)	133(21)	2.45	Recall that the Gent gent probably saw one states and not two here. The summed integrated cross section of these two states is 134(5) eV b, with z= 0.05.
7485.92	79(6)	130(17)	2.81	Same as above, the summed integrated cross section of these two states is 135(8) eV b, with z= 0.27.
7878.07	104(30)	219(15)	3.26	Sum in strength of 7893 peak: $I_s = 233(18)$ eV b, which corresponds to z= 0.60
7756.89	94(7)	142(13)	3.25	Summing up the strength in this peak with its two closest neighbors gives: $I_{exp} = 369(15)$ eV b and $I_{gent} = 337(23)$ eV b. These two measurements are within 1.17 standard deviations of each other.
7595.85	206(14)	143(13)	2.71	Sum up the strength in the 7603 peak: $I_s = 247(11)$ eV b. Compare this sum with the summation of the corresponding states in the Gent data: $I_s = 296(51)$ eV b. These two cross sections are within 0.93 standard deviations of each other.
8382.94	148(14)	96(6)	3.16	Possible interference from first-escape peak of ^{16}0 transition at 8872 keV.
7547.89	76(5)	111(16)	2.09	This energy region corresponds to the double-escape peak in the ^{11}B transitions at 8560 keV.

Table 5.4: Integrated cross sections that lie outside of two standard deviations from the Gent data.

by a ^{112}Sn target, which did not show any activity at 6.42 MeV. The 6.92-MeV transition will be discussed in more detail in the next section.

5.2.1 Magnetic Transitions

One of the most interesting questions about the present data is the lack of magnetic-dipole strength. The Gent group tentatively assigned two levels to be magnetic-dipole transitions, one at 8.269 MeV and the second at 6.808 MeV. The current experiment did not examine the 6.8-MeV energy range; therefore, nothing can be said about that state. The 8.269-MeV state was observed, and the measured azimuthal asymmetry was ε=-0.429(9), indicating that it is in fact an electric-dipole transition. Two possible magnetic-dipole excitations were observed in this experiment at 6.863 and 6.916 MeV. In the case of both transitions, the high density of E1 transitions made the positive parity assignment difficult. Neighboring negative parity states often overlapped with the energy region of the magnetic states, which decreased the azimuthal asymmetry. The Gent group did not see this level because they

Nucleus	E_x keV	$\frac{A_{air}}{A_{obs}}(h = 100cm)$ [%]	$\frac{A_{air}}{A_{obs}}(h = 1000cm)$ [%]
^{14}N	6446.17	0	0.01
^{14}N	8062.0	33	>100
^{16}O	6917.1	0.097	0.88

Table 5.5: Percentage of total counts that are due to transitions in ^{14}N or ^{16}O. These calculations are performed assuming a one-inch diameter column of air at constant temperature and pressure. The results are shown for a 100-cm long column of air and a 1000-cm long column of air. In the case of the 8.062-MeV state in ^{14}N, the number of counts expected in the peak for a 1000-cm long column of air exceeded the number of observed counts.

used ^{16}O as a calibration standard, which has a 2^+ state at 6.917 MeV. To rule out the presence of ^{16}O in the sample, I looked for the presence of other strong transitions in ^{16}O in the data, specifically the E_x=7.116 MeV state. Peaks were observed at 7.125 and 7.086 MeV, but nothing was seen at 7.116 MeV. In addition, the spectrum obtained from the irradiation of a natural Sn target with the same geometry and mass did not show the strength observed in ^{124}Sn target.

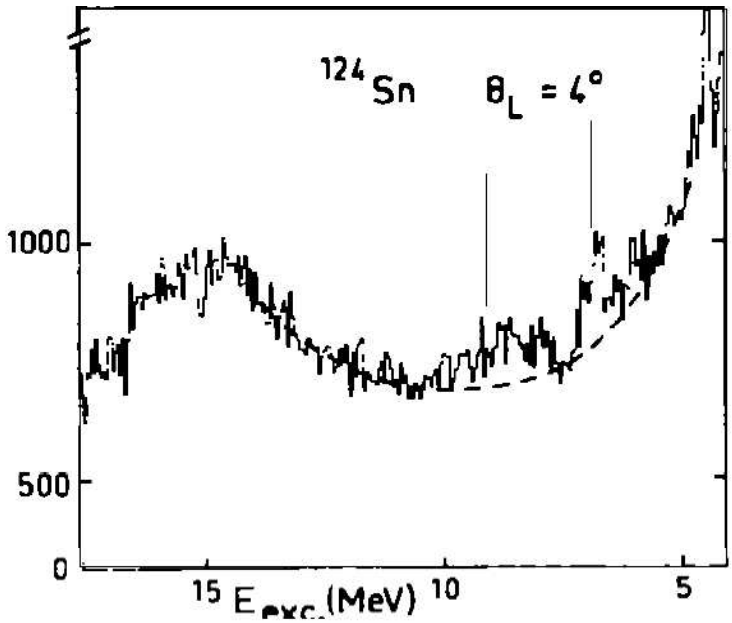

Figure 5.12: Spectrum at 4° from ^{124}Sn (p,p') scattering experiment [Dja82]. The arrows indicate the location of M1 resonances observed in this experiment, one at 8.4 MeV and the second at 6.9 MeV.

Interestingly enough, this is not the first instance in which an M1 state has been detected at this

energy. An experiment in the early 1980's at the Orsay synchrotron measured several M1 transitions in ^{124}Sn, as well as in various other isotopes [Dja82]. In the observed spectra at 4° on ^{124}Sn shown in Figure 5.12, there are clean bumps, one at 8.4 MeV and a second smaller bump at 6.9 MeV. Understanding why these resonances are observed only under certain circumstances would tell us a great deal about the nature of the excitation. Recall from Section 2.1 that the M1 operator is given by

$$\mathcal{M}^M = \frac{e\hbar}{m}\left(\left(\frac{1}{L+1}\mathbf{L}\cdot\nabla(r^l Y_{\ell m}(\theta,\phi))^*\right) + \frac{\mu_N}{2}\sigma\cdot\nabla(r^l Y_{\ell m}(\theta,\phi))^*\right). \tag{5.4}$$

Equation 5.4 has two terms that operate on the wave-function. In the first term, $\mathbf{L}$ transforms the orbital angular momentum of the initial state, while the operator in the second term, σ transforms the spin of the initial state. These operators indicate that, for NRF scattering, the M1 operator comprises two parts, an orbital part and a spin-flip part. If we had used the proton Hamiltonian in Equation 2.8, the $\mathbf{L}$ term in Equation 5.4 would vanish at small angles [Ric91]. The fact that the transition is observed in both (γ,γ') and (p,p') scattering indicates that this transition has both orbital and spin components, a characteristic of a spin-flip excitation. Since the decay width was not reported in the (p,p') experiment, deducing what percentage of this transition is due to the orbital component and what part is due to the spin component is impossible.

The M1 transition at 8.4 MeV is much more interesting. The existence of a state in this energy range has been shown both experimentally through (p,p') excitation and theoretically in RPA calculations (see Figure 5.13) [Ter07b] . What type of structure would be susceptible to excitation via protons but invisible to γ-rays? One suggestion was that this state corresponds to a spin-flip state in $1g_{9/2} \rightarrow 1g_{7/2}(\pi)$, $1g_{9/2} \rightarrow 1g_{7/2}(\nu)$, and $1h_{11/2} \rightarrow 1h_{9/2}(\nu)$ orbits [Gov98]. This state, however, is clearly not seen in the (γ,γ') data. This apparent absence does not necessarily preclude the existence of a spin-flip state; however, it does open up the possibility of other more exotic excitations. A similar situation was observed for the 10.15 MeV M1 state in ^{51}V [Oda87]. One proposed explanation for this state is that the spin and orbital contributions destructively interfere, which would explain why a state

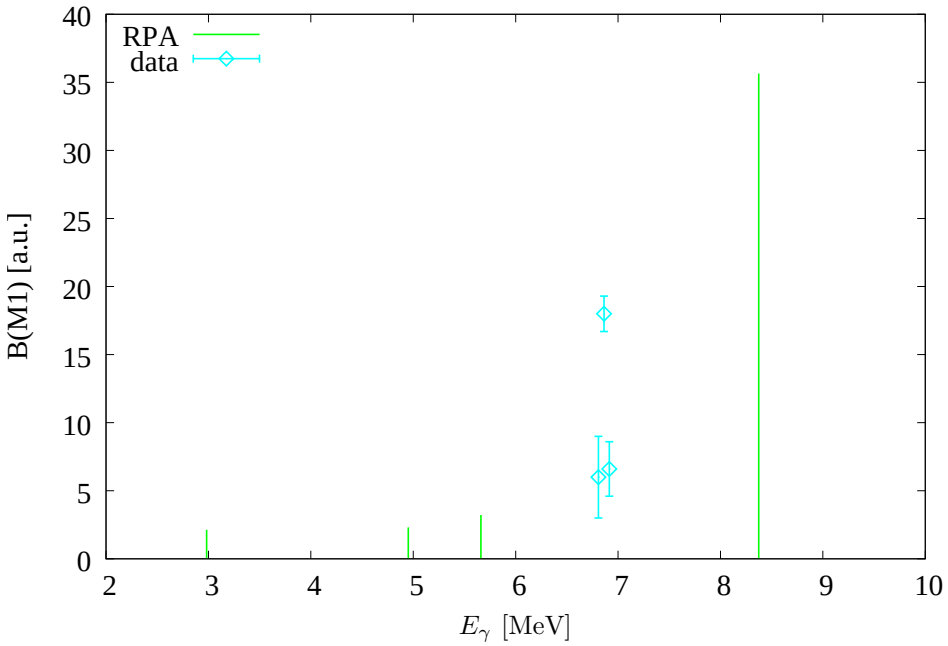

Figure 5.13: RPA calculations for M1 strength distribution on ^{124}Sn [Ter07b]. The calculations predict considerable strength at 8.4 MeV. While being observed in (p,p') scattering, this state is absent in (γ, γ') experiments.

was detected in (p,p') and not (e,e') [Oda87]. Another possible explanation concerns the excitation probabilities for the two probes. Proton scattering is much more sensitive to M1 transitions than γ-rays. In addition, the energy resolution in proton scattering is greater than NRF. All of these factors could lead to a series of fragmented states that are too weak to be detected above the background in (γ, γ') experiments but observable in (p,p') experiments [Oda87].

A third possible explanation for the absence of this transition in both the current data and the Gent data is the energetic location of the strength. The bump in Figure 5.12 is quite wide, extending essentially from the edge of the 6.8-MeV resonance to 10 MeV. The actual M1 strength could possibly be detected at a higher energy than 8.4 MeV. This possibility, however, can be ruled out by simply extending the experimental data up in energy.

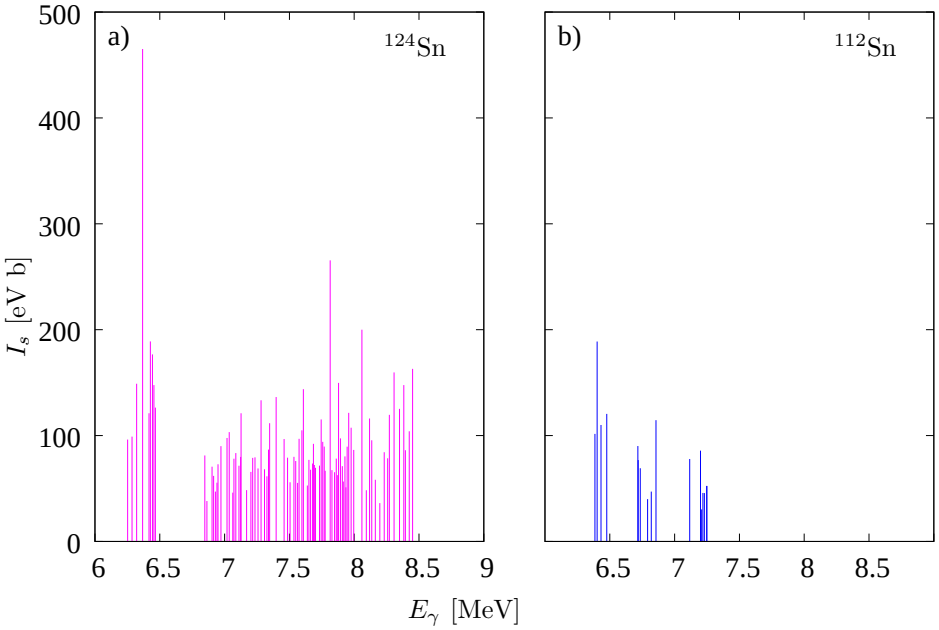

Figure 5.14: Integrated cross sections for Sn. The figure on the left (a) shows the integrated cross sections for ^{124}Sn as a function of excitation energy. The figure on the right (b) shows the integrated cross sections in ^{112}Sn.

5.2.2 Electric Transitions

The majority of the ground-state transitions were electric-dipole transitions, a result that agrees nicely with the Gent data. Figure 5.14 shows the integrated cross sections observed in this experiment. The minimum observed E1 transition at E_x =8197(3) keV had an integrated cross section of 36(7) eV b, while the maximum was at E_x=6367 keV was I_s=465(25) eV b. All of the transitions in the Gent experiment were measured with two exception, the transitions at 8433 keV and 8214 keV.

The elastic photon cross sections were determined by integrating over the background subtracted energy region of the observed transitions (see Figure 3.4). The same procedure was followed for the integrated cross section; however, the total flux was used instead of the flux at a specific E_x. As in the case of the inelastic transitions, the total elastic scattering cross section over an energy region is given by

$$< \sigma_{\gamma\gamma} >= \frac{2J+1}{2J_0+1} \left(\frac{\pi\hbar c}{E_x}\right)^2 \left\langle \frac{\left\langle \frac{\Gamma_0^2}{\Gamma} \right\rangle}{D} \right\rangle . \tag{5.5}$$

The observed strength distributions for ^{112}Sn and ^{124}Sn are shown in Figure 5.14. Due to the lack of available beam time, the full energy range was not investigated for the ^{112}Sn isotope. In the energy region between 6.3 to 7.3 MeV, there was three times more dipole strength in ^{124}Sn ($\sum B(E1) = 226(27) \times 10^{-3}\ e^2fm^{26}$) than in ^{112}Sn ($\sum B(E1) = 74(2) \times 10^{-3}\ e^2fm^2$).[7] This result, of course, is to be expected if one assumes that the nature of these excitations is related to the neutron radius, which increases in ^{124}Sn by a factor of 2.78 from ^{112}Sn [Kra04]. In addition, the summed-energy-weighted dipole strengths in this region are $\sum E_x B(E1) = 0.493(12)$ keV e^2fm^{26} and 1.513(183) keV e^2fm^2 for ^{112}Sn and ^{124}Sn, respectively. These summed-energy-weighted transitions can be related to the classical energy-weighted-sum rule [Har02] by

$$S_{TRK} = \int_0^\infty \sigma_\gamma(E)dE = \frac{2\pi^2e^2\hbar^2}{Mc}\frac{NZ}{A} \tag{5.6}$$

$$= 60\frac{NZ}{A} \quad \text{mb MeV}. \tag{5.7}$$

Or in terms of transition strength (see equation 2.24),

$$S(E1)_{TRK} = \frac{9}{4\pi}\frac{\hbar^2e^2}{2M}\frac{NZ}{A} = 14.8\frac{NZ}{A}\text{MeV } e^2fm^2. \tag{5.8}$$

We find the E1 strength in ^{112}Sn exhausts 0.120(3)%[6] of the EWSR, while 0.34(4)% of the EWSR is exhausted in ^{124}Sn. Furthermore, by dividing the summed-energy weighted strength by the total strength, we can establish an average excitation energy ($< E_x >$) for the observed strength. In this case of ^{112}Sn and ^{124}Sn, the average excitation energy was 6.66(17)[6] and 6.67(10) MeV, respectively.

In the Gent experiment, the summed transition strength in ^{124}Sn was estimated by summing up the individual transition strengths after correcting for an estimated ground-state branching ratio (75%). Assuming that all observed transitions were of E1 character, the Gent group estimated a summed transtion strength of 0.345(43) e^2fm^2 for ^{124}Sn between 5 and 8.5 MeV, which corresponds

[6] Uncertainty calculations are presented in Appendix D.0.3.

[7] Since the current experimental data did not cover the 6.8 MeV energy region, the Gent data were used to supplement this comparison.

to 0.27% of the energy-weighted-sum-rule. In the current experiment, the summed transition strength was calculated using the absorption cross section. In the 6-8.5 MeV energy region, the summed transition strength was 369(10) $\times 10^{-3}$ e^2fm^2, which corresponds to 0.61(2)% of the energy-weighted-sum-rule. Of course, when the branching ratio from the Monte Carlo simulation is used instead of the experimentally observed branching ratio, this strength increases to 638(30) $\times 10^{-3}$ e^2fm^2, or 1.06(5)% of the energy-weighted sum rule.

Considerable enhancement of the strength seems to occur in the 6.4-MeV energy range for both nuclei. In the case of ^{124}Sn, the absorption cross section in this energy range is dominated by a single transition at 6.367 MeV with a transition strength of $18.40 \times 10^{-3} e^2fm^2$, account for 25% of the total strength. In ^{112}Sn, this transition splits into two transitions at an $< E_x >= 6.42$ MeV with a summed transition strength of $15.93 \times 10^{-3} e^2fm^2$, or 20% of the total observed strength. These excitations appear consistently in heavy nuclei near closed shells [Gov98]. Enhanced transition strengths at this energy have also been observed in ^{116}Sn [Gov98], ^{90}Zr [Ala87], ^{89}Y [Rei97], and ^{140}Ce [Her97].

5.3 Total Absorption Strength

Recall from Chapter 1 the questions we set out to answer concerning the PDR: firstly, understanding the nature of the pygmy dipole states and to establish their relationship with the GDR. In section 5.2, we learned that these states are predominantly electric dipole, and that their strength is related to the number of valence neutrons. It is this latter question that we concern ourselves with here. Since most of the strength associated with the GDR is above the particle-emission threshold, we need some way of relating the (γ, n) data to our current (γ, γ) data. According to the compound nucleus hypothesis, the formation and subsequent decay of an excited state are independent processes [Fes92, Bet37, Boh36]. Thus, the probability of absorbing a photon can be related to the elastic-scattering cross section:

$$\sigma_{\gamma\gamma} = \frac{\Gamma_0}{\Gamma}\sigma_\gamma(E). \tag{5.9}$$

^{124}Sn	E_x (keV)	$\sigma_{\gamma\gamma}(2_1 \rightarrow gs)$ (mb)	$\sigma_{\gamma\gamma}(E_x \rightarrow gs)$ (mb)	σ_γ (mb)
	8.4	3.20(15)	5.48(25)	12.60(77)
	8.2	3.06(12)	4.97(17)	11.46(70)
	7.9	2.92(16)	5.25(18)	12.53(269)
	7.7	2.44(14)	6.26(20)	13.15(86)
	7.5	1.81(12)	5.44(18)	11.93(66)
	7.3	1.84(20)	6.37(26)	13.79(84)
	7.2	1.31(13)	4.70(16)	9.66(295)
	7.0	1.44(21)	4.76(22)	9.12(315)
	6.9	1.35(14)	3.68(15)	7.11(91)
	6.4	1.25(27)	11.76(42)	21.39(173)

^{112}Sn	E_x (keV)	$\sigma_{\gamma\gamma}(2_1 \rightarrow gs)$ (mb)	$\sigma_{\gamma\gamma}(E_x \rightarrow gs)$ (mb)	σ_γ (mb)
	7.2	1.55(25)	4.83(25)	6.11(107)
	6.8	1.33(22)	3.87(23)	4.90(89)
	6.4	0.169(3)	5.96(30)	7.45(115)

Table 5.6: Photo-absorption cross section for ^{112}Sn and ^{124}Sn. The photo-absorption cross section is determined by dividing the elastic photon scattering cross section (column 2) by the branching ratio. The branching ratio was determined in Section 5.1. In these calculations, the branching ratio was determined from Sir photon strength function.

Of course there is some concern over whether the compound nucleus theory holds across the particle-emission threshold. Generally, the average lifetime of states from 6 MeV to the particle-emission threshold are slow enough for the statistical theory to be applicable. The total elastic cross sections, the decay widths, and the transition strengths for each energy range are given in Appendix D Table D.3. The total absorption cross sections were determined using branching ratios from the Sir model in the DICEBOX simulation results (see Table 5.6). The photo-absorption cross sections for ^{124}Sn are shown in Figure 5.15 together with (γ, n) data taken at Livermore [Ful69] and at Saclay [Lep71]. These data sets, [Ful69] and [Lep71], will be referred to as the Livermore and Saclay data, respectively. In the case of the Livermore data, 92 photo-absorption cross sections were reported between the energies of 8.5 and 31 MeV [Ful69]. In the Saclay experiment, 46 photo-absorption cross sections were reported between the energies of 9.4 and 2 MeV [Lep71].

Generally, the systematic features of the GDR can be reproduced by approximating its shape with

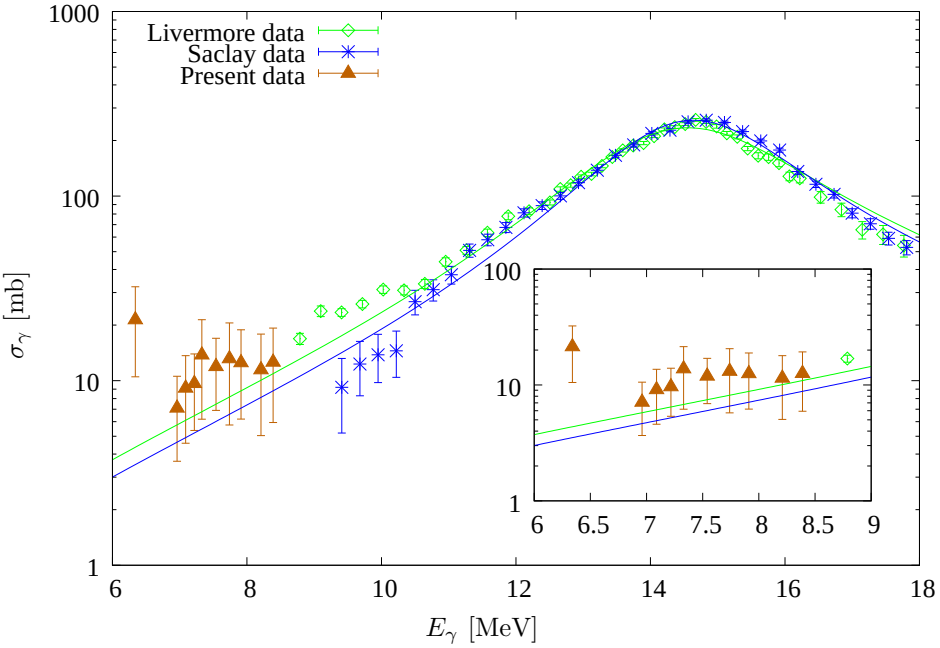

Figure 5.15: Comparison of determined photo-absorption cross section from the present experiment with the measured cross section from (γ, n) experiments [Ful69, Lep71]. The error bars for the (γ, γ) data have been increased to show the range of values predicted by the various γ-ray strength function models (see Section 5.1). The green and blue solid lines are Lorentz fit to the (γ, n) data from [Ful69] and [Lep71], respectively. In the small insert, the data below the particle-emission threshold have been enhanced for easier viewing.

a classical Lorentz line:

$$\sigma_\gamma = \sigma_0 \frac{E_x^2 \Gamma_0^2}{(E_x^2 - E_0^2)^2 + E_x^2 \Gamma_0^2}, \tag{5.10}$$

where E_0 and Γ_0 are the position and half-width of the resonance in MeV, and σ_0 is the maximum cross-section of the resonance in mb. The Lorentzian fits to the Saclay and Livermore data are shown in Figure 5.15. At the neutron emission threshold, the Livermore data display a small enhancement of strength, which is continued below the particle-emission threshold by the current data. In general, comparing the the present data with the (γ, n) data show a smooth connection between the data of the two experiments. In comparison to the GDR extrapolations, there is a 1% enhancement over the Livermore data fit and a 1.98% enhancement above the Saclay data fit.

Just as the parameters of the GDR can be described according to a Lorentzian fit, perhaps the parameters of the PDR can be described in a similar manner. As a test of this theory, the entire

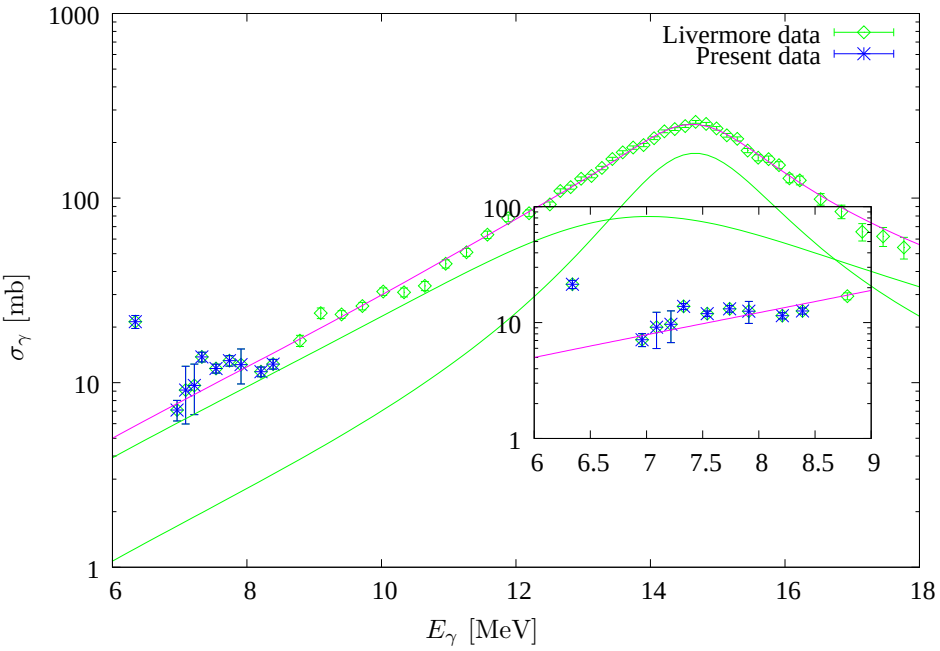

Figure 5.16: Comparison of determined photo-absorption cross section from the present experiment with the measured cross section from the Livermore (γ, n) reaction. These two data sets were fit with two Lorentzian's, one characterizing the GDR and the other the PDR.

energy range was fit with two Lorentzian's:

$$\sigma_\gamma = \sum_{i=1,2} \frac{\sigma_i E_x^2 \Gamma_i^2}{(E_x^2 - E_i^2)^2 + E_x^2 \Gamma_i^2}, \tag{5.11}$$

where σ_i, E_i, Γ_i are all fit parameters (Table 5.7). It is important to make sure that the new two Lorentzian shape continues to describe the GDR, as such, the results of the two Lorentzian fit should be compared to the single Lorentzian fit. In the case of the Livermore data, the double Lorentzian fit put the GDR energy at 14.57(4) MeV, which is considerably lower than the quoted energy, $E_0 = 15.18(4)$ MeV, from the Livermore analysis[Ful69]. This is also the case for the fit to the Saclay data, which estimated the GDR energy at 15.29 MeV, about 1-MeV higher than the 14.64(3) MeV obtained in this fit [Lep71]. Of course both of these data sets have been modified since their original publication to account for experimental errors (see [Var03]). The fit parameters Γ_i and σ_i can be related to the S_{TRK} according to $\frac{\pi}{2}\sigma_i\Gamma_i = 60NZ/A$. In the case of the Livermore data, these fit parameters exhausted

data	E_0 MeV	Γ_0 MeV	σ_0 b	χ^2/ndf
Livermore	14.57(4)	3.80(11)	234(4)	14
	7.38(30)	1.15(93)	5.3(21)	
Saclay	14.64(2)	3.18(9)	259(48)	5
	7.55(17)	1.42(55)	6.98(119)	

Table 5.7: Parameters of the fit to the various GDR data.

78% of the sum rule, while for the fit to Saclay data 72% of the sum rule was exhausted. Turning now to the characterisation of the PDR peak, Equation 5.11 describes the lower energy data very nicely (see Figure 5.16), making it much easier to compare the recent (γ, γ') measurements with the existing (γ, n) data. The fit to Livermore data puts the PDR at a centroid energy of 7.38(31) MeV, while the Saclay data shifts the centroid higher to 7.55(17) MeV. Similarly, the resonance widths were similar for the two fits; Γ_2=1.15 MeV for the fit to Livermore data, and 1.44 MeV for the fit to Saclay data. The slight deviation between the two widths is most likely due to different low-energy behaviour observed in the two experiments.

The area ratio for the two Lorentz lines ($\sigma_1\Gamma_1/\sigma_2\Gamma_2$), was examined for the two fits. In the case of the Livermore data, the area under the GDR fit was 145 times larger than the area under the PDR fit. For the Saclay data, the area under the GDR fit was 83 times larger than the area under the PDR fit. It would be interesting to compare these ratios with other isotopes, specifically ^{112}Sn. Unfortunately, there is no available (γ, n) data for ^{112}Sn, therefore, this type of analysis could not be performed on ^{112}Sn.

It might be informative to compare the fit parameterizations with the PDR properties deduced in the previous section. There we find that for ^{124}Sn, the summed transition strength is 638(30) $\times 10^{-3} e^2 fm^2$, and the energy-weighted-summed-transitions strength was 2.130 MeV $e^2 fm^2$, which exhausts 1.06(5)% of the energy-weighted-sum rule. Comparing this to the results of the Lorentzian fit, the area under the PDR peak is 9.57 MeV b and 15.57 MeV b, or 0.5% and 0.9% of the sum rule for the Livermore and Saclay fit, respectively. The Saclay fit is much closer to agreement with the traditional methods for estimating the exhausted fraction of the sum rule. Turning now to average

Authors	Model	Interaction	Conclusion
Paar *et al.*	RQRPA	NL3+DIS	Several single particle states and a single collective states exhausting 2% of EWSR [Paa03].
Sarchi *et al.*	QRPA+PC	p-h SLIII	Non-collective excitations in Sn [Sar04].
Tsoneva *et al.*	QPM	G-matrix	New mode of excitation that evolve with neutron skin [Tso07].
Terasaki & Engel	QRPA	SkM*	No clear correlation between strength and collectivity in neutron-rich nuclei especially at higher masses [Ter06].
Piekarewicz	MF+RPA	NL3/FSU Gold	Single particle excitation with no real enhancement above GDR [Pie06].

Table 5.8: Summary of theoretical models describing the PDR in Sn.

excitation energy, the calculated average excitation energy was found to be 7.37(48) MeV, which agreed with the results of the Livermore fit.

5.3.1 Theoretical Models

What could possibly be the cause of this observed strength enhancement in ^{124}Sn? There are numerous theoretical models that have set out to answer this very question (see Table 5.8). While the models generally agree that the strength evolves with an increase in neutron radius, they differ regarding the degree of the enhancement and the nature of the excitation producing the enhancement. Two underlying modes of excitation are at issue here: a collective excitation of the excess neutrons and an enhancement of single particle excitations associated with an extended neutron density.

Using the Quasi-particle Random Phase Approximation plus phonon coupling (QRPA-PH), Sarchi *et al.* studied the dipole strength in ^{120,132}Sn and ^{208}Pb [Sar04].[8] In all three nuclei, the observed dipole strength below 8 MeV were characterized by single-particle excitations of the surface neutrons.

A similar results was obtained by Piekarewicz using the relativistic RPA, although he neglects effects of pairing in this calculations [Pie06]. Piekarewicz also observed an increase in transition strength with neutron excess. This increase, however, abruptly changed at ^{120}Sn due to the filling of the

[8]This calculation did not provide any data on ^{124}Sn and ^{112}Sn; therefore, a direct comparison is not possible at this time.

$1h_{11/2}$ shell. Piekarwicz calculations extend up to 25 MeV, thus to distinguish between PDR and GDR related excitation, he established an arbitrary cut-off of 10 MeV. Summing up the energy weighted total strength below 10 MeV, and normalizing it to the total strength in this region, the Piekarwicz model estimates the PDR occurring at an average excitation energy of about 7.93 MeV, considerably lower than the measured average excitation energy, 8.25(32) MeV, in the current experiment.[9] The ratio of PDR to GDR for this model is approximately 2.1% and 5.3% for ^{112}Sn and ^{124}Sn, respectively.[10] In the case of ^{124}Sn, the fraction of strength below 10-MeV was 3.8(1)%, again, this was lower than the theoretical predictions of this model.

While the exact predictions of the Piekarewicz model did not describe the ^{124}Sn data, the implications of the theory are quite interesting. In general, the calculations showed that the strength observed in the 8 MeV range can be entirely attributed to bound state transitions between the $3s^{1/2} \rightarrow [3p^{3/2}, 3p^{1/2}]$ and $2d^{3/2} \rightarrow [3p^{3/2}, 3p^{1/2}]$ shells [Pie06]. The energies of these transitions are shown in comparison with the integrated cross sections.[11] By binning the integrated cross sections, we can easily see two bumps in the data. If these excitations do correspond to single-particle excitations, could these two bumps correspond to the various shells involved? In ^{124}Sn, the highest closed shell is the $2d_{3/2}$ shell with four neutrons in the $1h_{11/2}$ shell. The protons completely fill the $2d_{5/2}$ shell. The energy gap between the $2d_{3/2}$ shell to the $3p_{3/2}$ and $3p_{1/2}$ shells corresponds to 6.36 MeV and 7.76 MeV, respectively. While the energy gap between the $3s_{1/2}$ shell and the $3p_{3/2}$ and $3p_{1/2}$ shells corresponds to 6.63 MeV and 8.03 MeV, respectively. The energies of these transitions are shown together with the measured cross section in Figure 5.17. The energies attributed to the various shells are determined by analyzing the single-nucleon transfer reactions [Cor00].[12] There are several strong transitions located very close to the energies of the single-particle transitions. In fact, the

[9] This model made the arbitrary distinction of using 5-10 MeV as the energy region for the PDR. As such, the Livermore data [Ful69] was used to cover the energy range assumed in this model. Since we are using photo-absorption cross sections, the effects of the decay channel have been removed. Essentially, we are only dealing with the probability that a photon is absorbed by the nucleus at a certain energy.

[10] Again, since Piekarewicz cutoff the PDR at 10 MeV, we are essentially looking at the ratio of the total strength below 10 MeV to the total strength between 10 and 25 MeV.

[11] The energies of the transitions are determined from the energy difference of the two shells. These energies do not take into account quasiparticle contributions, which will cause these energies to shift a bit.

[12] The exact energy of the $1h_{11/2}$ shell and the $2d_{5/2}$ shell is not exactly known. Two different measurements have yielded two different results.

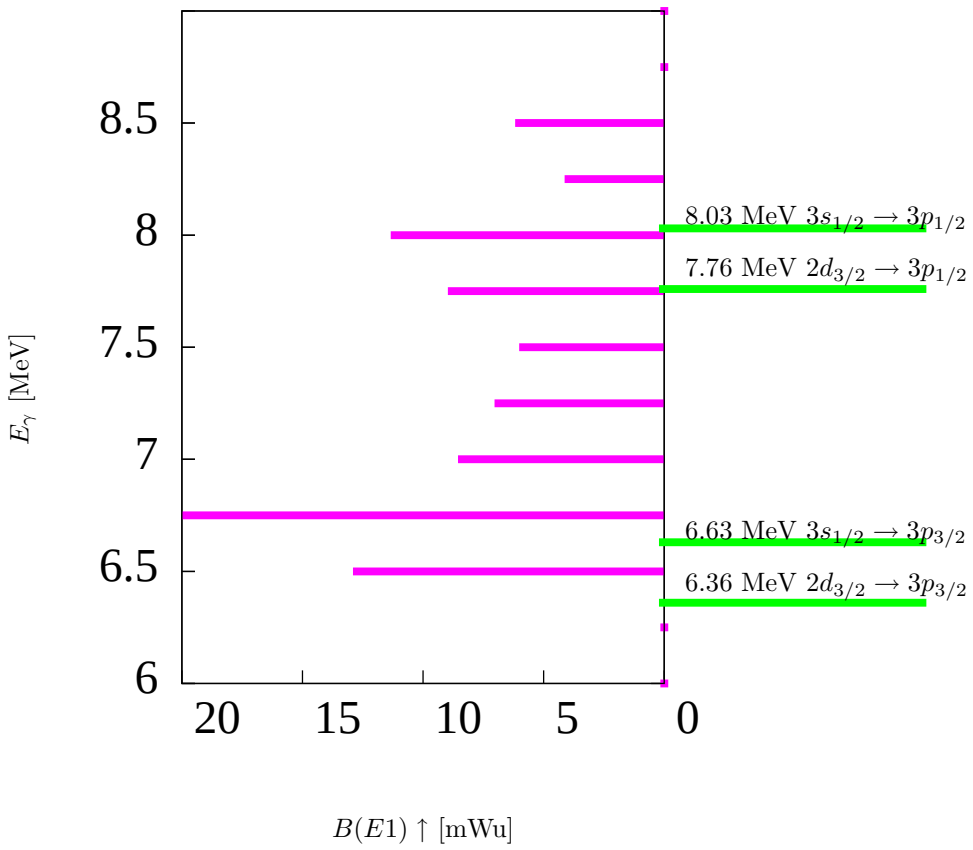

Figure 5.17: The integrated cross sections in ^{124}Sn are compared with single-particle levels in ^{124}Sn [Cor00]. The integrated cross sections have been binned to ease in the comparison. The green (horizontal) lines show the location of the possible transitions across a shell closure [Cor00]. Since this experiment did not cover the 6.8 MeV energy range, the Gent data has been used to fill in this gap.

six strongest transitions strength were all measured very close to the energies of these single-particle transitions, and their sum accounts for 23.6% of the total observed transition strength.

If some, or perhaps even all of these transitions are in fact single-particle transitions, how does one account for their enhanced strength? A total of 26 transitions (22 in ^{124}Sn and 4 in ^{112}Sn) have a transition strength in excess of one mWu. As stated earlier, most of these transitions occur close to where single-particle excitations should be located. Using the formalism of the HFB+RPA approach, J. Terasaki and J. Engel examined this issue assuming a Skyrme SkM* interaction [Ter06, Ter07a]. Their calculations showed that these enhanced transitions were in-fact due to large noncollective transitions to very spatially extended single-particle states [Ter07a]. Figure 5.18 shows the transition strengths

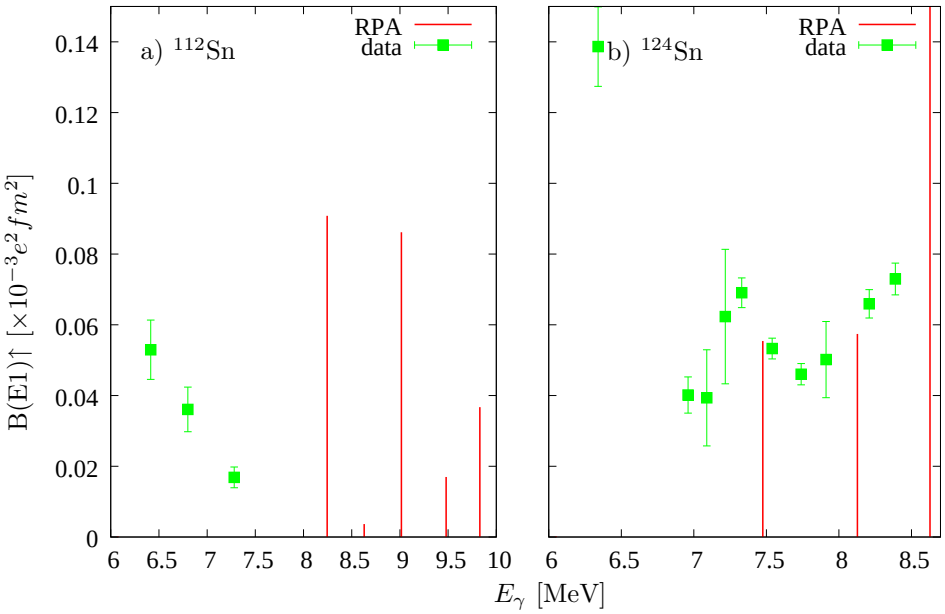

Figure 5.18: Observed and estimated E1 strength in ^{124}Sn. The figure a(b) shows the Strength distribution from RPA calculations in ^{112}Sn (^{124}Sn)[Ter07b].

for ^{124}Sn and ^{112}Sn from their calculations as well as the measured transition strengths. In ^{112}Sn, this model puts most of the transition strength outside of the measured energy region, suggesting that the PDR in ^{112}Sn is shifted up in energy as compared with ^{124}Sn. Turning to ^{124}Sn, the energy region covered in this experiment corresponds to regions of expected strength. The contributions of the various quasi-particle configurations below 8.5 MeV in ^{124}Sn are given in Table 5.9 [Ter07b]. At first glance, the transitions at 8.2 MeV seems slightly larger than the theoretical prediction, however, the 8.2-MeV beam energy overlapped with some of the higher energy transitions in the 7.9 MeV energy range. Despite this slight enhancement, both of the predicted transitions strength agree with the experimental data, it is the lower energy region that is of concern here. According to this theoretical model, a single transition contributes a majority of the strength. Is this missing low energy strength an indication of the contributions from other p-h configurations not listed in Table 5.9?

Several RPA calculations have predicted some strength enhancement associated with collectivity in the neutron skin. Using the formalism of RMF+RRPA, Paar *et al.* predicted several single-particle states and a single collective state at 8.5 MeV that exhausted $\approx 3.3\%$ of the EWSR in the 7-9 MeV

7.4754	particle	shell	%
	ν	$1g_{7/2} \rightarrow 2f_{7/2}$	80.0
	π	$1h_{11/2} \rightarrow 1g_{9/2}$	3.50
	ν	$1i_{13/2} \rightarrow 1h_{11/2}$	2.70
	ν	$2f_{7/2} \rightarrow 2d_{5/2}$	2.20
	ν	$1h_{11/2} \rightarrow 1g_{9/2}$	2.00

8.127	particle	shell	%
	ν	$2d_{3/2} \rightarrow 3p_{1/2}$	64.90
	ν	$2f_{7/2} \rightarrow 1d_{5/2}$	8.80
	ν	$3p_{3/2} \rightarrow 3s_{1/2}$	7.10
	π	$2d_{3/2} \rightarrow 3p_{1/2}$	7.00
	π	$2p_{1/2} \rightarrow 3s_{1/2}$	5.50

Table 5.9: Two quasi-particle components to the QRPA wavefunctions at 7.475 and 8.127 MeV in ^{124}Sn. The first column indicates the type of particle involved in the transition, the second column indicates the shells involved, while the third column show the differences between the squared RPA forward and backward amplitudes [Ter07b].

range [Paa03]. The transition strength seems to increase until A=124, above which the shell effects and pairing correlations reduce the effects of the added neutrons [Paa03]. In a later paper, Paar *et al.* did predict that the peak energies of the PDR for $A \leq 124$ would be located above the neutron seperation energy, thus hindering their observation in (γ, γ') measurements [Paa05]. Using our photo-absorption cross sections, along with the Livermore data below 10-MeV, the average excitation energy is 8.23(13) MeV, very close to the Paar model prediction of 8.7(2) MeV. The predicted transitions strengths for various Sn isotopes are shown in Figure 5.19. The Paar model predicts that 3.3% of the TRK sum rule is exhausted below 10 MeV which agrees nicely with the experiment data. As discussed earlier, combining the current results with the (γ, n) data, 3.82(6)% of the total strength is located below 10 MeV.

In calculations involving the Quasi-particle Phonon Model (QPM), the transition strengths below the particle-emission threshold can be directly related to the neutron skin thickness [Tso07]. Here, below the particle emission threshold, the transition exhibit a strong isoscalar character, thus distinctively separating it from the strongly isovector low-energy tail of the GDR [Tso04]. In a detailed examination of the E1 strength distribution, this model attributes most of the strength to one-phonon

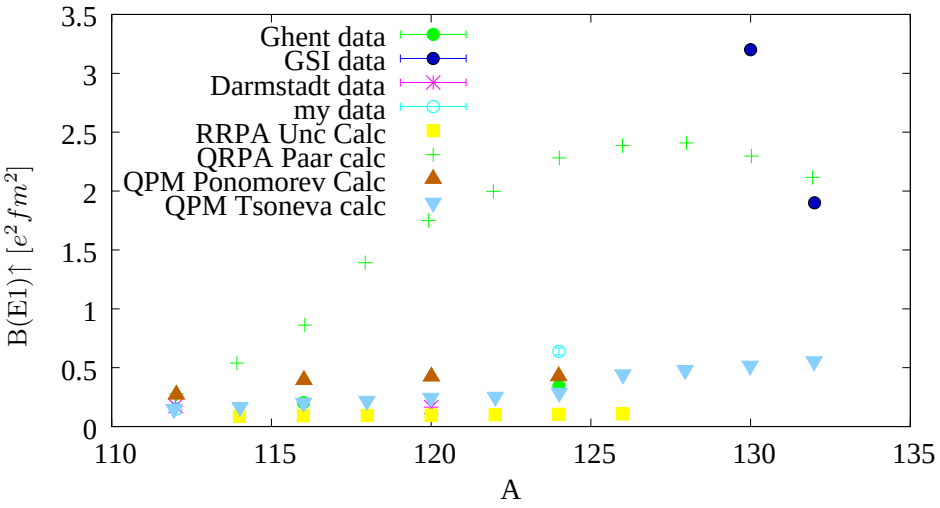

Figure 5.19: Comparison of theoretical models with observed transition strength in Sn. This plot shows all of the experimental and theoretical information available on Sn. Figure 5.20 shows a closer view of the experimental data from this experiment.

$[1_2^-]$ or $[1_3^-]$ components.[13] This model predicted a summed transition strength of 0.398 e^2fm^2 at an average excitation energy of 6.641 MeV. In comparison to the current investigation, the predicted values are considerably lower than the summed transitions strength, 0.549(20) e^2fm^2 at an average excitation energy of 7.70 MeV.

What then, does the QPM model say about the collectivity below the particle-emission threshold? The authors of the various papers are quite cryptic about the nature of this excitation. They often refer to it as a "new excitation", and they discuss the various phonons that contribute to the excitation. In the QPM, the term *phonon* is ambiguous because both collective and non-collective phonons are used in the calculations [Sol92]. Thus, saying that the region below the particle-emission threshold is characterized by one-phonon transitions does not say anything about the degree of collectivity involved. In a recent paper, however, Tsoneva briefly discusses the issue of collectivity [Tso07]. The degree of collectivity is strongly dependent on the spin-orbit potential used in the calculations. In the case of QPM, the spin-orbit potentials that produced collective excitations did not describe the

[13] $[1_2^-]$ and $[1_3^-]$are the second and third 1^- states. The excitation energies associated with these states are not clear. There is only one known 1^- state in ^{124}Sn at E_x=3490 keV. In this model, that state is assigned the notation of $[1_1^-]$

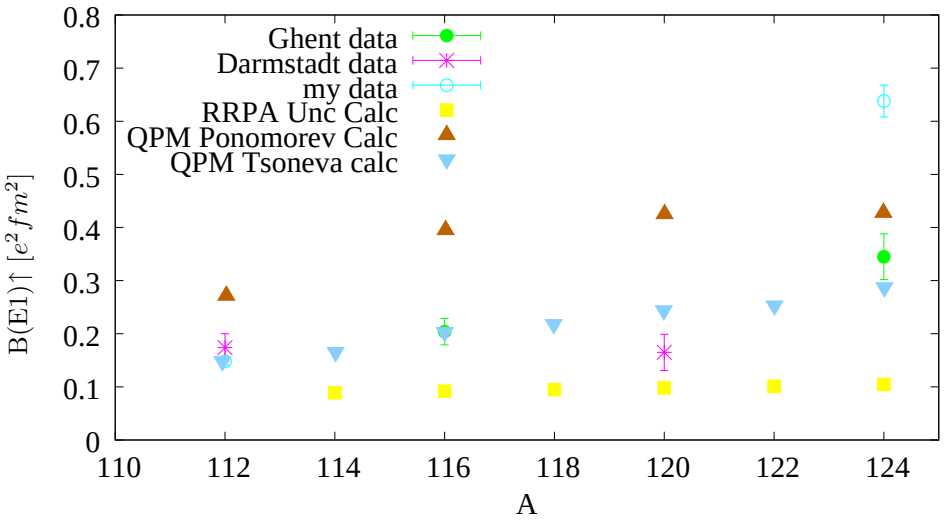

Figure 5.20: Comparison of theoretical models with observed transition strength in Sn.

spectra; thus, these potentials were not used. So the QPM seems to predict enhanced single-particle excitations below the particle-emission threshold.

In summary, while most of the theoretical models predict a strength enhancement that is strongly related to the valence neutrons, how these neutrons generate this enhanced strength is a topic of much discussion. Most of the microscopic theories agree that the transition strength below the particle-emission threshold is predominantly single-particle. Some speculation persists, however, about the occurrence of any collective excitations. Of the theoretical calculations included in this analysis, the Paar model agrees the best with both the average excitation energy and summed transition strength measured in this experiment. This model predicts enhanced strength due to collective motion at 8.5 MeV, which is beyond the scope of the current investigation. In conclusion, the excitations observed in the current experiment are due to single particle excitations to spatially extended neutron orbitals.

6 Summary and Conclusion

To conclude this thesis, it is instructive to first reconsider the research questions originally posed, and whether they have been convincingly addressed.

- What is the spin and parity of the states associated with the pygmy dipole resonance?
- Is there a concentration of strength associated with a collective oscillation of the valence neutrons in the nucleus?
- How does this concentration of strength compare with the giant dipole resonance?

These issues were investigated by using the nuclear resonance fluorescence technique to determine the excitation energies, spins, parities, branching ratios, and the reduced excitation probabilities for E1, M1, and E2 transitions for E_γ = 6.2 - 8.4 MeV in ^{124}Sn and E_γ = 6.2 - 9.0 MeV in ^{112}Sn. The nature of these states are predominantly electric dipole in both nuclei, absorbing 0.52(2)% and 0.39(4)% of the energy-weighted-sum rule in ^{124}Sn and ^{112}Sn, respectively. The cummulative strength of these transitions does show an isotonic dependence, but below the particle-emission threshold, this strength enhancement is attributable to single-particle excitations.

Before proceeding too far in the analysis of the Sn data, I should discuss the accuracy of cross-section measurements at the FEL. Since this is the first time cross-section measurements have been preformed at the FEL, a method was developed in this thesis to determine the flux of the incident Compton-scattered γ-ray beam. The procedure was tested using a well known transition in ^{11}B, as well as several integrated cross sections from the Gent measurement [Gov98]. In the case of ^{11}B, the

measured cross sections were in agreement with reference [Ajz90]. The comparison with the Gent group was a little more involved due to effects of level feeding, to minimize these effects only levels of assigned parity were used. In comparing the 22 known parities, 7 of the measured integrated cross sections were more than two standard deviations from the Gent data. Most of these deviations were attributed to newly measured levels or to interference from calibration standards used by the Gent group.

The excitation energy measurements were also compared with the Gent experiment. In this case, all 60 energies from the Gent group were used in the analysis. A total of 17 measured excitation energies differed by more than two standard deviations from the Gent data. Again, most of these deviations were attributed to the addition of new levels or interference with calibration standards by the Gent group. Five discrepancies could not be explained.

Turning now to the subject of the Sn isotopes, 106 ground-state transitions were observed in ^{124}Sn, and 13 ground-state transition were observed in ^{112}Sn. Using the observed angular distribution of the γ-rays, we confirmed 22 parity assignments and assigned 57 new parities in ^{124}Sn. We also observed 27 new levels in ^{124}Sn, and 13 new levels in ^{112}Sn. The azimuthal asymmetry measurements for ^{112}Sn and ^{124}Sn revealed that 99.98% of the transitions in this energy region were electric dipole. The remaining strength was attributed to two tentative M1 transitions observed in ^{124}Sn. These states did not exhibit strongly asymmetric angular distribution, and were tentatively assigned to be M1+E2 transitions. The M1 strength in the Gent experiment observed at 8.269 MeV was found to be an E1 transition. A second M1 state was observed in the Gent experiment at 6.808 MeV, though this energy region was not covered in the current experiment. Assuming that this state does exist, the summed M1 strength in ^{124}Sn was determined to be 0.67 μ_N^2. Interestingly enough, a state observed in elastic proton scattering at 8.5 MeV was not observed in this experiment. Further investigation is needed to understand the nature of this state. There were no M1 transitions found in ^{112}Sn.

One of the goals of this experiment was to compare the transitions strengths in ^{124}Sn to ^{112}Sn. Unfortunately, a lack of available beam time prevented us from measuring the same large energy range

in ^{112}Sn that was measured in ^{124}Sn. There was, however, some overlapping energy regions between the two measurements. Here, we were able to show an enhanced cumulative transitions strengths in ^{124}Sn compared with those measured in ^{112}Sn. Specifically, in the energy region between 6.3 and 7.3 MeV, ^{124}Sn had three times the cumulative dipole transition strength ($\sum BE1 = 226(27) \times 10^{-3} e^2 fm^2$) of ^{112}Sn ($\sum BE1 = 74(2) \times 10^{-3} e^2 fm^2$). This enhancement is probably related to the larger neutron radius in ^{124}Sn, which is 2.78 times larger than in ^{112}Sn [Kra04].

The examination of the entire energy range covered for ^{124}Sn (6-8.5 MeV) showed the summed transitions strength to be $638(30) \times 10^{-3}\ e^2 fm^2$. To determine the magnitude of the strength enhancement, these data were compared with photoabsorption cross section in the region of the GDR or (γ, n) data [Ful69, Lep71]. This comparison was done using a two-Lorentzian fit; one on the GDR and a second Lorentzian in the region of the PDR. The fit to the Livermore data put the PDR at a centroid energy of 7.38(6) MeV with a width of 1.15(94) MeV, while the Saclay data shifted the centroid higher to 7.55(17) MeV with a width of 1.42(55) MeV. In the case of the fit to the the Livermore data, the ratio of the PDR peak to the GDR peak was about 0.69(63)%, this increased to 1.20(51)% in the case of the Saclay data. Unfortunately, there is no available (γ, n) data for ^{112}Sn, therefore, this type of analysis could not be performed on ^{112}Sn.

One surprising finding in both nuclei was that a small number of transitions contribute most of the strength. In the case of ^{124}Sn, the absorption cross section was dominated by 30% of the observed ground-state transitions, having a summed transition strength of $210(13) \times 10^{-3} e^2 fm^2$, or more than 50% of the total strength. In ^{112}Sn, there were two transitions observed at $< E_x >= 6.403$ MeV with a summed strength of $15.93(3) \times 10^{-3} e^2 fm^2$, or 20% of the total strength. In the case of ^{124}Sn, the energies of many of these states corresponded with single-particle transitions. These enhanced single-particle transitions are believed to result from the extended neutron radius in these elements [Ter07a].

While it seems clear that a majority of the low-energy strength is characterized by single-particle excitations, there is some debate about the contributions of collectivity at the higher-energies, around

the neutron-emission threshold [Paa03]. The problem with resolving this issue is that single-particle excitations, and low-energy GDR excitations also make contributions in this region. In order to determine the collectivity of the PDR, these other excitation mechanisms need to be identified. Currently, all of these modes are excited by γ-rays. Recently, however, an inelastic alpha scattering experiment on ^{140}Ce presented a means by which these different mechanisms might be examined [Sav06]. While the results of the KVI experiment agreed with previous NRF measurements below 6 MeV, above 6 MeV, the alpha particles very weakly excited some transitions, perhaps not exciting them at all. Significant strength was observed above 6 MeV in NRF experiments. The KVI group attributed this disparity to the different excitation mechanisms of the two probes. The α-nucleon interaction is purely isoscalar, while the electromagnetic dipole interaction is both isovector and isoscalar (although the isovector component is much stronger). The two probes also differ in their interactions with the nucleus; photons interact with the entire nucleus, while α particles interact mainly with the nuclear surface [Sav06].

Future measurements using γ-ray beams will help to provide more information on the isotonic dependence of the transitions strengths. In addition, by continuing to parameterize the PDR in terms of a double Lorentzian fit, we might be able to ascribe some neutron radius dependence to this resonance. Turning to the nature of the excitation, γ-rays will probably not be able to provide further information. There are just too many different types of excitation mechanisms below the neutron emission threshold. Inelastic alpha scattering experiments are the most promising means to determining the degree of collectivity associated with the PDR. The hope, is that in the future, through α and γ-ray beams, we will be able to define the nature and strength of the pygmy dipole resonances.

A FEL Beam Characteristics

A Monte Carlo simulation (Geant4) was used to reproduce the beam energy measurement spectrum. An asymmetric Voigt distribution was used as the initial beam profile,

$$GL(x,\sigma,\mu,m) = \frac{e^{\left(-4\ln 2(1-m)\frac{(x-\mu)^2}{\sigma^2}\right)}}{1+4m\frac{(x-\mu)^2}{\sigma^2}}, \tag{A.1}$$

where σ is the full-width-at-half-maximum, and μ is the location of the centroid. The Voigt distribution is simply a Gaussian/Lorentzian distribution; an adjustable parameter m controls whether the peak is a Gaussian (m=0) or Lorentzian (m=1). This line shape is used because of the nature of the FEL beam. The maximum energy γ-ray generated during the Compton scattering process occurs at an angle of $\theta = 0°$. The lower energy γ-rays are scattered at an angle $theta > 0$, and are limited by the finite opening of the collimator. The resulting γ-ray energy distribution exhibits a sharp drop at the higher energies (customary of a Poisson distribution) and an exponential tailing at the lower energies. In order to take into account this effect, Equation A.1 has to be modified to account for this low-energy tailing:

$$A(x,a,\sigma_{1,2},\mu) = \begin{cases} GL(x,\sigma_2,\mu,m) + b(a)\left(e^{-\left(\frac{2\sqrt{\ln 2}(x-\mu)}{\sigma_2 - a2\sqrt{\ln 2}(x-\mu)}\right)^2} - e^{-\left(\frac{(x-\mu)}{\sigma_2}\right)^2}\right) & x \le \mu, \\ GL(x,\sigma_1,\mu,m) & x > \mu. \end{cases} \tag{A.2}$$

where b(a) $=\left(0.7 + \frac{0.3}{a+0.01}\right)$. The parameters for the various incident γ-ray beams are given in Table A.1, while the total incident fluxes of these γ-ray beams are given in Table A.2.

E_γ MeV	σ_1 keV	σ_2 keV	a	m
6.387	65	65	0.34	0.1
6.800	60	60	0.3	0.1
6.960	45	45	0.23	0.1
7.080	70	70	0.35	0.3
7.233	40	50	0.2	0.9
7.25	50	65	0.5	0.1
7.345	47	55	0.3	0.1
7.550	45	55	0.23	0.2
7.766	65	70	0.25	0.5
7.925	50	100	0.27	0.2
8.227	50	60	0.14	0.9
8.420	60	90	0.12	0.5
8.590	50	67	0.19	0.1
9.050	70	70	0.2	0.3

Table A.1: Beam parameters for the incident γ-ray beams.

E_γ (MeV)	Ψ $x10^9\gamma$'s
6.387	14.39(7) + 35.01(17)
6.800	29.54(13)
6.960	38.55(16)
7.080	15.1(6)
7.233	48.8(20)
7.28	25.56(67)
7.345	16.9(7)
7.550	52.11(20)
7.766	39.07(15)
7.925	35.83(14)
8.227	49.00(18)
8.4	75.62(35)
9.050	70.89(166)

Table A.2: Total fluxes for the various incident γ-ray beams.

B NRF Calibration Standards

E_x keV	I_s %
846.771	99.94(3)
1037.840(6)	14.17(13)
1175.102(6)	2.288(21)
1238.282(7)	66.9(6)
1360.215(2)	4.29(4)
1771.351(16)	15.47(14)
2015.181(16)	3.04(5)
2034.755(13)	7.89(13)
2598.459(13)	17.3(3)
3009.596(7)	1.16(3)
3201.962(16)	3.32(7)
3253.416(15)	8.12(17)
3272.990(15)	1.93(4)
3451.152(17)	0.972(20)

Table B.1: ^{56}Co transitions used in simulations and efficiency measurements.

E_x keV	I_s %
1173.288(3)	99.85(3)
1332.492(4)	99.9826(6)

Table B.2: ^{60}Co transitions used in simulations and efficiency measurements.

Source	ID	Calibration	Strength
		Date	$[\mu Ci]$
$^{5}6Co$	10D	12/1/03	0.5270
	89G	1/15/2002	9.409
^{60}Co	2D	3/85	1.193
	89	1/15/02	0.9672
^{88}Y		11/1/03	1.060

Table B.3: Calibration sources used for efficiency measurements.

Nucleus	Abundance %	Mass g	Radius cm	Height cm
^{11}B	99	20	1.27	6.35
^{112}Sn	99	4	0.5	1.6
^{124}Sn	73	46.62	0.795	3.06

Table B.4: Characteristic of targets used in NRF experiment.

C Gent Data

Table C.1: Properties of observed levels in Gent experiment

E_x (keV)	J^π	I_s (eV b)	Γ_0 (meV)	$B(\pi l) \uparrow$ ($\times 10^{-3} e^2 fm^2$)
8433.20(100)	1^-	69(9)	424(53)	
8422.80(70)	1^-	80(8)	495(51)	
8376.20(110)	1^-	96(8)	586(51)	2.9(2)
8350.10(130)	1^-	52(7)	316(42)	
8269.80(70)	$1^{(+)}$	95(8)	564(45)	0.3(2)[1]
8256.90(90)	1^-	54(7)	319(40)	
8228.90(60)	1^-	108(12)	632(72)	
8214.30(120)	1^-	50(11)	291(63)	
8162.20(80)	1^-	67(9)	390(54)	
8131.70(150)	1^-	125(12)	716(67)	
8118.80(80)	1^-	145(11)	827(65)	
8111.80(160)	1^-	66(10)	375(56)	
7998.90(90)	1^-	91(12)	506(68)	2.8(4)
7957.10(90)	1^-	156(10)	857(56)	
7939.00(120)	1^-	52(8)	282(46)	
7913.10(80)	1^-	81(16)	442(89)	
7905.10(120)	1^-	54(12)	294(62)	

continued on next page

[1] M1+E2 Transition in μ_N^2

Observed levels in Gent Experiment (continued)

E_x (keV)	J^π	I_s (eV b)	Γ_0 (meV)	$B(\sigma l) \uparrow$ ($\times 10^{-3} e^2 fm^2$)
7880.20(50)	1^-	219(15)	1181(80)	6.9(5)
7872.10(60)	1^-	108(17)	582(89)	
7863.40(80)	1^-	94(12)	506(64)	3.0(4)
7815.30(50)	1^-	249(18)	1321(95)	7.6(6)
7788.30(50)	1^-	111(13)	582(66)	
7778.10(90)	1^-	56(12)	294(63)	
7770.60(60)	1^-	80(15)	420(79)	
7759.10(40)	1^-	142(13)	741(68)	4.5(4)
7747.40(70)	1^-	115(12)	598(63)	3.7(4)
7702.60(90)	1^-	41(10)	212(50)	
7691.20(70)	1^-	83(14)	424(72)	
7683.90(110)	1^-	97(18)	496(91)	3.1(6)
7678.80(140)	1^-	54(11)	274(58)	
7666.00(70)	1^-	47(8)	241(41)	
7642.60(80)	1^-	74(14)	374(73)	2.4(5)
7603.70(80)	1^-	153(21)	768(104)	5.0(7)
7596.40(100)	1^-	143(13)	716(66)	4.7(4)
7575.90(70)	1^-	96(12)	476(60)	3.1(4)
7566.90(100)	1^-	69(9)	342(45)	
7550.90(60)	1^-	111(16)	548(81)	3.6(5)
7536.50(70)	1^-	133(21)	655(104)	4.4(7)
7487.60(70)	1^-	130(17)	633(82)	4.3(6)

continued on next page

Observed levels in Gent Experiment (continued)

E_x (keV)	J^π	I_s (eV b)	Γ_0 (meV)	$B(\sigma l)\uparrow$ ($\times 10^{-3} e^2 fm^2$)
7394.50(40)	1^-	103(17)	488(79)	3.5(6)
7344.40(70)	1^-	92(18)	430(84)	
7337.50(70)	1^-	128(19)	597(89)	4.3(6)
7326.20(70)	1^-	58(14)	269(66)	
7308.50(90)	1^-	58(14)	268(65)	
7295.50(70)	1^-	156(12)	720(55)	5.3(4)
7258.60(100)	1^-	59(19)	270(85)	
7233.80(80)	1^-	55(15)	249(68)	
7125.70(70)	1^-	85(12)	374(53)	
7086.50(70)	1^-	72(12)	313(53)	
7071.10(80)	1^-	80(11)	347(48)	
7062.20(90)	1^-	41(10)	176(43)	
7032.50(70)	1^-	111(12)	472(52)	3.9(4)
7018.00(80)	1^-	100(12)	427(52)	
6947.50(80)	1^-	69(13)	288(55)	
6938.90(80)	1^-	68(13)	283(54)	
6928.20(80)	(1)	77(20)	320(83)	
6902.10(80)	1^-	98(12)	404(50)	3.5(4)
6847.10(80)	1^-	125(14)	508(57)	4.5(5)
6808.00(60)	$1^{(+)}$	105(14)	422(56)	0.3(5)[1]
6790.60(80)	1^-	160(19)	639(76)	5.8(7)
6775.60(80)	1^-	136(24)	541(96)	

continued on next page

Observed levels in Gent Experiment (continued)

E_x (keV)	J^π	I_s (eV b)	Γ_0 (meV)	$B(\sigma l) \uparrow$ ($\times 10^{-3} e^2 fm^2$)
6764.20(80)	1^-	197(25)	781(99)	7.2(9)
6722.30(60)	1^-	177(18)	693(75)	
6713.60(70)	1^-	227(21)	883(86)	8.3(8)
6705.40(80)	1^-	121(17)	471(66)	4.5(6)
6683.30(80)	1^-	165(21)	639(85)	6.1(8)
6677.90(70)	1^-	280(23)	1083(89)	10.4(9)
6635.60(60)	1^-	307(23)	1171(88)	11.4(9)
6599.80(70)	1^-	94(20)	335(76)	
6584.10(60)	1^-	161(17)	605(64)	6.0(6)
6565.80(80)	1^-	143(18)	534(67)	
6560.80(70)	1^-	348(31)	1299(116)	13.1(12)
6548.50(50)	1^-	188(20)	699(74)	
6524.00(50)	1^-	219(25)	808(92)	8.3(9)
6503.20(60)	1^-	99(16)	363(59)	
6467.50(60)	1^-	132(12)	478(44)	
6453.00(70)	1^-	97(12)	350(44)	
6369.10(70)	1^-	469(27)	1650(95)	18.2(11)
6321.60(70)	1^-	189(17)	654(59)	7.4(7)
6287.10(70)	1^-	88(14)	301(48)	
6236.50(70)	1^-	211(19)	711(65)	
6184.00(60)	1^-	147(17)	487(57)	5.9(7)
6170.80(120)	1^-	133(13)	439(43)	

continued on next page

Observed levels in Gent Experiment (continued)

E_x (keV)	J^π	I_s (eV b)	Γ_0 (meV)	$B(\sigma l)\uparrow$ ($\times 10^{-3} e^2 fm^2$)
6129.00(70)	1^-	171(18)	557(59)	
6002.00(70)	1^-	86(13)	268(41)	
5968.40(70)	1^-	68(12)	210(37)	
5951.70(70)	1^-	108(15)	331(46)	
5902.50(70)	1^-	28(10)	85(31)	
5869.70(80)	(1)	30(6)	90(18)	
5842.50(70)	1^-	151(12)	446(36)	6.4(5)
5064.70(70)	1^-	29(6)	65(14)	
4953.70(70)	1^-	15(31)	33(7)	
4605.70(60)	1^-	25(6)	45(11)	
4263.40(60)	1^-	12(18)	19(30)	
4219.10(60)	1^-	22(24)	34(37)	
		$\sum B(E1)\uparrow$		377(5)
		$\sum E_x B(E1)\uparrow$	$[MeVe^2fm^2]$	2629(37)
		$\sum E_x B(E1)\uparrow$	[% EWSR]	0.595(8)
		$< E_x >$	(MeV)	6.97(14)

Table C.2: Summed electric dipole strength from ^{124}Sn Gent data in various energy ranges.

ΔE MeV	$\sum I_S$ MeV b	$\sum B(E1)\uparrow$ $\times 10^{-3}\ e^2fm^2$	$\sum E_x B(E1)\uparrow$ $keVe^2fm^2$	% EWSR	$< E_x >$ MeV
5-8	9.74(14)	345(5)	2612(37)	0.591(8)	7.56(15)
6.2-8.4	8.70(14)	303(5)	2125(34)	0.481(7)	7.00(16)
6-7.4	6.62(12)	241(4)	1611(30)	0.365(7)	6.67(18)

D Observed Transitions in ^{112,124}Sn

Table D.1: Properties of observed levels in ^{124}Sn. New states are marked by a *. Transitions with a weak azimuthal asymmetry are marked by an $^{\diamond}$. These transititons will be discussed in more detail in Section D.0.2.

E_x (keV)	J^π	ϵ	I_s (eV b)	Γ_0 (meV)	$B(\sigma l)\uparrow$ ($\times 10^{-3} e^2 fm^2$)
6251.74(190)*	1^-	-0.43(20)	96(21)	326(72)	3.83(85)
6286.04(110)	1^-	-0.18(13)$^{\diamond}$	98(17)	339(59)	3.91(68)
6321.69(73)	1^-	-0.50(8)	148(15)	516(53)	5.86(60)
6367.77(52)	1^-	-0.71(3)	465(25)	1635(88)	18.16(98)
6417.27(7)*	1^-	-0.63(11)	121(14)	432(50)	4.69(5)
6427.12(92)*	1^-	-0.50(9)	188(20)	676(71)	7.31(76)
6443.18(92)*	1^-	-0.93(2)	176(25)	636(90)	6.82(96)
6454.8(9)	1^-	-0.63(15)	147(21)	533(79)	5.69(8)
6466.3(1)	1^-	-0.98(2)	126(30)	458(110)	4.86(116)
6847.31(120)	1^-	-0.98(2)	81(9)	330(38)	2.95(33)
6863.61(180)*	1^+	-0.04(29)$^{\diamond}$	38(6)	156(24)	0.13(2)[1]
6903.28(66)	1^-	-0.80(5)	70(6)	291(27)	2.54(23)
6915.13(66)*	1^+	0.53(13)	61(5)	256(21)	0.20(2)[1]
6929.14(69)	1^-	-0.33(14)	47(5)	196(20)	1.69(17)
6941.19(52)	1^-	-0.95(2)	55(5)	231(21)	1.99(18)

continued on next page

[1] M1+E2 Transition in μ_N^2

Properties of observed levels in ^{124}Sn (continued)

E_x (keV)	J^π	ϵ	I_s (eV b)	Γ_0 (meV)	$B(\sigma l) \uparrow$ ($\times 10^{-3} e^2 fm^2$)
6949.23(45)	1^-	-0.77(10)	72(6)	305(24)	2.61(20)
6971.92(46)*	1^-	-0.54(7)	90(6)	379(27)	3.21(23)
7019.03(48)	1^-	-0.63(11)	97(8)	417(35)	3.46(29)
7036.03(120)	1^-	-0.69(5)	103(10)	443(41)	3.65(34)
7063.40(1000)	1^-	-0.18(14)$^\diamond$	46(7)	199(32)	1.62(26)
7071.91(51)	1^-	-0.67(7)	78(6)	339(27)	2.75(22)
7086.72(56)	1^-	-0.50(9)	83(6)	363(27)	2.93(22)
7126.63(96)	1^-	-0.041(270)$^\diamond$	89(8)	393(33)	3.11(22)
7169.85(110)*	1^-	-0.65(13)	48(5)	216(22)	1.68(17)
7202.72(70)*	1^-	-0.66(8)	65(5)	295(22)	2.27(17)
7216.49(48)*	1^-	-0.73(6)	78(5)	356(24)	2.72(18)
7234.51(50)	1^-	-0.87(1)	79(5)	361(24)	2.73(18)
7257.90(57)	1^-	-0.79(4)	69(5)	315(24)	2.36(18)
7281.25(43)*	1^-	-0.70(8)	133(8)	613(38)	4.55(28)
7296.06(47)	1^-	-0.59(9)	140(9)	646(43)	4.77(32)
7308.19(92)	1^-	-0.53(11)	68(8)	315(38)	2.32(28)
7327.00(71)	1^-	-0.59(7)	61(7)	286(34)	2.09(25)
7338.62(47)	1^-	-0.54(8)	86(8)	405(36)	2.94(36)
7347.71(48)	1^-	-0.84(5)	111(8)	522(39)	3.78(28)
7397.46(82)*	1^-	-0.98(1)	136(14)	647(68)	4.58(48)
7459.12(65)*	1^-	-0.59(6)	96(8)	466(37)	3.22(25)
7485.92(52)	1^-	-0.58(7)	79(6)	384(30)	2.63(21)

continued on next page

Properties of observed levels in ^{124}Sn (continued)

E_x (keV)	J^π	ϵ	I_s (eV b)	Γ_0 (meV)	$B(\sigma l)\uparrow$ ($\times 10^{-3} e^2 fm^2$)
7505.29(100)*	1^-	-0.52(7)	55(5)	272(26)	1.85(17)
7535.17(37)	1^-	-0.36(9)	79(5)	393(26)	2.64(17)
7548.62(45)	1^-	-0.89(1)	75(5)	375(25)	2.50(17)
7563.70(64)	1^-	-0.74(6)	55(5)	274(25)	1.82(16)
7574.80(47)	1^-	-0.81(3)	96(7)	482(35)	3.18(23)
7596.7(4)	1^-	-0.89(1)	104(6)	525(35)	3.44(2)
7608.2(5)	1^-	-0.89(1)	143(11)	722(60)	4.70(4)
7638.61(120)	1^-	-0.99(1)	52(9)	267(46)	1.72(30)
7651.01(100)*	1^-	0.00(23)$^\diamond$	77(11)	391(54)	2.50(34)
7663.66(96)	1^-	-0.44(13)	67(10)	344(50)	2.20(31)
7678.66(77)	1^-	-0.31(13)	73(8)	376(42)	2.38(32)
7685.61(44)	1^-	-0.96(1)	92(8)	472(43)	2.98(27)
7692.64(54)	1^-	-0.66(8)	72(8)	370(39)	2.33(24)
7701.44(67)	1^-	-0.69(10)	69(8)	357(41)	2.24(36)
7731.93(94)*	1^-	-0.59(11)	71(7)	371(37)	2.30(23)
7745.45(57)	1^-	-0.51(9)	115(8)	599(42)	3.70(26)
7757.56(46)	1^-	-0.47(5)	94(7)	491(36)	3.02(22)
7768.67(41)	1^-	-0.68(6)	89(7)	469(35)	2.87(22)
7776.26(8)	1^-	-0.59(6)	67(5)	350(29)	2.14(17)
7787.43(6)	1^-	-0.68(8)	70(6)	350(29)	2.14(17)
7814.31(46)	1^-	-0.59(8)	265(16)	1406(83)	8.45(50)
7828.45(64)*	1^-	-0.69(9)	67(7)	358(38)	2.14(23)

continued on next page

Properties of observed levels in ^{124}Sn (continued)

E_x (keV)	J^π	ϵ	I_s (eV b)	Γ_0 (meV)	$B(\sigma l)\uparrow$ ($\times 10^{-3} e^2 fm^2$)
7848.46(83)*	1^-	-0.62(6)	65(7)	349(37)	2.07(22)
7861.47(6)	1^-	-0.43(11)	78(7)	419(36)	2.47(2)
7869.72(4)	1^-	-0.40(10)	62(5)	336(29)	1.98(2)
7879.30(51)	1^-	-0.48(7)	149(18)	806(97)	4.73(6)
7893.89(43)*	1^-	-0.54(6)	97(6)	526(34)	3.07(20)
7907.90(44)	1^-	-0.59(5)	71(5)	386(29)	2.24(17)
7915.67(47)	1^-	-0.57(7)	56(5)	307(29)	1.78(17)
7928.54(97)*	1^-	-0.71(6)	80(14)	438(79)	2.52(45)
7935.57(85)	1^-	-0.76(6)	51(6)	279(32)	1.60(18)
7945.89(78)*	1^-	-0.62(7)	89(15)	490(84)	2.80(48)
7957.91(51)	1^-	-0.43(8)	122(8)	667(46)	3.79(26)
7976.50(54)*	1^-	-0.51(6)	107(11)	593(59)	3.35(33)
7996.77(91)	1^-	-0.57(10)	86(13)	479(72)	2.69(40)
8059.56(140)*	1^-	-0.60(7)	200(18)	1126(100)	6.17(54)
8093.67(120)*	1^-	-0.21(15)	48(9)	274(50)	1.49(27)
8118.61(80)	1^-	-0.60(7)	116(10)	664(59)	3.56(32)
8135.64(86)	1^-	-0.65(7)	95(9)	548(53)	2.92(28)
8162.71(92)	1^-	-0.88(1)	58(8)	336(45)	1.78(24)
8197.28(300)*	1^-	-0.97(2)	36(7)	211(39)	1.10(20)
8231.59(140)	1^-	-0.65(8)	84(7)	495(42)	2.54(22)
8258.52(87)	1^-	-0.55(7)	79(9)	645(53)	2.36(27)
8271.39(180)	1^-	-0.43(9)	120(13)	710(76)	3.59(38)

continued on next page

Properties of observed levels in ^{124}Sn (continued)

E_x (keV)	J^π	ϵ	I_s (eV b)	Γ_0 (meV)	$B(\sigma l)\uparrow$ ($\times 10^{-3} e^2 fm^2$)
8307.50(220)*	1^-	-0.45(6)	159(19)	955(116)	4.78(58)
8349.81(10)	1^-	-0.71(6)	125(14)	757(86)	3.73(42)
8382.94(80)	1^-	-0.66(5)	147(14)	899(85)	4.38(41)
8394.63(90)*	1^-	-0.89(2)	86(12)	526(71)	2.55(35)
8424.51(93)	1^-	-0.75(6)	104(12)	640(73)	3.07(35)
8450.32(210)*	1^-	-0.43(7)	163(22)	1009(135)	4.80(63)
			$\sum B(E1)\uparrow$	[$\times 10^{-3}$ $e^2 fm^2$]	289(4)
			$\sum E_x B(E1)\uparrow$	[$MeV e^2 fm^2$]	2130(27)
			$\sum E_x B(E1)\uparrow$	[% EWSR]	0.482(6)(5)
			$< E_x >$	(MeV)	7.37(14)

D.0.2 Transitions with Weak Azimuthal Asymmetry

For the most part, the transitions are all electric dipole. Five states seem to exhibit an isotropic distribution, obscuring any parity determination. These states correspond to very weak transitions, and as a result, they are are markedly susceptible to background fluctuations. The energy, integrated cross section, and azimuthal asymmetry of these transitions are given in Table D.4. When TOF cuts are used to eliminate some of the background, the azimuthal asymmetry for most of these states becomes less ambiguous and more clearly of E1 character.[2] The one exception is the state at 6.863 MeV. This state seems to become slightly more positive as the background counts are eliminated. The lack of any azimuthal asymmetry suggests that higher multipoles are contributing to the angular distribution. Since transitions of E1+M2 character are very rare, the de-excitation is probably a

[2] In general, the spectra were clean enough to be examined without the use of TOF cuts.

E_x (keV)	J^π	ϵ	I_s (eV b)	Γ_0 (meV)	$B(\sigma l)\uparrow$ ($\times 10^{-3} e^2 fm^2$)
7248.1(14)	1^-	-0.31(13)	59(25)	267(112)	2.01(1)
7229.3(14)	1^-	-0.57(10)	49(30)	222(136)	1.68(1)
7217.6(11)	1^-	-0.60(8)	55(22)	248(101)	1.89(1)
7207.9(10)	1^-	-0.24(10)	34(16)	154(73)	1.18(1)
7199.6(9)	1^-	-0.21(11)	77(32)	346(143)	2.66(1)
6819.4(11)	1^-	-0.54(9)	87(27)	350(109)	3.16(1)
6791.6(23)	1^-	-0.26(11)	55(25)	220(99)	2.01(1)
6735.2(14)	1^-	-0.30(11)	72(34)	284(134)	2.66(1)
6718.7(13)	1^-	-0.50(10)	82(36)	321(143)	3.03(1)
6476.1(15)	1^-	-0.91(2)	194(100)	707(364)	7.46(4)
6431.6(8)	1^-	-0.78(6)	127(59)	454(211)	4.89(2)
6402.0(2)	1^-	-0.69(5)	218(81)	776(289)	8.47(3)
6384.9(4)	1^-	-0.63(7)	133(55)	470(193)	5.17(2)
			$\sum B(E1)\uparrow$	[$\times 10^{-3}$ $e^2 fm^2$]	46.27(7)
			$\sum E_x B(E1)\uparrow$	[$MeV e^2 fm^2$]	308.5(4)
			$\sum E_x B(E1)\uparrow$	[% EWSR]	0.0753(1)
			$< E_x >$	(MeV)	6.67(1)

Table D.2: Properties of observed levels in ^{112}Sn.

mixture of M1+E2 radiation.

D.0.3 Error Propogation

This sections discusses the error propogation for various calculations in this dissertation. Included here are the formulas used, as well as sample calculations using Table D.1.

Summed Dipole Strength

$$\sum_i B_i(E1) \tag{D.1}$$

Calculating the summed dipole strength involves summing up the terms in column six of Table D.1 or D.2. The error in the summed dipole strength is simply the square-root of the sum of the squared uncertainties in the individual values.

^{124}Sn	E_x (keV)	$\sigma_{\gamma\gamma}$ (mb)	D (keV)	B_0 %	Γ_0 (eV)	$B(E1)\uparrow$ $(x10^{-3}e^2fm^2)$
	8389(6)	5.48(25)	19.54	43(2)	15.03(92)	72.96(4)
	8209(6)	4.97(17)	19.00	43(2)	12.72(77)	65.93(4)
	7911(3)	5.25(18)	12.74	42(9)	8.67(186)	50.16(10)
	7740(5)	6.26(20)	10.90	48(3)	7.45(48)	46.02(3)
	7540(4)	5.44(18)	13.55	46(2)	7.97(43)	53.29(2)
	7330(4)	6.37(26)	14.77	46(2)	9.49(57)	69.06(4)
	7217(4)	4.70(16)	18.73	49(15)	8.17(249)	62.32(19)
	7089(5)	4.76(22)	12.31	52(18)	4.89(168)	39.36(13)
	6960(3)	3.68(15)	15.82	52(6)	4.72(60)	40.15(5)
	6340(5)	11.76(42)	16.53	55(4)	12.33(99)	138.65(11)
				$\sum BE1\uparrow$	$[x10^{-3}e^2fm^2]$	638(30)
				$\sum E_xBE1\uparrow$	$[MeVe^2fm^2]$	4702(215)
					% EWSR	1.06(5)
				$<E_x>$	MeV	7.37(48)

^{112}Sn	E_x (keV)	$\sigma_{\gamma\gamma}$ (mb)	D (keV)	B_0 %	Γ_0 (eV)	$B(E1)\downarrow$ $(x10^{-3}e^2fm^2)$
	7281(8)	4.83(28)	8.08	79(13)	2.27(39)	16.87(2)
	6800(4)	3.87(23)	20.14	79(13)	3.96(69)	36.07(6)
	6415(5)	5.96(30)	18.34	80(12)	4.88(77)	52.95(8)
				$\sum BE1\uparrow$	$[x10^{-3}e^2fm^2]$	74(2)
				$\sum E_xBE1\uparrow$	$[MeVe^2fm^2]$	708(72)
					% EWSR	0.17(2)
				$<E_x>$	MeV	6.68(97)

Table D.3: Averaged elastic cross section for ^{112,124}Sn of energy range. The second column corresponds to the number of energy levels observed in the specific energy range. The third and fourth column refer to the ground state decay width and the reduced transitions strength respectively. Both of these quantities were calculated assuming the experimentally observed branching ratio.

E_x	I_s	ε	
$[keV]$	$[eVb]$	raw data(%)	TOF cut
7651	52(9)	0.0025(2337)	-0.248(136)
7126	89(8)	-0.041(270)	-0.332(111)
7063	46(7)	-0.176(150)	-0.214(110)
6286	98(17)	-0.179(132)	-0.361(106)
6863	63(33)	-0.041(300)	0.104(115)

Table D.4: Characteristics of weak states for which parity could not be established. The parity of the 7639 keV was determined in the Gent experiment to be 1^-. All levels except for the 6863-keV level were previously measured by the Gent group.

Summed Energy Weighted Dipole Strength

The summed-energy-weigthed dipole strength is given by

$$\sum_i E_{xi} B_i(E1), \tag{D.2}$$

where E_{xi} is the excitation energy of the individual resonance (see column one of Table D.1 or D.2), and $B_i(E1)$ is the transition strength at that energy (see column six of same tables). The error in the summed dipole strength is given by

$$\Delta \left(\sum_i E_{xi} B_i(E1) \right)^2 = \sum_i \left(\frac{\Delta E_{xi}}{E_{xi}} \right)^2 + \left(\frac{\Delta B_i(E1)}{B_i(E1)} \right)^2. \tag{D.3}$$

Often, the summed-energy-weighted dipole strength is quoted in units of the EWSR. This corresponds to

$$\sum_i E_{xi} B_i(E1)[\%EWSR] = \frac{\sum_i E_{xi} B_i(E1)}{S(E1)_{TRK}}, \tag{D.4}$$

where $S(E1)_{TRK}$ is the EWSR given in Equation 5.8 on page 81. Since there is no error associated with the EWSR, the uncertainty is obtained by dividing the normal summed-energy-weighted dipole strength uncertainty (see Equation D.3) by the EWSR.

In some theoretical calculations, rather than comparing the summed-energy weighted strength to the EWSR, they compare it to the total strength in the GDR. These calculations can be compared

with theoretical calculations using

$$\frac{\sum_{E<E_{cut-off}} E_x B_i(E1)}{\sum_{E>E_{cut-off}} E_x B_i(E1)}, \tag{D.5}$$

where $E_{cut-off}$ is some arbitray energy, usually determined by the Theoretician, that seperates the PDR from the GDR. Again, the error is determined using the error of a ratio, where the individual errors are given by Equation D.3.

Average Excitation Energy

The average excitation energy for an energy region is given by

$$< E_x >= \frac{\sum_i E_{xi} B_i(E1)}{\sum_i B_i(E1)} \tag{D.6}$$

where E_{xi} is the excitation energy of the individual resonance (column one of Table D.1 or D.2), and $B_i(E1)$ is the transition strength at that energy (see column six of same tables). The error is calculated using the normal propogation of errors procedure.

E Results Appendix

In this section I shall present all of the information which supplements the results given in Chapter 5. Since there were so many levels observed, and so many calculations preformed, the inclusion of all this information in Chapter 5 would have disrupted the flow of ideas. In the spirit of full disclosure, these additional calculations have been included in this Appendix. In order to make this chapter as easy as possible to navigate, I have arranged a Table the information presented in this chapter and what page it is on.

Table of Contents

^{124}Sn	E_x	Average Number of Intermediate Transitions					
	(MeV)	SP	BA	Sir	KMF	GLO	GEM
	6.4	3.24	2.54	2.40	3.14	2.90	1.53
	6.9	3.44	2.93	2.74	3.55	3.26	1.79
	7.08	3.55	2.99	2.77	3.20	3.35	1.71
	7.2	3.54	3.11	2.86	3.31	3.44	1.83
	7.3	3.62	3.21	2.96	3.40	3.52	1.91
	7.5	3.73	3.35	3.09	4.00	3.67	2.04
	7.7	4.33	3.37	3.08	4.03	3.69	2.18
	7.9	4.45	3.55	3.26	4.19	3.86	2.31
	8.2	4.59	3.65	3.36	4.33	3.99	2.45
	8.4	4.66	3.69	3.38	4.40	4.05	2.42

^{112}Sn	E_x	Average Number of Intermediate Transitions					
	(MeV)	SP	BA	Sir	KMF	GLO	GEM
	6.4	3.57	2.67	2.70	2.81	2.99	2.01
	6.8	3.75	2.89	2.83	2.99	3.15	2.13
	7.28	3.88	2.99	2.88	3.09	3.25	2.09
	9.0	4.55	3.60	3.38	3.67	3.80	2.56

Table E.1: Average number of transitions for various γ-ray strength functions.

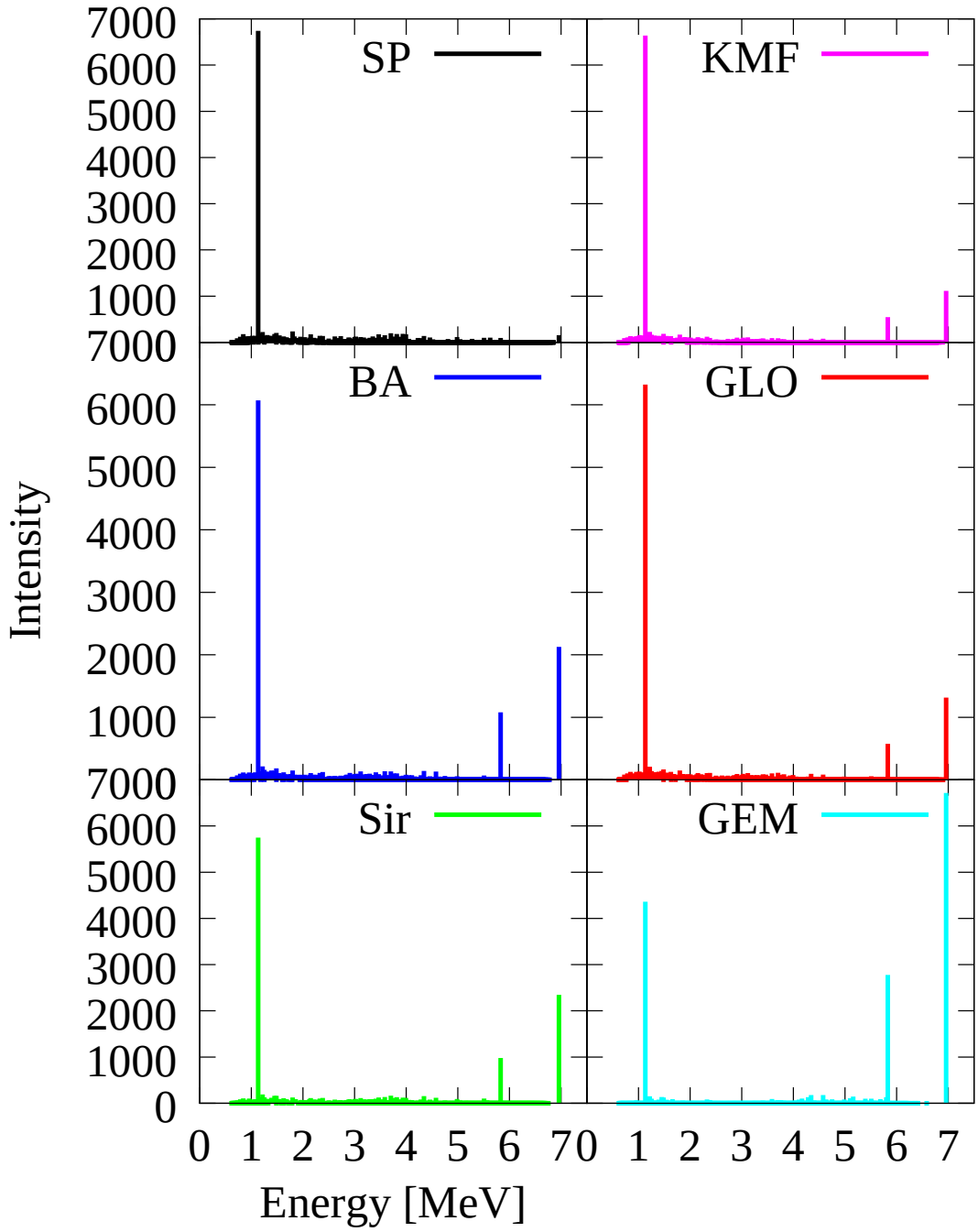

Figure E.1: Simulation of spectra observed from 6.9 MeV excitation in ^{124}Sn. These spectra correspond to what is expected according to the various models in one of the detectors in the vertical plane (detector 2). The spectra have been corrected for the angular distribution of different transitions and the efficiency of the detector.

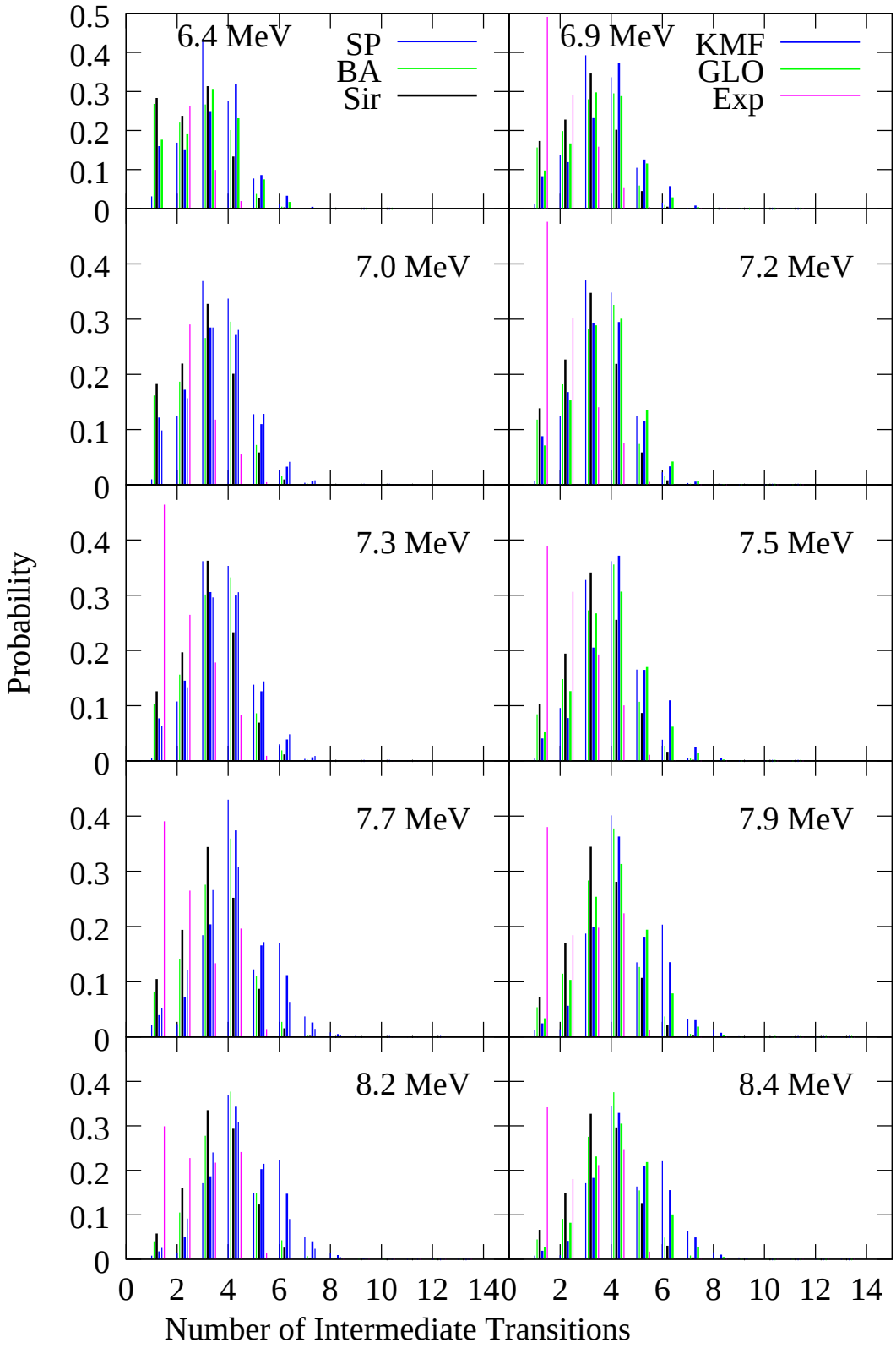

Figure E.2: Average number of transitions needed to get to the ground state in ^{124}Sn for various models. All the models seem to prefer 3- or 4-step cascades in decaying to the ground state. Although at the lower energies, there is a higher probability of cascades that involve fewer than 4-steps.

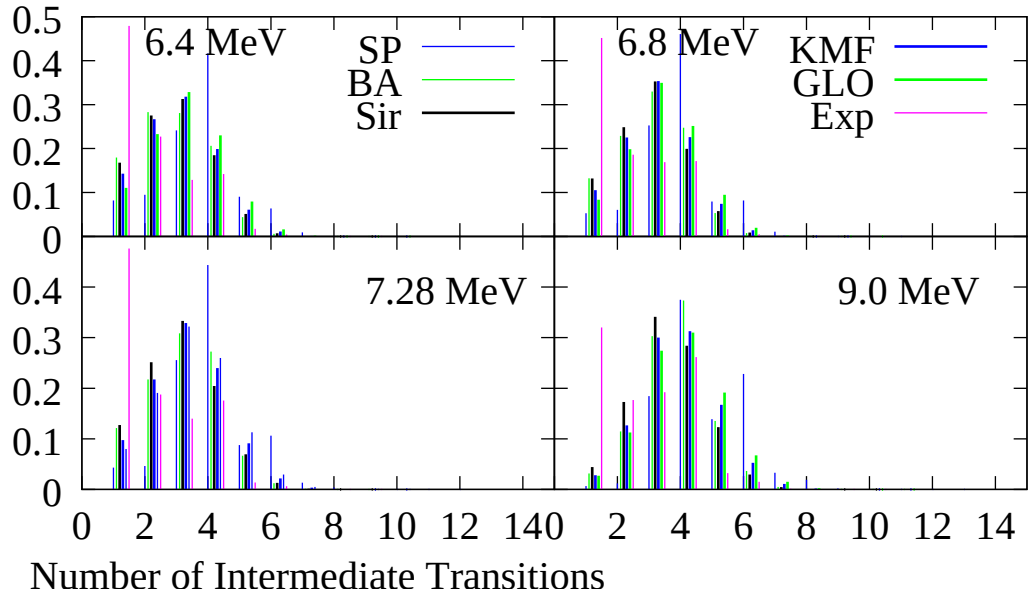

Figure E.3: Average number of transitions needed to get to the ground state in ^{112}Sn

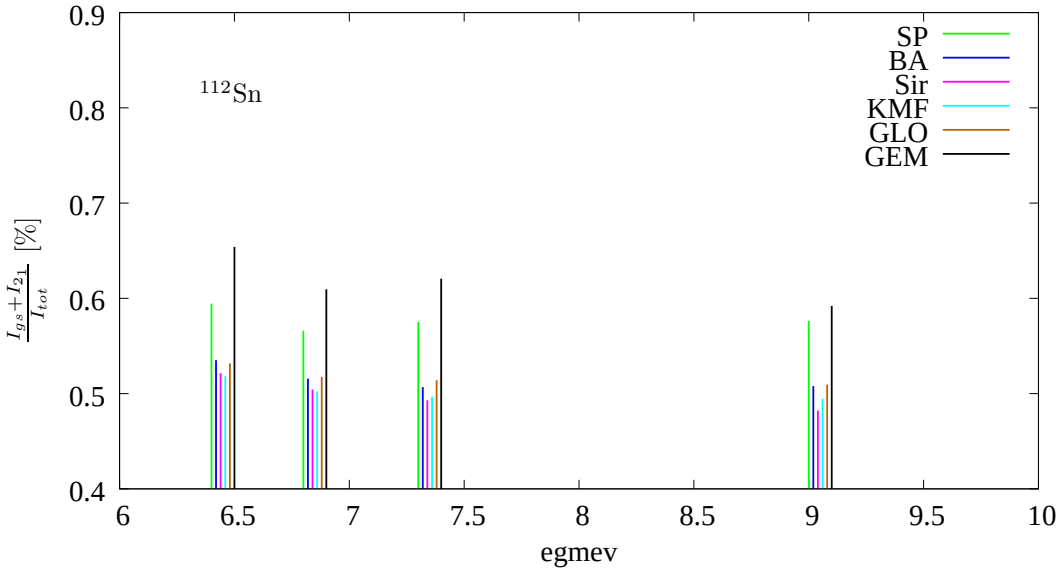

Figure E.4: Percentage of total intensity in the 2_1^+ and E_x peaks for various models in ^{112}Sn.

^{124}Sn	E_x	$\sigma_{\gamma\gamma}$				$\frac{I_{gs}}{I_{tot}}$ [%]			
	(MeV)	(mb)	data	SP	BA	Sir	KMF	GLO	GEM
	8.39	5.08(2)	73(5)	33(6)	40(6)	43(2)	35(5)	37(5)	52(11)
	8.21	4.70(1)	76(4)	32(8)	40(5)	43(2)	35(4)	37(4)	56(9)
	7.91	5.14(1)	77(5)	32(7)	38(7)	42(1)	33(5)	36(5)	50(19)
	7.74	5.93(2)	82(4)	34(10)	43(8)	48(3)	38(8)	41(7)	56(11)
	7.54	5.08(2)	82(3)	36(20)	41(1)	46(2)	35(13)	39(12)	57(16)
	7.33	6.68(2)	87(5)	36(10)	43(8)	46(2)	41(7)	41(7)	61(8)
	7.22	4.48(1)	87(3)	39(4)	44(11)	49(1)	43(8)	43(8)	60(34)
	7.09	4.38(2)	87(5)	38(4)	48(9)	52(2)	46(8)	44(7)	65(18)
	6.96	3.38(1)	86(4)	40(6)	48(9)	52(1)	42(7)	45(7)	62(16)
	6.34	11.21(5)	90(7)	38(14)	52(12)	55(4)	44(12)	46(12)	71(11)

^{112}Sn	E_x	$\sigma_{\gamma\gamma}$				$\frac{I_{gs}}{I_{tot}}$ [%]			
	(keV)	(mb)	data	SP	BA	Sir	KMF	GLO	Exp
	8.91	0.00(0)	0(0)	43(5)	50(3)	53(2)	51(4)	49(4)	52(3)
	7.28	4.43(2)	78(7)	41(7)	54(7)	56(7)	53(6)	50(6)	53(7)
	6.80	2.88(1)	80(6)	46(10)	55(10)	56(9)	54(8)	52(8)	55(9)
	6.37	5.09(0)	82(2)	46(10)	56(9)	56(5)	56(7)	53(7)	56(6)

Table E.2: Low-lying excitation in ^{112,124}Sn. Shown here are the elastic scattering cross section of the first excited state along with the ratio of ground state.

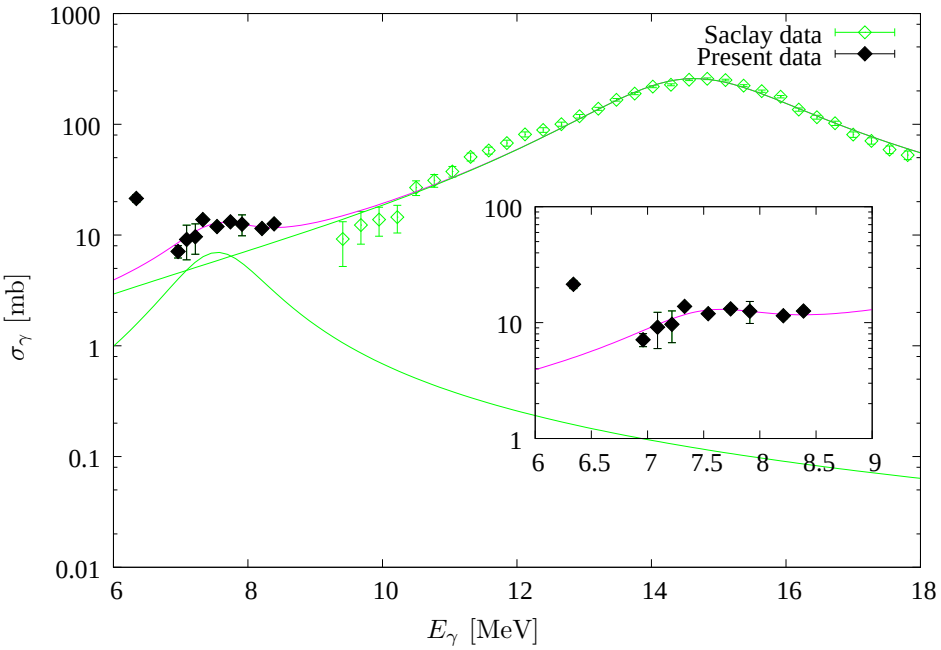

Figure E.5: Comparison of determined photo-absorption cross section from the present experiment with the measured cross section from the Saclay (γ, n) reaction [Lep71].

Nucleus	E_{level} keV	E_γ keV	$\pi\ell$	Branch %	Γ_γ meV
^{14}N	6446.17	611.91(17)	E1	3.7(6)	0.04(1)
		1340.21(14)	E1	6.5(6)	0.07(1)
		2497.83(23)	E2	19.7(10)	0.21(3)
		6444.58(10)	E2	70.1(15)	0.74(7)
	7029.12	3080.7(23)	M1	0.9(25)	<1.1(3)
		4715.47(12)	E2	0.5(1)	0.62(14)
		7027.22(12)	M1+E2	98.6	(M1)91(13) (E2)50(12)
	7966.9	4018.2(5)	E1	55(3)	10
		7964.5(5)	E1	45(3)	8
	8062.0	2371(10)	M1	3.5(4)	430(12)
		2956(10)	M1	0.25(14)	30(20)
		3147(1)	M1	1.86(14)	230(60)
		4113(10)	E1	12.7(4)	1560(400)
		5748(10)	E1	1.40(14)	170(50)
		8060(10)	E1	80.3(6)	9900(2500)
	8490	2656(2)	E2	17(3)	13(4)
		3384(2)	M1	83(3)	61(15)
^{16}O	6917.1	6915.6	E2	100	97(3)
	7116.85	7115.15(14)	E1	100	55(3)

Table E.3: Transitions in air that correspond to the observed energy region [Til93].

F NRF Spectra in ^{112,124}Sn

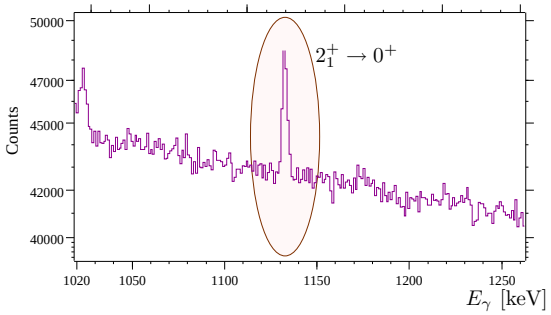

(a) First Excited State to the ground state transition for ^{124}Sn.

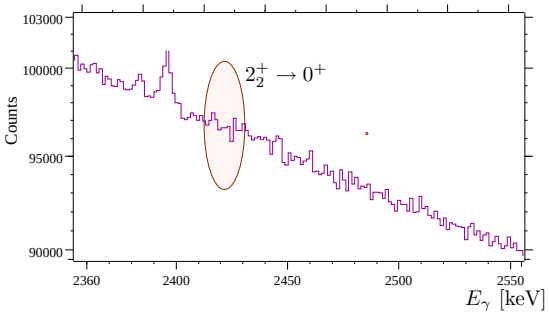

(b) 2_2^+ to ground state transition for ^{124}Sn.

Figure F.1: Spectra showing the location of the $2_1^+ \rightarrow 0^+$ and $2_2^+ \rightarrow 0^+$ transitions in ^{124}Sn. These spectra are summed spectra over all angles and energies. Interestingly enough, no transitions were observed from the 2_2^+ to the ground state.

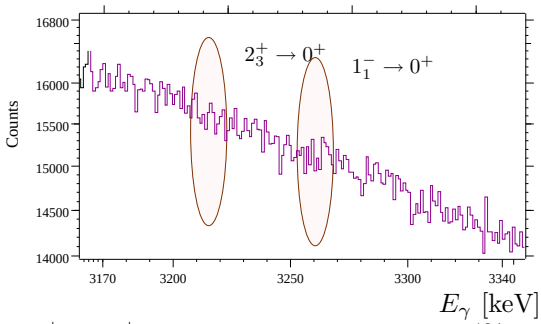

(a) 2_3^+ and 2_4^+ transitions to the ground state in ^{124}Sn.

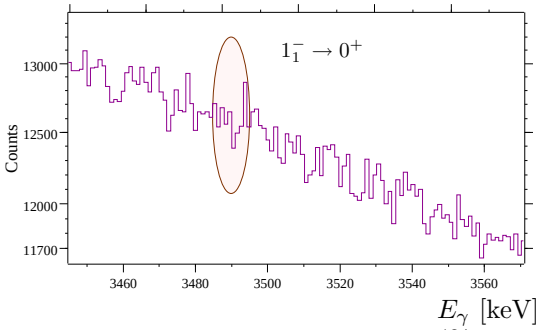

(b) 1_1^- transitions to the ground state in ^{124}Sn.

Figure F.2: Spectra showing the location of the $2_3^+ \rightarrow 0^+$, $2_4^+ \rightarrow 0^+$, and $1_1^- \rightarrow 0^+$ transitions in ^{124}Sn. These spectra are summed spectra over all angles and energies. Interestingly enough, none of these transitions were observed in the current experiment. This contradicts the results of the Gent experiment, which measured considerable feeding to all of these states.

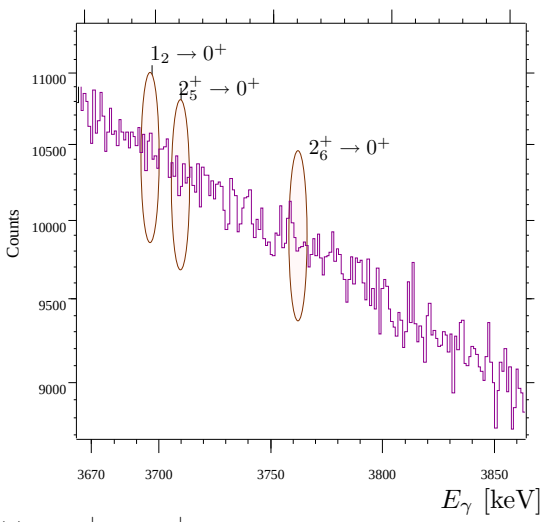

(a) 1_2, 2_5^+, and 2_6^+ transitions to the ground state in ^{124}Sn.

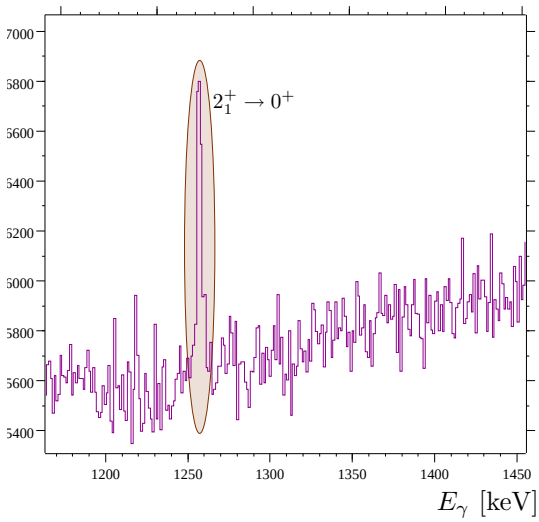

(b) First Excited State to the ground state transition for ^{112}Sn.

Figure F.3: Spectra showing the location of the $1_1^- \rightarrow 0^+$, $2_5^+ \rightarrow 0^+$, and the $2_6^+ \rightarrow 0^+$ transitions in ^{124}Sn, as well as the $2_1^+ \rightarrow 0^+$ transition in ^{112}Sn. These spectra are summed spectra over all angles and energies. Interestingly enough, none of these ^{124}Sn transitions were observed in the current experiment. The $2_1^+ \rightarrow 0^+$ transitions was observed even at 9.06 MeV, where no other ground-state transitions were observed.

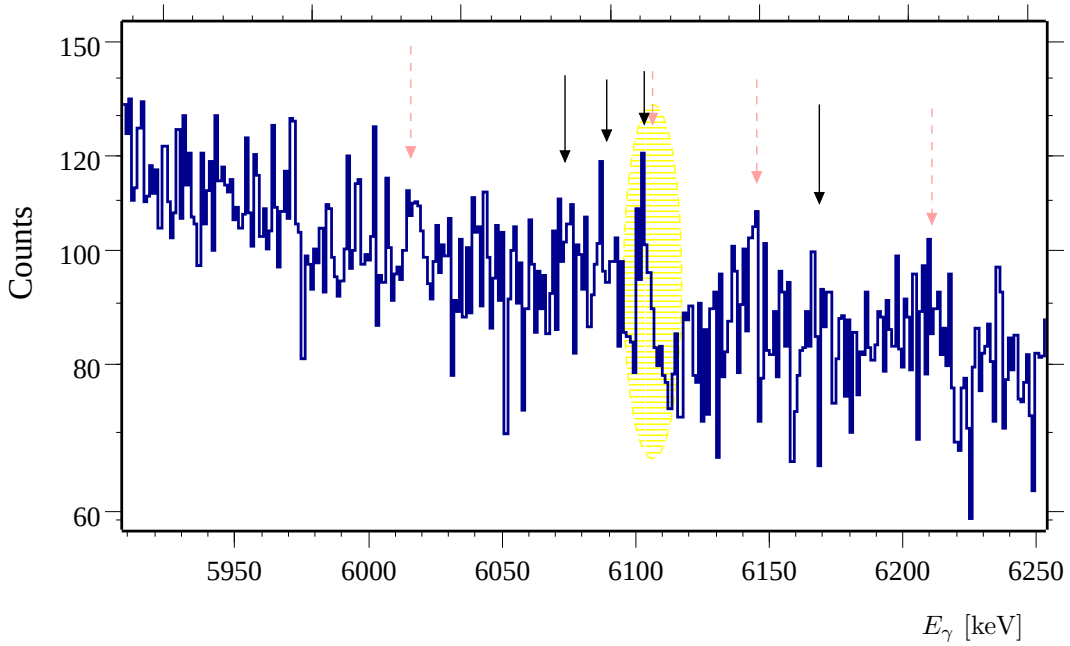

Figure F.4: The summed vertical detector spectrum in the energy region of the $2_1^+ \rightarrow 0^+$ and double escape peaks for ^{124}Sn. The black solid arrows indicate peaks that might correspond to $2_1^+ \rightarrow 0^+$, while the dashed pink arrows indicate double escape peaks. In some cases, the arrows overlap, this is the case for the peak encased in the yellow circle.

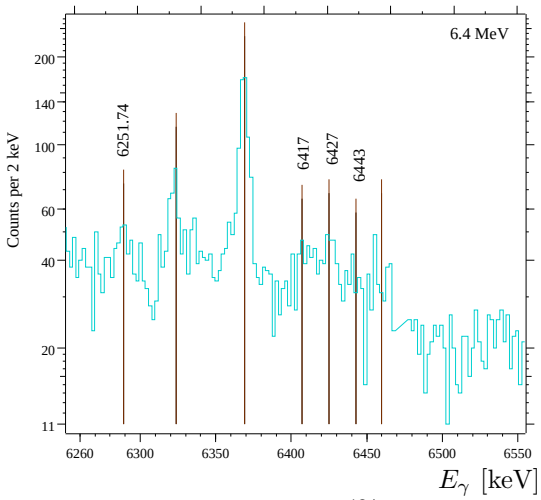

(a) Vertical detector spectrum for ^{124}Sn at E_{inc}=6.4 MeV.

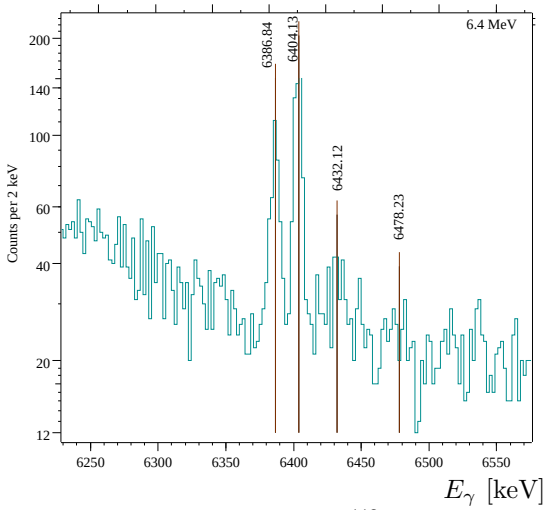

(b) Vertical detector spectrum for ^{112}Sn at E_{inc}=6.4 MeV.

Figure F.5: Vertical detector spectra at E_{inc}=6.4 MeV. The brown lines indicate the location of peak. The energies of new transitions are supplied above the vertical lines for their respective peak.

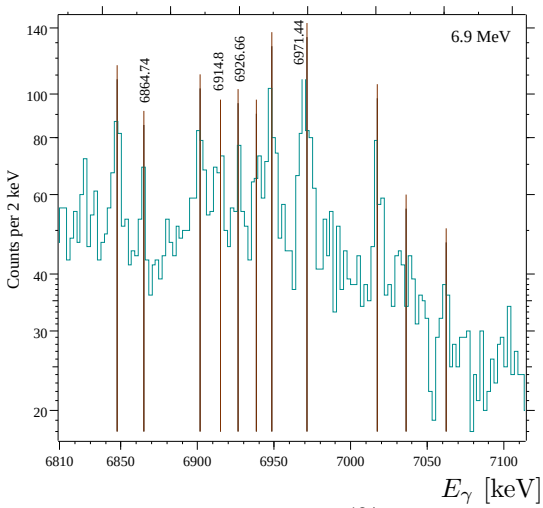

(a) Vertical detector spectrum for ^{124}Sn at E_{inc}=6.9 MeV.

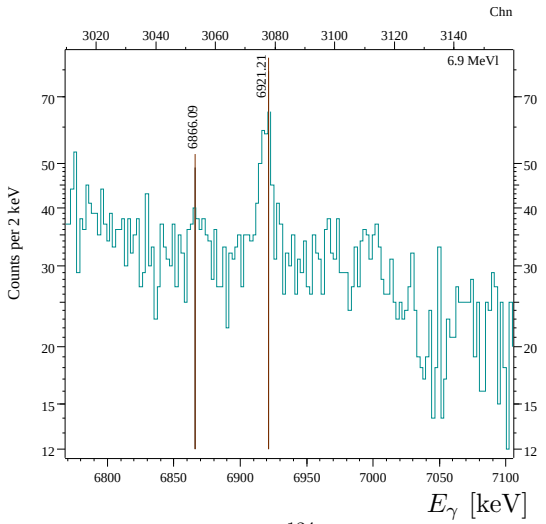

(b) Horizontal spectrum for ^{124}Sn at E_{inc}=6.9 MeV.

Figure F.6: Vertical and horizontal spectra at E_{inc}=6.9 MeV. The brown lines indicate the location of peak. The energies of new transitions are supplied above the vertical lines for their respective peak.

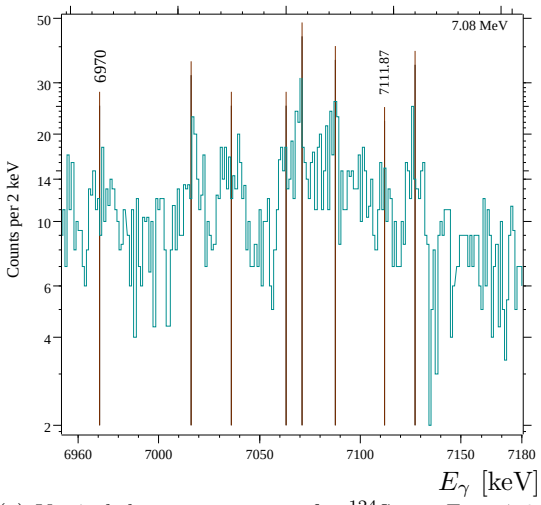

(a) Vertical detector spectrum for ^{124}Sn at E_{inc}=7.0 MeV.

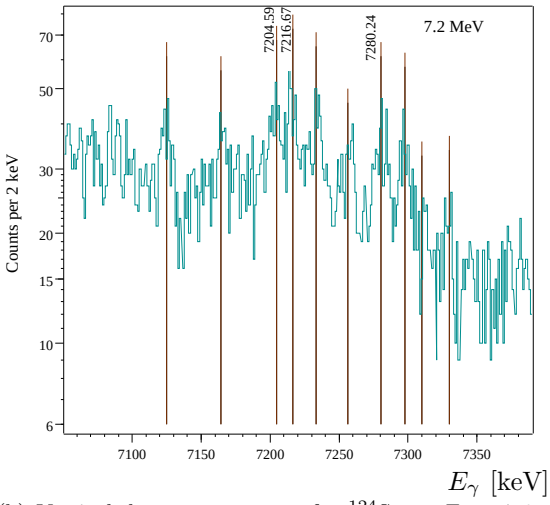

(b) Vertical detector spectrum for ^{124}Sn at E_{inc}=7.2 MeV.

Figure F.7: Vertical detector spectra at E_{inc}=7.0 and 7.2 MeV. The brown lines indicate the location of peak. The energies of new transitions are supplied above the vertical lines for their respective peak.

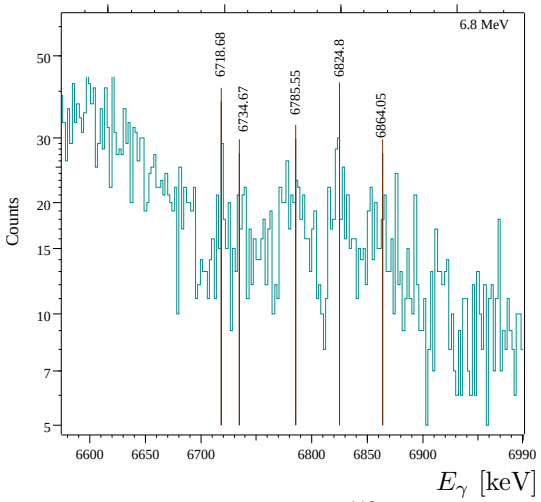

(a) Vertical detector spectrum for ^{112}Sn at E_{inc}=6.8 MeV.

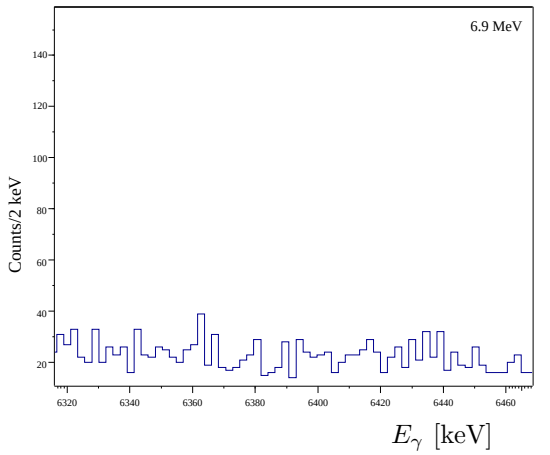

(b) Horizontal detector spectrum for $^{\text{nat}}$Sn at E_{inc}=6.9 MeV.

Figure F.8: Vertical detector spectra at E_{inc}=6.8 MeV and $^{\text{nat}}$Sn horizontal spectrum at 6.9 MeV. The brown lines indicate the location of peak. The energies of new transitions are supplied above the vertical lines for their respective peak.

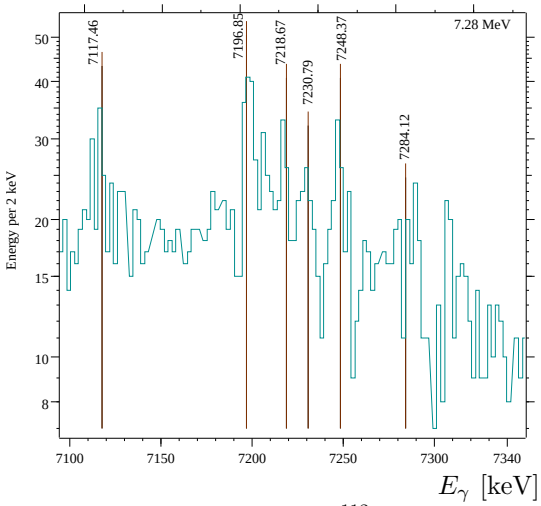

(a) Vertical detector spectrum for ^{112}Sn at E_{inc}=7.28 MeV.

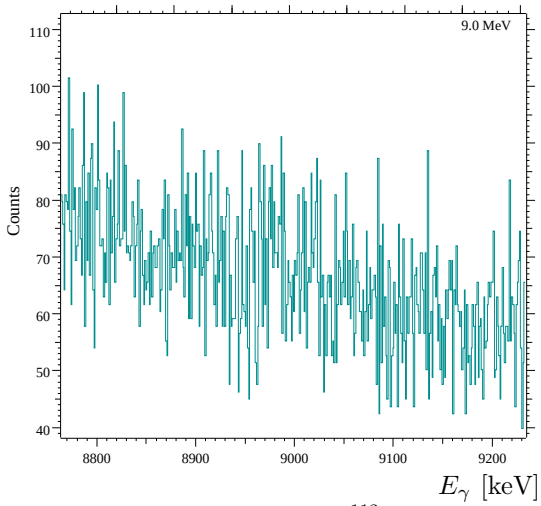

(b) Vertical detector spectrum for ^{112}Sn at E_{inc}=9.0 MeV.

Figure F.9: Vertical detector spectra at E_{inc}=7.28 and 9.0 MeV. The brown lines indicate the location of peak. The energies of new transitions are supplied above the vertical lines for their respective peak.

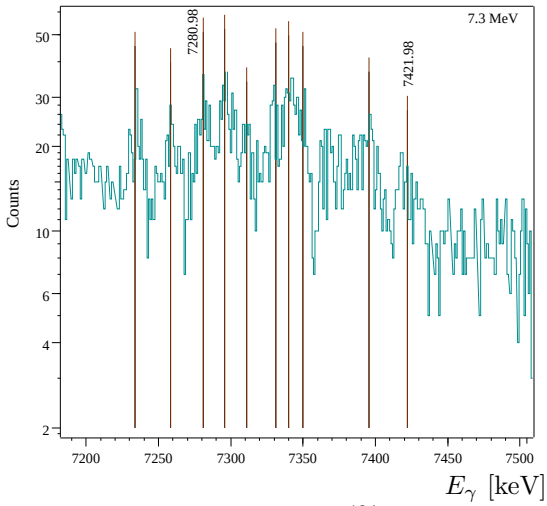

(a) Vertical detector spectrum for ^{124}Sn at E_{inc}=7.3 MeV.

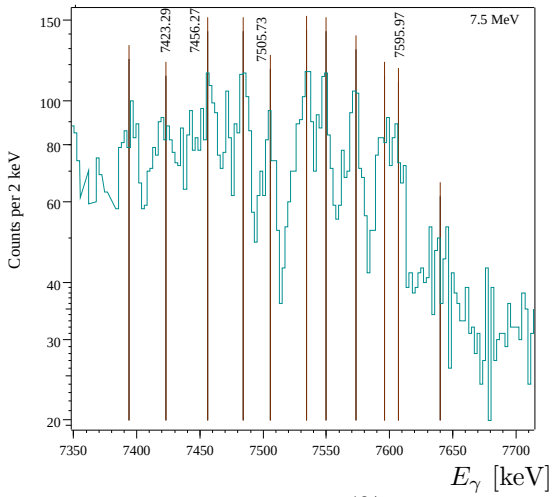

(b) Vertical detector spectrum for ^{124}Sn at E_{inc}=7.5 MeV.

Figure F.10: Vertical detector spectra at E_{inc}=7.3 and 7.5 MeV. The brown lines indicate the location of peak. The energies of new transitions are supplied above the vertical lines for their respective peak.

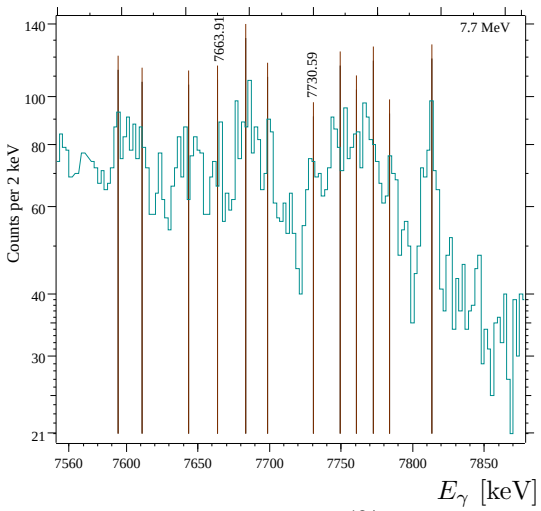

(a) Vertical detector spectrum for ^{124}Sn at E_{inc}=7.7 MeV.

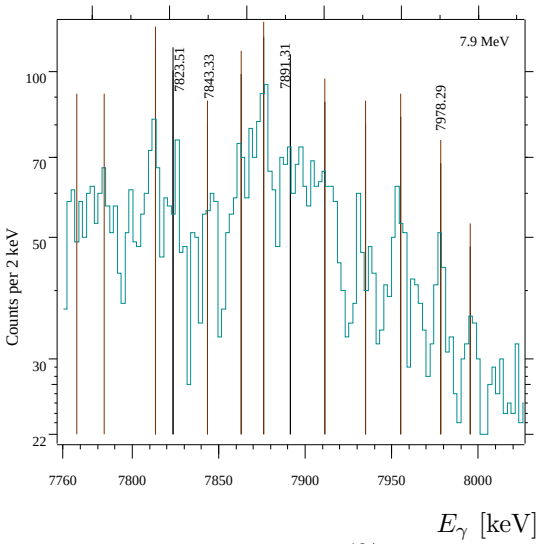

(b) Vertical detector spectrum for ^{124}Sn at E_{inc}=7.9 MeV.

Figure F.11: Vertical detector spectra at E_{inc}=7.7 and 7.9 MeV. The brown lines indicate the location of peak. The energies of new transitions are supplied above the vertical lines for their respective peak.

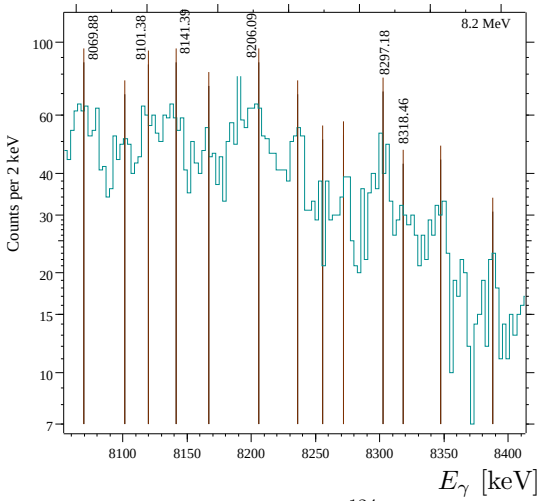

(a) Vertical detector spectrum for ^{124}Sn at E_{inc}=8.2 MeV.

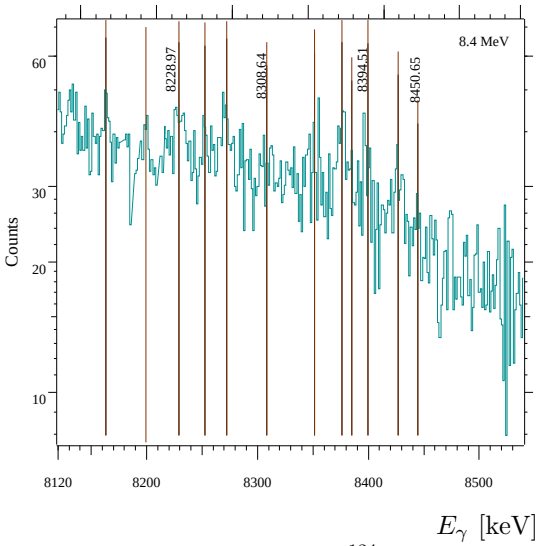

(b) Vertical detector spectrum for ^{124}Sn at E_{inc}=8.4 MeV.

Figure F.12: Vertical detector spectra at E_{inc}=8.2 and 8.4 MeV. The brown lines indicate the location of peak. The energies of new transitions are supplied above the vertical lines for their respective peak.

Bibliography

[Ajz90] F. Ajzenberg-Selove, "Energy levels of light nuclei A= 11-12", Nuclear Physics A **506**, 1 (1990).

[Ala87] R. Alarcon, R. Laszewski, A. Nathan, and S. Hoblit, "Photon scattering from ^{90}Zr below neutron emission threshold", Physical Review C **36**, 954 (1987).

[Ara73] B. Arad and G. Ben-David, "Nuclear studies with neutron-capture γ rays", Review of Modern Physics **45**, 230 (1973).

[Aud93] G. Audi, A. Wapstra, and M. Dedieu, "The 1993 atomic mass evaluation (IV): evaluation of input data, adjustment procedures", Nuclear Physics A **565**, 193 (1993).

[Axe62] P. Axel, "Electric dipole ground-state transition width strength function and 7-MeV photon interactions", Physical Review **126**, 671 (1962).

[Axe70] P. Axel, K. K. Min, and D. C. Sutton, "Intermediate structure in the photon interaction cross sections of Sn and Zr", Physical Review C **2**, 689 (1970).

[Baz59] A. Baz, "Threshold effects in nuclear reactions", Advances in Physics **8**, 349 (1959).

[Bec00] F. Becvar and M. Krticka, "Simulations of gamma cascades and modelling of atomic collision chains", Journal of Research from the National Institute of Standandards and Technology **105**, 113 (2000).

[Bel06] T. Belgya et al., "Handbook for calculations of nuclear reaction data, RIPL-2", Technical report, IAEA-TECDOC-1506 (IAEA, Vienna, 2006) available online at http://www-nds. iaea. org/RIPL-2, 2006.

[Bet36] H. Bethe, "An attempt to calculate the number of energy levels of a heavy nucleus", Physical Review **50**, 332 (1936).

[Bet37] H. Bethe, "Nuclear physics B. Nuclear dynamics, theoretical", Reviews of Modern Physics **9**, 69 (1937).

[Bev92] Bevington and Robinson, *Data reduction and error analysis for the physical sciences*, McGraw-Hill, 1992.

[Bla52] J. Blatt and V. Weisskopf, *Theoretical nuclear physics*, Wiley, New York, 2$^{\text{nd}}$ edition, 1952.

[Boh36] N. Bohr, "Neutron capture and nuclear constitution", Nature **137**, 344 (1936).

[Cas00] R. Casten, *Nuclear structure from a simple perspective*, Oxford Science Publications, New York, 2$^{\text{nd}}$ edition, 2000.

[Cor00] L. Corradi et al., "Multinucleon transfer reactions in the ^{40}Ca+^{124}Sn system studied via γ-particle coincidences", Physical Review C **61**, 24609 (2000).

[Cro01] B. Crowley, "Developement of a Compton-scattering-based beam-intensity monitor at the HIγS facility", Master's thesis, Duke University, 2001.

[Dat73] S. Datta and J. S. Allen, "Photon scattering cross sections of ^{88}Sr in the energy region 8.6 to 12 MeV", Physical Review C **8**, 1421 (1973).

[De 87] H. De Vries, C. de Jager, and C. de Vries, "Nuclear charge-density-distribution parameters from elastic electron scattering", Atomic and Nuclear Data Tables **36** (1987).

[Dir95] P. Dirac, *The collected works of PAM Dirac, 1924-1948*, Cambridge University Press, 1995.

[Dja82] C. Djalali et al., "Systematics of the excitation of M1 resonances in medium heavy nuclei by 200 MeV proton inelastic scattering", Nucear Physics A **388**, 1 (1982).

[Egi05] T. Egidy and D. Bucurescu, "Systematics of nuclear level density parameters", Physical Review C **72**, 44311 (2005).

[Fag59] L. W. Fagg and S. S. Hanna, "Polarization measurements on nuclear gamma rays", Review of Modern Physics **31**, 711 (1959).

[Fal48] D. L. Falkoff, "Polarization correlation of successive gamma-ray quanta", Physical Review **73**, 518 (1948).

[Fee48] E. Feenberg and H. Primakoff, "Interaction of cosmic-ray primaries with sunlight and starlight", Physical Review **73**, 449 (1948).

[Fer50] E. Fermi, "Nuclear physics", A course given by Enrico Fermi at the University of Chicago, 1949, Chicago: University of Chicago Press, 1950, Rev. ed. (1950), It is not clear the original paper where this rule was proposed. It was derived in the reference [Dir95]. Although this refence is where it was termed "The golden rule".

[Fes92] H. Feshbach, *Theoretical nuclear physics: nuclear reactions*, John Wiley & Sons, Inc, 1992.

[Fit00] A. Fitzler, *Tv user-manual*, Institute for Nuclear Physics, University of Cologne, 2000.

[Ful56] E. G. Fuller and E. Hayward, "Nuclear elastic scattering of photons", Physical Review **101**, 692 (1956).

[Ful69] S. C. Fultz, B. L. Berman, J. T. Caldwell, R. L. Bramblett, and M. A. Kelly, "Photoneutron cross sections for ^{116}Sn, ^{117}Sn, ^{118}Sn, ^{119}Sn, ^{120}Sn, ^{124}Sn, and Indium", Physical Review **186**, 1255 (1969).

[Gil65] A. Gilbert and A. Cameron, "A composite nuclear-level density formula with shell corrections", Canadian Journal of Physics **43**, 1446 (1965).

[gnt03] "Geant4 - a simulations toolkit", Nuclear Instruments and Methods in Physical Research A **506**, 250 (2003).

[Gor82] A. M. Goryachev and G. N. Zalesnyy, "The studing of the photoneutron reactions cross sections in the region of the giant dipole resonance in Zinc, Germanium, Selenium, and Strontium isotopes.", Voprosy Teoreticheskoy i Yadernoy Fiziki **8**, 121 (1982).

[Gor98] S. Goriely, "Radiative neutron captures by neutron-rich nuclei and the r-process nucleosynthesis", Physics Letters B **436**, 10 (1998).

[Gov98] K. Govaert, F. Bauwens, J. Bryssinck, D. De Frenne, E. Jacobs, W. Mondelaers, L. Govor, and V. Y. Ponomarev, "Dipole excitations to bound states in ^{116}Sn and ^{124}Sn", Physical Review C **57**, 2229 (1998).

[Har02] T. Hartmann, J. Enders, P. Mohr, K. Vogt, S. Volz, and A. Zilges, "Dipole and electric quadrupole excitations in ^{40,48}Ca", Physical Review C **65**, 034301 (2002).

[Hed82] S. Hedman, K. Helenelund, L. Asplund, U. Gelius, and K. Siegbahn, "Line sharpening effect due to PCI in Ar LMM Auger spectra: experimental and theoretical results", Journal of Physics B: Atomic, Molecular, and Optical Physics **15**, L799 (1982).

[Hei54] W. Heitler, *The quantum theory of radiation*, Oxford, London, 3rd edition, 1954.

[Her97] R.-D. Herzberg et al., "Fine structure of the E1 response in ^{140}Ce below the particle threshold", Physics Letters B **390**, 49 (1997).

[Ish00] B. Ishkhanov, N. Yudin, and R. A. Eramzhyan, "Giant resonances in atomic nuclei", Physics of Particles and Nuclei **31**, 149 (2000).

[Kad83] S. Kadmenskij, V. Markushev, and V. Furman, "Radiation widths of neutron resonances and giant dipole resonances", Yadernaya Fizika **37**, 277 (1983).

[Kop87] J. Kopecky and R. Chrien, "Observation of the M1 giant resonance by resonance averaging in ^{106}Pd", Nuclear Physics A **468**, 285 (1987).

[Kop90] J. Kopecky and M. Uhl, "Test of gamma-ray strength functions in nuclear reaction model calculations", Physical Review C **41**, 1941 (1990).

[Kra04] A. Krasznahorkay et al., "Neutron-skin thickness in neutron rick isotopes", Nuclear Physics A **731**, 224 (2004).

[Krt02] M. Krticka, *Photon strength functions in rare-earth nuclei: studied from slow neutron capture*, Ph.D. thesis, Charles University, Prague, 2002.

[Leo94] W. R. Leo, *Techniques for nuclear and particle physics experiments: A how-to approach*, Springer-Verlag, 2$^{\text{nd}}$ edition, 1994.

[Lep71] A. Lepretre, H. Beil, R. Bergere, P. Carlos, A. Veyssiere, and M. Sugawara, "The giant dipole states in the A= 90 mass region", Nuclear Physics A **175**, 609 (1971).

[Lit07] E. Litvinova, P. Ring, and D. Vretenar, "Relativistic RPA plus phonon-coupling analysis of pygmy dipole resonances", Physics Letters B **647**, 111 (2007).

[Mac70] J. R. MacDonald, "Doppler shift measurements of nuclear lifetimes", Science **167**, 1339 (1970).

[Mad71] J. M. J. Madey, "Stimulated emission of bremsstrahlung in a periodic magnetic field", Journal of Applied Physics **42**, 1906 (1971).

[Mar85] T. C. Marshall, *Free-electron lasers*, Macmillan Publishing Co., New York, 1985.

[Mat83] G. J. Mathews, A. Mengoni, F.-K. Thielemann, and W. A. Fowler, "Neutron capture rates in the r-process - the role of direct radiative capture", Astrophysical Journal **270**, 740 (1983).

[Mug00] S. Mughabghab and C. Dunford, "A dipole–quadrupole interaction term in E1 photon transitions", Physics Letters B **487**, 155 (2000).

[Mye38] R. D. Myers, "The angular distribution of resonance disintegration products", Physical Review **54**, 361 (1938).

[Oda87] T. Oda, M. Hino, and K. Muto, "The orbital current for the $0^+ \rightarrow 1^+$ M1 excitations in the even-even $f_{7/2}$ shell nuclei", Physics Letters B **190**, 14 (1987).

[Paa03] N. Paar, P. Ring, T. Niksic, and D. Vretenar, "Quasiparticle random phase approximation based on the relativistic Hartree-Bogoliubov model", Physical Review C **67**, 034312 (2003).

[Paa05] N. Paar, T. Niksic, D. Vretenar, and P. Ring, "Isotopic dependence of the pygmy dipole resonance", Physics Letters B **606**, 288 (2005).

[Paa07] N. Paar, D. Vretenar, E. Khan, and G. Colò, "Exotic modes of excitation in atomic nuclei far from stability", Reports on Progress in Physics **70**, 691 (2007).

[Pie06] J. Piekarewicz, "Pygmy dipole resonance as a constraint on the neutron skin of heavy nuclei", Physical Review C **73**, 044325 (2006).

[Ply00] V. Plyaskin and R. Kosilov, "Level-density parameters in the back-shifted Fermi gas model", Physics of Atomic Nuclei **63**, 752 (2000).

[Pov02] B. Povh, K. Rith, C. Scholz, and F. Zetsche, *Particles and nuclei: an introduction to the physical concepts*, Springer, New York, 3rd edition, 2002.

[Rei60] K. Reibel and A. K. Mann, "Energy level parameters from nuclear resonance fluorescence at 7 Mev", Physical Review **118**, 701 (1960).

[Rei97] J. Reif et al., "Resonant photon scattering on the semi-magic nucleus ^{89}Y up to 7 MeV", Nuclear Physics A **620**, 1 (1997).

[Ric91] A. Richter, "Electron scattering and elementary excitations", Nuclear Physics A **522**, 139 (1991).

[Saa95] P. Saarinen, J. Kauppinen, and J. Partanen, "New method for spectral line shape fitting and critique on the Voigt line shape model", Applied Spectroscopy **49**, 1438 (1995).

[Sar04] D. Sarchi, P. Bortignon, and G. Colò, "Dipole states in stable and unstable nuclei", Physics Letters B **601**, 27 (2004).

[Sav06] D. Savran, M. Babilon, A. M. van den Berg, M. N. Harakeh, J. Hasper, A. Matic, H. J. Wörtche, and A. Zilges, "Nature of the pygmy dipole resonance in ^{140}Ce studied in $(\alpha, \alpha'\gamma)$ experiments", Physical Review Letters **97**, 172502 (2006).

[Sch07] R. Schwengner, G. Rusev, N. Benouaret, R. Beyer, M. Erhard, E. Grosse, A. R. Junghans, J. Klug, K. Kosev, L. Kostov, C. Nair, N. Nankov, K. D. Schilling, and A. Wagner, "Dipole response of ^{88}Sr up to the neutron-separation energy", Physical Review C **76**, 034321 (2007).

[Sol92] V. Solov'ev, *Theory of atomic nuclei: quasi-particles and phonons*, CRC Press, 1992.

[Suz90] Y. Suzuki, K. Ikedo, and H. Sato, "New type of dipole vibration in nuclei", Progress in Theoretical Physics **83**, 180 (1990).

[Tay97] J. Taylor, *An introduction to error analysis*, University Science Books Mill Valley, Calif, 1997.

[Ter06] J. Terasaki and J. Engel, "Self-consistent description of multipole strength: Systematic calculations", Physical Review C **74**, 044301 (2006).

[Ter07a] J. Terasaki and J. Engel, "Excited-state density distributions in neutron-rich nuclei", Physical Review C **76**, 044320 (2007).

[Ter07b] J. Terasaki, 2007, Private communication with Jun Terasaki.

[Til93] D. Tilley, H. Weller, and C. Cheves, "Energy levels of light nuclei A= 16-17", Nuclear Physics A **564**, 1 (1993).

[Ton06] A. P. Tonchev, C. Angell, M. Boswell, C. R. Howell, H. J. Karwowski, J. H. Kelley, W. Tornow, and N. Tsoneva, "Low-energy dipole modes of excitation below the neutron separation energy", in *Capture Gamma-Ray Spectroscopy and Related Topics*, edited by A. Woehr and A. Aprahamian, volume 819 of *American Institute of Physics Conference Series*, pages 350–354, 2006.

[Tso04] N. Tsoneva, H. Lenske, and C. Stoyanov, "Pygmy dipole resonances as a manifestation of the structure of the neutron-rich nuclei", Nuclear Physics, Section A **731**, 273 (2004).

[Tso07] N. Tsoneva and H. Lenske, "Investigation of pygmy dipole resonances in the tin region", eprint arXiv: 0706.4204 (2007).

[Var03] V. Varlamov, N. Peskov, D. Rudenko, and M. Stepanov, "Photoneutron reaction cross sections in experiments with beams of quasi-monoenergetic annihilation photons", Preprint SINP MSU **2**, 715 (2003).

[Zar78] D. Zaretskii and V. Sirotkin, "Total radiative widths of neutron resonances", Soviet Journal of Nuclear Physics(Engl. Transl **27** (1978).